Immunity

Cell-autonomous regulation of complement C3 by factor H limits macrophage efferocytosis and exacerbates atherosclerosis

Graphical abstract

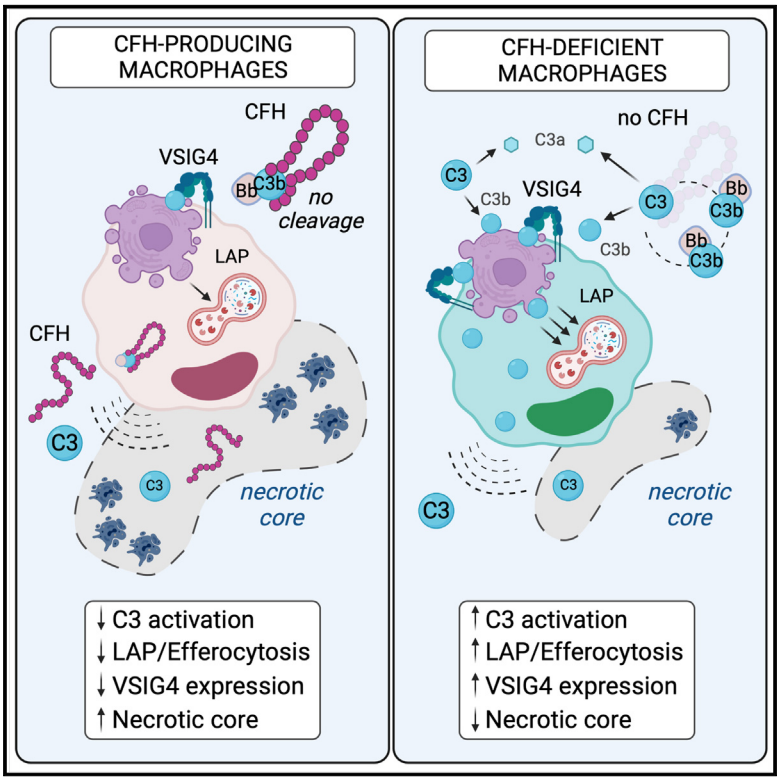

Highlights

- Expression of CFH and C3 is co-regulated in monocytes/macrophages upon inflammation
- C3- and CFH-producing macrophages populate murine and human atherosclerotic lesions
- CFH-deficient macrophages display enhanced cell-autonomous C3 consumption
- Loss of hematopoietic CFH heightens C3-mediated efferocytosis and limits plaque necrosis

Authors

Máté G. Kiss, Nikolina Papac-Miličević, Florentina Porsch, ..., Claudia Kemper, Ziad Mallat, Christoph J. Binder

Correspondence

christoph.binder@meduniwien.ac.at (C.J.B.), mate.kiss@mssm.edu (M.G.K.)

In brief

Misregulation of complement cascade is associated with chronic inflammatory disease. Kiss et al. report the impact of local complement regulation on atherosclerotic lesions, finding that monocyte-derived complement factor H limits cell-autonomous alternative complement activation. This regulation restricts monocyte-derived macrophages' pro-resolving functions and promotes plaque necrosis in a murine model of atherosclerosis.

Kiss et al., 2023, Immunity *56*, 1–16
August 8, 2023
https://doi.org/10.1016/j.immuni.2023.06.026

CellPress

Immunity

CellPress

Article

Cell-autonomous regulation of complement C3 by factor H limits macrophage efferocytosis and exacerbates atherosclerosis

Máté G. Kiss,[1,2,16,*] Nikolina Papac-Miličević,[1,16] Florentina Porsch,[1,2] Dimitrios Tsiantoulas,[1,3] Tim Hendrikx,[1] Minoru Takaoka,[3] Huy Q. Dinh,[4] Marie-Sophie Narzt,[5] Laura Göderle,[1] Mária Ozsvár-Kozma,[1] Michael Schuster,[2] Nikolaus Fortelny,[2,6] Anastasiya Hladik,[7] Sylvia Knapp,[7] Florian Gruber,[5] Matthew C. Pickering,[8] Christoph Bock,[2,9] Filip K. Swirski,[10] Klaus Ley,[11] Alma Zernecke,[12] Clément Cochain,[12,13] Claudia Kemper,[14] Ziad Mallat,[3,15] and Christoph J. Binder[1,2,17,*]

[1]Department of Laboratory Medicine, Medical University of Vienna, Vienna, Austria
[2]CeMM Research Center for Molecular Medicine of the Austrian Academy of Sciences, Vienna, Austria
[3]Division of Cardiovascular Medicine, Department of Medicine, University of Cambridge, Cambridge, UK
[4]McArdle Laboratory for Cancer Research, University of Wisconsin-Madison School of Medicine and Public Health, Madison, WI, USA
[5]Department of Dermatology, Medical University of Vienna, Vienna, Austria
[6]Department of Biosciences and Medical Biology, University of Salzburg, Salzburg, Austria
[7]Department of Medicine I, Laboratory of Infection Biology, Medical University of Vienna, Vienna, Austria
[8]Centre for Inflammatory Disease, Imperial College, London, UK
[9]Medical University of Vienna, Institute of Artificial Intelligence, Center for Medical Data Science, Vienna, Austria
[10]Cardiovascular Research Institute, Icahn School of Medicine at Mount Sinai, New York, NY, USA
[11]Immunology Center of Georgia, Augusta University, Augusta, GA, USA
[12]Institute of Experimental Biomedicine, University Hospital Würzburg, Würzburg, Germany
[13]Comprehensive Heart Failure Center Würzburg, University Hospital Würzburg, Würzburg, Germany
[14]Inflammation Research Section, National Heart, Lung and Blood Institute, Bethesda, MD 20892, USA
[15]Institut National de la Santé et de la Recherche Médicale, Paris Cardiovascular Research Center, Paris, France
[16]These authors contributed equally
[17]Lead contact
*Correspondence: christoph.binder@meduniwien.ac.at (C.J.B.), mate.kiss@mssm.edu (M.G.K.)
https://doi.org/10.1016/j.immuni.2023.06.026

SUMMARY

Complement factor H (CFH) negatively regulates consumption of complement component 3 (C3), thereby restricting complement activation. Genetic variants in *CFH* predispose to chronic inflammatory disease. Here, we examined the impact of CFH on atherosclerosis development. In a mouse model of atherosclerosis, CFH deficiency limited plaque necrosis in a C3-dependent manner. Deletion of CFH in monocyte-derived inflammatory macrophages propagated uncontrolled cell-autonomous C3 consumption without downstream C5 activation and heightened efferocytotic capacity. Among leukocytes, *Cfh* expression was restricted to monocytes and macrophages, increased during inflammation, and coincided with the accumulation of intracellular C3. Macrophage-derived CFH was sufficient to dampen resolution of inflammation, and hematopoietic deletion of CFH in atherosclerosis-prone mice promoted lesional efferocytosis and reduced plaque size. Furthermore, we identified monocyte-derived inflammatory macrophages expressing C3 and CFH in human atherosclerotic plaques. Our findings reveal a regulatory axis wherein CFH controls intracellular C3 levels of macrophages in a cell-autonomous manner, evidencing the importance of on-site complement regulation in the pathogenesis of inflammatory diseases.

INTRODUCTION

Complement represents the serum-effective protease cascade of innate immunity with a critical role in detecting and clearing invading microorganisms and dying cells.[1,2] The proteolytic cleavage of the central complement component 3 (C3) is the convergence point in the activation of three separate complement pathways.[3] Although the classical and lectin pathways are triggered by antibody-mediated antigen binding or carbohydrate recognition on microbial surfaces, respectively, the alternative complement pathway is continuously triggered by a tick-over mechanism acting as its own catalyst.[4] The delicate balance in complement activation is tightly coordinated by a wide array of regulators that prevent unwanted host tissue damage.[5]

Please cite this article in press as: Kiss et al., Cell-autonomous regulation of complement C3 by factor H limits macrophage efferocytosis and exacerbates atherosclerosis, Immunity (2023), https://doi.org/10.1016/j.immuni.2023.06.026

While most of the complement components are primarily produced in the liver, extrahepatic sources of complement exist, including immune cells.[6] In humans, hematopoietic C3 can contribute up to 5% of the circulating C3 pool after bone marrow transplantation.[7] Complement activation fragments of immune cell origin can engage complement receptors independent of their serum-derived counterparts and act in a paracrine or an autocrine manner[8–10] to orchestrate cellular immunity, including lymphocyte function[11–13] and opsonization of cyto-invasive bacteria,[14] viruses,[15] and apoptotic cells.[16] Furthermore, tonic generation of bioactive C3 and C5 cleavage products occurs in an intracellular fashion,[17] mediating basic cellular processes.[18,19] Based on these observations, on-site complement production by hematopoietic cells may have a fundamental physiological relevance in age-related chronic inflammatory disorders that are characterized by persistent leukocyte infiltration.

Atherosclerosis is a lipid-driven chronic inflammatory disease and the pathology underlying coronary artery disease (CAD) and stroke, leading causes of death worldwide.[20] Monocyte-derived macrophages are central to the maladaptive, non-resolving inflammatory response during atherosclerotic lesion progression.[21] In contrast to the common notion that the role of complement in atherosclerosis is primarily driven by serum-derived complement, there is increasing evidence that complement factors are actively expressed in atherosclerotic plaques[22] with recent single-cell sequencing data suggesting distinct lesional macrophage subsets as potential sources of local complement production.[23–25] Although complement proteins have been long known to be present in human atherosclerotic plaques,[26] exhibiting both protective and detrimental properties,[27,28] the pathologic importance of local vis-à-vis systemic complement in atherosclerotic lesion formation, including the regulation of cell-autonomous responses, is not well understood.

Complement factor H (CFH) is a key regulator of alternative complement activation and the most abundant complement repressor in plasma of mainly hepatic origin.[29] By accelerating the decay of the alternative C3 convertase, CFH inhibits C3 cleavage in the fluid phase[30] and on cellular surfaces via binding to glycosaminoglycans[31] and malondialdehyde epitopes.[32] Consequently, global loss of CFH in mice results in uncontrolled systemic complement activation due to the continuous consumption of circulating C3.[33] In humans, genetic variants in the CFH gene, including the common CFH polymorphism *rs1061170*, which results in a histidine 402 to tyrosine exchange (Y402H) and impairs the binding to malondialdehyde epitopes,[32] strongly predisposes to chronic inflammatory diseases, such as membranoproliferative glomerulonephritis and age-related macular degeneration (AMD).[34]

Here, we examined the impact of CFH on atherosclerosis development. There are conflicting results on the association of the Y402H variant with cardiovascular disease risk,[22] and although CFH was found to be deposited in atherosclerotic lesions,[35] its role in atherosclerosis remains elusive. We found that CFH dampens the efferocytotic capacity of macrophages by controlling their C3 consumption. We could further demonstrate that CFH derived from inflammatory monocytes and macrophages is a key contributor to the progression of atherosclerosis by limiting lesional apoptotic cell clearance. Our findings propose a key role for on-site vis-à-vis systemic complement regulation in the pathogenesis of inflammatory diseases.

RESULTS

CFH deficiency protects from plaque necrosis in a C3-dependent fashion

First, to evaluate whether CFH deficiency affects atherosclerosis and is dependent on its complement-regulatory functions, we bred $C3^{+/+}Cfh^{+/+}Ldlr^{-/-}$, $C3^{+/+}Cfh^{-/-}Ldlr^{-/-}$, $C3^{-/-}Cfh^{+/+}Ldlr^{-/-}$, and $C3^{-/-}Cfh^{-/-}Ldlr^{-/-}$ mice and fed them a western-type diet (WTD) for 10 weeks. Plasma cholesterol and triglyceride levels were comparable between the groups (Figure 1A), suggesting no significant impact of either CFH or C3 deficiency on lipid metabolism. As expected, the absence of CFH led to diminished circulating C3 levels, while we confirmed that C3 was undetectable in the plasma of C3-deficient mice (Figure 1B). Consistent with previous findings,[27] C3 deficiency led to heightened aortic lipid content, while loss of CFH showed no effect (Figure 1C). Furthermore, in agreement with our recent report,[36] CFH-deficient mice displayed an increase in circulating anti-dsDNA (double-stranded DNA) autoantibodies compared with $Cfh^{+/+}Ldlr^{-/-}$ controls (Figure S1A). Although both excessive complement activation[37] and systemic autoimmunity[38] accelerate atherosclerosis, we found no difference in atherosclerotic lesion size between the groups (Figure 1D). Instead, global loss of CFH resulted in reduced necrotic core formation and this effect was reverted in $C3^{-/-}Cfh^{-/-}Ldlr^{-/-}$ mice (Figure 1E), while independent from bone marrow hematopoiesis, circulating monocyte levels, and lesional macrophage or collagen content (Figures S1B–S1E). Thus, CFH promotes necrotic core formation in a C3-dependent manner.

CFH controls intracellular C3 levels in monocyte-derived macrophages

Necrotic core formation is typically a consequence of defective efferocytosis by macrophages during atherosclerosis progression.[39] CFH promotes inflammation in AMD.[40] The proposed mechanism involves subretinal accumulation of mononuclear phagocytes due to the blockade of TSP1-dependent CD47 activation. However, CD47 activation seemed unlikely to mediate the protective effect of CFH deficiency in atherosclerosis, as pharmacological inhibition of CD47 prevents lesion formation by restoring efferocytosis[41] and our results indicate a C3-dependent role for CFH in necrotic core formation. Therefore, we wondered whether CFH modulates inflammation by mediating C3 activation on a cellular level.

To test this, we first treated bone-marrow-derived macrophages (BMDMs) from wild-type (WT) mice with inflammatory stimuli and measured C3 production. Both interferon-gamma (IFNγ) and lipopolysaccharide (LPS) treatment led to increased *C3* expression and intracellular C3 accumulation (Figure S2A). Next, we isolated monocyte-derived macrophages (Mo-Macs) or resident macrophages (Res-Macs) from the peritoneal cavity of mice injected with or without the sterile inflammatory trigger thioglycolate, respectively. Mo-Macs had higher C3 production relative to Res-Macs (Figure S2B). Notably, surface-bound levels of C3 were minute (Figure S2C) and comparable between Mo-Macs and Res-Macs (Figure S2D). As C3 activation is tightly

Please cite this article in press as: Kiss et al., Cell-autonomous regulation of complement C3 by factor H limits macrophage efferocytosis and exacerbates atherosclerosis, Immunity (2023), https://doi.org/10.1016/j.immuni.2023.06.026

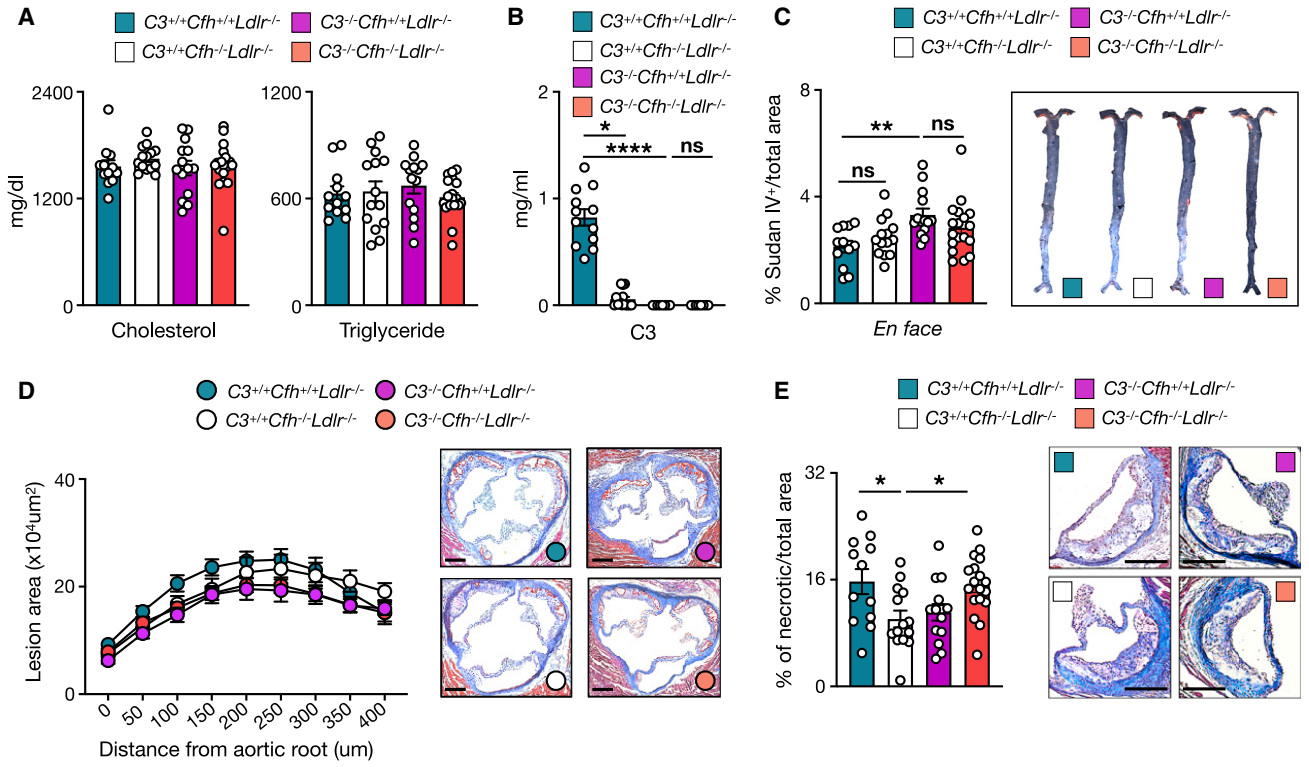

Figure 1. Global complement factor H deficiency protects from necrotic core formation in a C3-dependent manner

C3$^{+/+}$*Cfh*$^{+/+}$*Ldlr*$^{-/-}$, *C3*$^{+/+}$*Cfh*$^{-/-}$*Ldlr*$^{-/-}$, *C3*$^{-/-}$*Cfh*$^{+/+}$*Ldlr*$^{-/-}$, and *C3*$^{-/-}$*Cfh*$^{-/-}$*Ldlr*$^{-/-}$ mice were fed an atherogenic diet for 10 weeks (n = 12, 14, 14, and 18, respectively; pooled from two independent experiments).

(A) Plasma cholesterol and triglyceride levels measured by an automated enzymatic method.

(B) Total plasma C3 levels quantified by ELISA.

(C) Quantitative analysis of atherosclerosis of the whole aorta. Data are expressed as percentage of Sudan IV-stained area of the entire aorta. Representative images are shown.

(D) Quantification of aortic root plaque size. Values represent the average μm^2 of nine sections throughout the entire aortic origin. Representative images of Masson's trichrome-stained sections are shown. Original magnification, 50×; scale bars, 200 μm.

(E) Assessment of necrotic core formation in cross sections at the aortic origin. Bars indicate the percentage of necrotic area per total lesion area throughout the entire aortic origin. Representative images are shown. Original magnification, 50×; scale bars, 200 μm. Each symbol represents individual mice. Mean ± SEM, statistical significance was evaluated by one-way ANOVA followed by Tukey's multiple comparison test (*p < 0.05, **p < 0.01, ****p < 0.0001).

coupled to subsequent C5 consumption, we compared C3 and C5 production by Mo-Macs. Remarkably, while Mo-Macs expressed and secreted substantial amount of C3, we did not observe detectable C5 either on the mRNA or on the protein level (Figure 2A).

Mo-Macs are derived from circulating Ly6C^{hi} monocytes that infiltrate the peritoneum upon challenge.[42] Intracellular flow cytometry staining revealed that >80% of infiltrating peritoneal Ly6C^{hi} monocytes contained C3 (Figure S2E), whereas patrolling Ly6C^{lo} monocytes had minimal C3 content (Figure 2B). Moreover, peritoneal C3^{+}Ly6C^{hi} monocytes displayed elevated surface levels of the macrophage markers F4/80 and C5aR1, indicating that C3 accumulation is associated with macrophage differentiation (Figure S2E). Finally, we quantified total cell-associated C3 levels and found that peritoneal Mo-Macs and inflammatory Ly6C^{hi} monocytes contained >10× more intracellular C3 compared to Res-Macs or unchallenged circulating Ly6C^{hi} monocytes (Figure 2C).

Having identified a robust potential for Ly6C^{hi} Mo-Macs to produce C3, we aimed to determine whether loss of CFH influences intracellular C3 levels. We sorted Ly6C^{hi} monocytes from the peritoneum of thioglycolate-injected *Cfh*$^{+/+}$ and *Cfh*$^{-/-}$ mice, and, intriguingly, monocytes from *Cfh*$^{-/-}$ mice contained less intact C3 compared with controls (Figure 2D). Consistent with this, CFH-deficient Mo-Macs had dramatically reduced cell-associated C3 levels (Figure 2E), which was due to a decrease in the intracellular C3 pool (Figure 2F). This appeared to be a consequence of enhanced C3 consumption, as judged by a concomitant increase in intracellular C3a levels (Figure S2F) and a higher C3a/C3 ratio (Figure 2G). Intracellular complement activation drives C5aR1-dependent NLRP3 inflammasome activity in human T cells.[19] In line with the lack of *C5* expression in Mo-Macs, CFH deficiency did not induce the proinflammatory C5a-inflammasome axis, as macrophages from *Cfh*$^{+/+}$ and *Cfh*$^{-/-}$ mice displayed comparable interleukin1-beta (IL-1β) secretion (Figure S2G). These data demonstrate that uncontrolled cell-autonomous C3 consumption as a result of CFH deficiency does not trigger downstream C5 activation in macrophages, including the proinflammatory sequelae.

Please cite this article in press as: Kiss et al., Cell-autonomous regulation of complement C3 by factor H limits macrophage efferocytosis and exacerbates atherosclerosis, Immunity (2023), https://doi.org/10.1016/j.immuni.2023.06.026

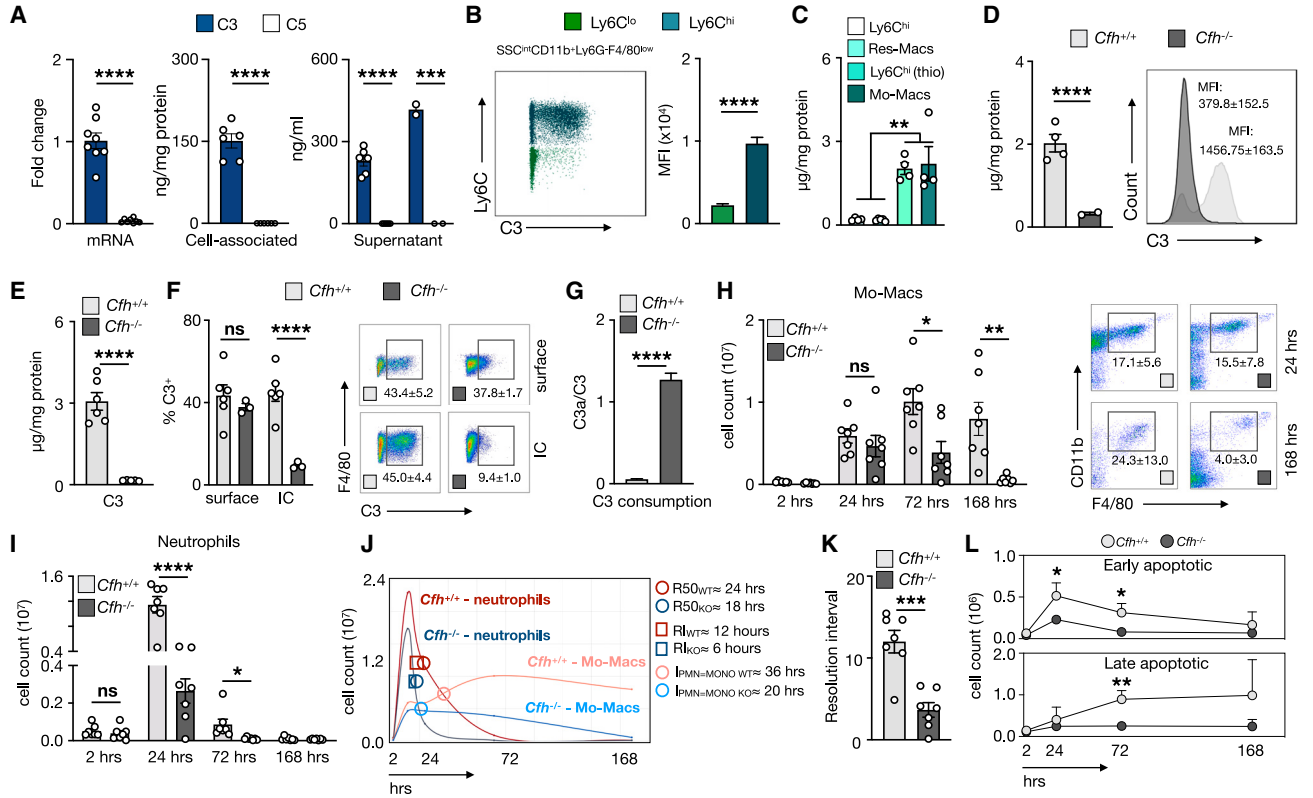

Figure 2. Complement factor H controls cell-autonomous C3 activation in monocyte-derived macrophages and delays the resolution of inflammation

(A) C3 and C5 mRNA and protein levels of monocyte-derived macrophages (Mo-Macs) from thioglycolate-injected mice measured by real-time qRT-PCR and ELISA.

(B) C3 mean fluorescence unit (MFI) of peritoneal Ly6C^{hi} and Ly6C^{lo} monocytes of thioglycolate-injected mice, determined by intracellular flow cytometry.

(C) Intracellular C3 levels normalized to cellular protein content in cell lysates of sorted circulating Ly6C^{hi} monocytes and resident peritoneal macrophages (Res-Macs) from unchallenged mice as well as Ly6C^{hi} monocytes, and Mo-Macs from thioglycolate-injected mice, quantified by ELISA.

(D) Intracellular C3 levels of peritoneal Ly6C^{hi} monocytes of thioglycolate-injected *Cfh*$^{+/+}$ and *Cfh*$^{-/-}$ mice quantified by ELISA. Representative histograms show C3 levels within peritoneal Ly6C^{hi} monocytes assessed by intracellular flow cytometry.

(E–G) Characterization of Mo-Macs in the peritoneal lavage fluid of thioglycolate-injected *Cfh*$^{+/+}$ vs. *Cfh*$^{-/-}$ mice.

(E) Intracellular C3 levels of adherent Mo-Macs by ELISA.

(F) Bar graphs and representative cytometry plots show surface and intracellular C3 staining of Mo-Macs measured by flow cytometry.

(G) C3a/C3 ratio, a measure of complement activation, as judged by total intracellular C3a and C3 levels in lysates of adherent Mo-Macs quantified by ELISA.

(H–L) Characterization of the resolution of inflammation in the peritoneal lavage fluid of *Cfh*$^{+/+}$ vs. *Cfh*$^{-/-}$ mice 2, 24, 72, and 168 h after thioglycolate injection. Absolute numbers of (H) Mo-Macs and (I) neutrophils, quantified by flow cytometry.

(J) Resolution curves and (K) the corresponding resolution interval, calculated by the resolution indices extrapolated from the curves, are shown. PMN, polymorphonuclear neutrophils; MONOs, monocytes.

(L) Absolute numbers of early (AnnV$^+$7-AAD$^-$) and late (AnnV$^+$7-AAD$^+$) apoptotic cells, assessed by flow cytometry. AnnV, Annexin V; 7-AAD, 7-aminoactinomycin D. Each symbol represents individual mice. Data are representative of at least three independent experiments. Mean ± SEM, two-tailed Student's t tests (*p < 0.05, **p < 0.01, ***p < 0.001, ****p < 0.0001).

To explore the relevance of altered intracellular C3 levels in the kinetics of sterile inflammation, we subjected *Cfh*$^{+/+}$ and *Cfh*$^{-/-}$ mice to thioglycolate-induced sterile peritonitis over multiple time points. Despite no effect of CFH on steady-state peritoneal macrophage numbers (Figure S2H) or on the initiation of inflammation, *Cfh*$^{-/-}$ mice displayed accelerated resolution of sterile peritonitis, as indicated by a robust reduction in peritoneal Mo-Macs compared with controls (Figure 2H). Because efferocytosis is key for the resolution of sterile peritonitis,[42] we next monitored *in vivo* neutrophil efferocytosis and calculated resolution indices and interval according to Bannenberg et al.[43] Although early neutrophil infiltration (Figure 2I) and CXCL1 levels (Figure S2I) were comparable in the peritoneal lavage fluid of *Cfh*$^{+/+}$ and *Cfh*$^{-/-}$ mice, loss of CFH led to a sharp decrease in neutrophil numbers 24 h post injection (Figure 2I), indicative of accelerated efferocytosis of dying neutrophils. Consequently, we predicted the respective Ψ_{max} (maximum neutrophil numbers) values and projected our dataset on resolution curves (Figure 2J). We extrapolated an R_{50} (time point at which neutrophils decrease by 50%) of 24 h for the control group, while R_{50} was 18 h in CFH-deficient mice. These led us to estimate that the resolution interval (RI) of *Cfh*$^{+/+}$ mice is approximately 12 h, while

Please cite this article in press as: Kiss et al., Cell-autonomous regulation of complement C3 by factor H limits macrophage efferocytosis and exacerbates atherosclerosis, Immunity (2023), https://doi.org/10.1016/j.immuni.2023.06.026

Cfh$^{-/-}$ mice displayed a considerably faster RI, ca. 6 h, which led to a 3.3-fold increase in neutrophil clearance over 24 h (Figure 2K). Similar findings were made using zymosan-induced sterile peritonitis (Figure S2J). Furthermore, we calculated the point of intersection ($I_{PMN = MONO}$; the time point when the increase in Mo-Macs intersects the decrease of neutrophils). Although this index was approximately 36 h in the control group, we calculated an $I_{PMN = MONO}$ of 20 h in CFH-deficient mice, further supporting accelerated resolution upon CFH deficiency (Figure 2J). Accordingly, *Cfh*$^{-/-}$ mice had fewer early (AnnV$^+$7-AAD$^-$) and late (AnnV$^+$7-AAD$^+$) apoptotic cells in the peritoneal cavity throughout the course of peritonitis (Figure 2L). Taken together, these indices led us to conclude that loss of CFH harbors a 1.8–2.0× faster pro-resolving capacity following an acute inflammatory challenge.

CFH-deficient macrophages display heightened efferocytotic capacity

To perform functional validation of the pro-resolving capacity of CFH-deficient macrophages, we carried out *ex vivo* efferocytosis assays in which equivalent numbers of isolated peritoneal Mo-Macs from *Cfh*$^{+/+}$ and *Cfh*$^{-/-}$ mice were incubated with chloromethylfluorescein diacetate (CMFDA)-labeled apoptotic macrophages for 1.5 h. Subsequent quantification of CMFDA$^+$ Mo-Macs by flow cytometry revealed that CFH-deficient macrophages indeed display heightened efferocytotic capacity compared with WT macrophages (Figure 3A). Cleavage products of C3 are potent opsonins and are required for efficient phagocytosis by macrophages.[44] Therefore, we enumerated the presence of C3 on apoptotic Mo-Macs and found that *Cfh*$^{-/-}$ mice display a slight increase in the frequency of C3-coated 7-aminoactinomycin D$^+$ (7-AAD$^+$) apoptotic cells in the peritoneal cavity (Figure 3B), suggesting enhanced opsonization. To test whether opsonization alone is responsible for the heightened efferocytotic capacity of CFH-deficient Mo-Macs, we repeated our assay in the presence of WT or CFH-deficient sera. Exposure to *Cfh*$^{-/-}$ serum did not influence the uptake of CMFDA-labeled apoptotic cells of *Cfh*$^{+/+}$ Mo-Macs, and efferocytosis by *Cfh*$^{-/-}$ Mo-Macs was also unaffected by CFH-competent serum (Figure 3C). These observations suggest that independent of increased opsonization, cell-intrinsic mechanisms may shape the potent efferocytotic signature of CFH-deficient macrophages.

To decipher how loss of CFH licenses C3-dependent pro-efferocytotic functions, we performed RNA sequencing (RNA-seq) of Mo-Macs from *Cfh*$^{+/+}$ and *Cfh*$^{-/-}$ mice. Expression of over 1,000 genes was significantly altered ($q < 0.1$; Figures 3D, S3A, and S3B) and Enrichr-based pathway analysis[45,46] revealed that genes associated with the complement cascade were primarily upregulated in CFH-deficient Mo-Macs, again underlining the relevance of cell-autonomous complement in macrophages (Figure 3E). Other differentially regulated pathways included focal adhesion, inflammatory responses, and eicosanoid synthesis (Figure 3E). Confirming our previous observations, the regulation of apoptotic cell clearance, i.e., efferocytosis, was identified as the top biological process affected by CFH deficiency (Figure 3F). We next aimed to identify the molecular mechanisms that are accountable for heightened efferocytosis upon loss of CFH. In general, many hallmark genes of a disease-relevant macrophage subset[23,47–50] defined by high *Trem2* and *Spp1* expression were downregulated in Mo-Macs of *Cfh*$^{-/-}$ mice (Figure S3C), and we confirmed diminished *Spp1* transcript levels upon CFH deficiency in sorted Mo-Macs (Figure S3D). In parallel, CFH deficiency was associated with a marked upregulation of genes that are reminiscent of a resident-like macrophage phenotype (Figure S3C). Among these—in particular—we identified a high abundance of cell-surface receptors, including *Marco, Fcgr2b*, and *Timd4*, as well as the complement receptors *Itgam* and *Vsig4* (Figure 3G) that trigger an autophagy-related process involved in efficient efferocytosis, called LC3-associated phagocytosis (LAP).[51,52] LAP promotes rapid phagolysosomal fusion and the hydrolytic degradation of apoptotic material by conjugating lipids to LC3-bound phagosomal membranes,[39,53] and, notably, intracellular C3 promotes LC3-driven autophagic flux in an ATG16L1-dependent manner.[14,54] Therefore, we first validated the heightened surface expression of the respective LAP-associated receptors on *Cfh*$^{-/-}$ Mo-Macs (Figure 3H) and evaluated the conversion of cellular LC3-I to the lipidated LC3-II form by western blotting. Importantly, lysates of *Cfh*$^{-/-}$ Mo-Macs displayed an elevated LC3-II/LC3-I ratio compared with WT controls (Figure 3I), consistent with heightened LAP. Next, to verify that CFH deficiency promotes LAP via increased cell-associated C3 consumption, we supplemented Mo-Macs with increasing concentrations of purified C3 and confirmed C3 consumption by detecting elevated cell-associated C3a levels (Figure S3E). C3 supplementation increased the expression of *Timd4*—and especially *Vsig4*—by Mo-Macs in a dose-dependent manner (Figure 3J) and led to elevated LC3 conversion (Figure 3K). These data indicate that increased activation of cellular C3 promotes the emergence of phenotypically resident-like macrophages with high efferocytotic capacity.

We then sought to determine whether LAP blockage could delay the resolution of peritonitis in CFH-deficient mice. First, we treated CFH-deficient Mo-Macs with bafilomycin A1 (BafA1) prior to feeding them with pHrodo-labeled apoptotic macrophages. BafA1 is a specific vacuolar H + ATPase (V-ATPase) inhibitor that does not impact the lipidation of LC3 during autophagosome formation in canonical autophagy but specifically inhibits LC3 lipidation during LAP.[55] Accordingly, BafA1 exposure dampened the efferocytotic capacity of CFH-deficient Mo-Macs (Figure 3L). Next, we injected WT and CFH-deficient mice with BafA1 or PBS, 6 and 30 h post thioglycolate injection (Figure 3M), in a dose equivalent to previous reports.[56,57] BafA1 treatment dampened the resolution of sterile peritonitis, as judged by increased numbers of inflammatory Mo-Macs in the peritoneum of BAfA1-treated mice relative to their respective PBS-injected controls (Figures 3N, S3F, and S3G), and led to a more robust, over 2-fold delay in resolution, specifically in the CFH-deficient group, suggesting a blunted clearance of dying macrophages (Figures 3O and S3G). Together, our findings demonstrate that CFH inhibits efficient efferocytosis by controlling C3-mediated LAP.

Local CFH production by inflammatory monocytes/macrophages perpetuates inflammation

Having established a prominent role for CFH in C3-mediated efferocytosis, we next wondered whether CFH production by

Please cite this article in press as: Kiss et al., Cell-autonomous regulation of complement C3 by factor H limits macrophage efferocytosis and exacerbates atherosclerosis, Immunity (2023), https://doi.org/10.1016/j.immuni.2023.06.026

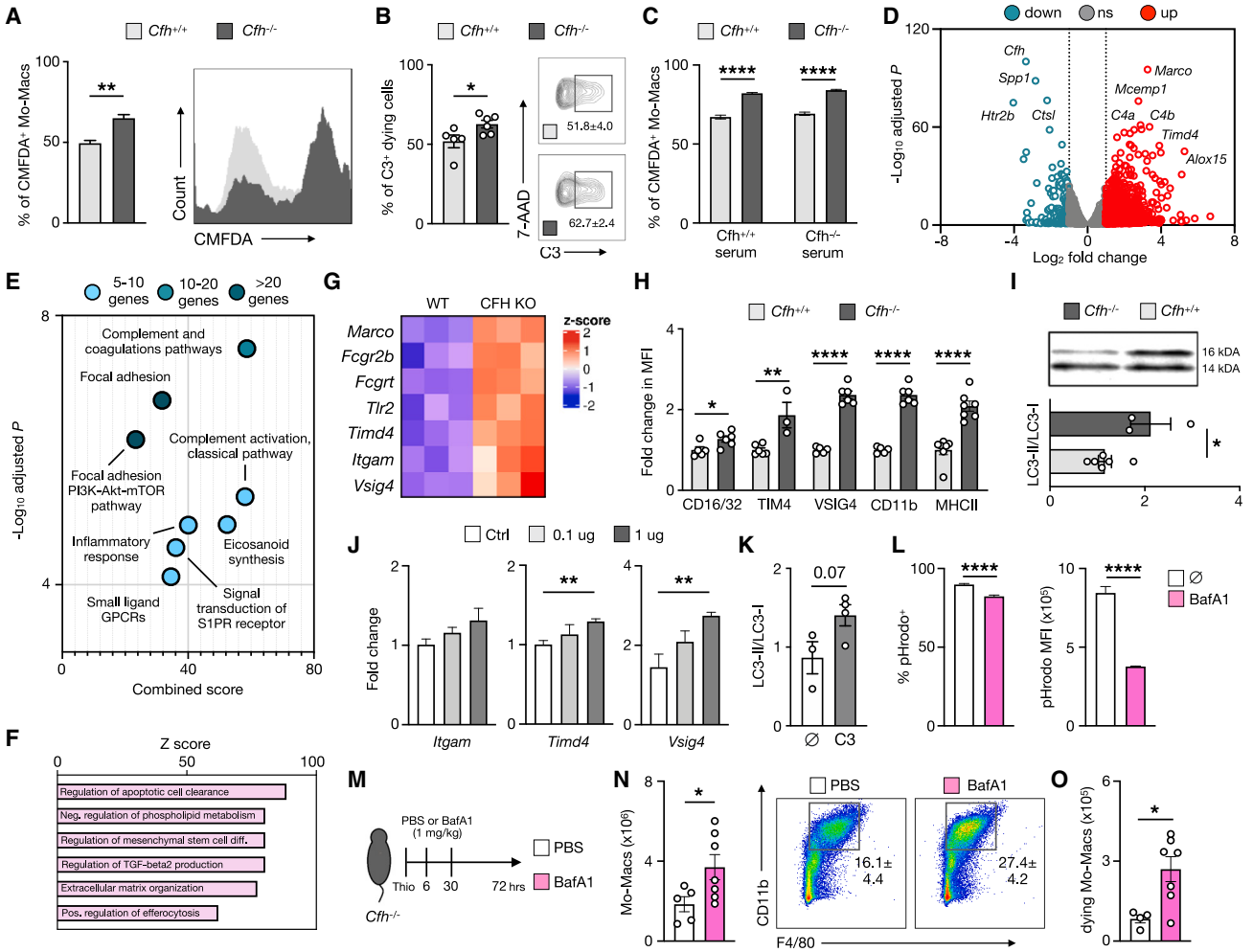

Figure 3. Complement-factor-H-deficient macrophages display heightened efferocytotic capacity

(A) *Ex vivo* efferocytosis assay using adherent Mo-Macs isolated from the peritoneal cavity of thioglycolate-injected *Cfh*$^{+/+}$ vs. *Cfh*$^{-/-}$ mice. Percentages of CMFDA^{+} efferocytotic Mo-Macs were quantified by flow cytometry. Representative histograms are shown.

(B) Assessment of opsonization, as judged by the percentage of C3^{+} and 7-aminoactinomycin D^{+} (7-AAD) double-positive Mo-Macs in the peritoneal cavity of *Cfh*$^{+/+}$ and *Cfh*$^{-/-}$ mice, determined by flow cytometry.

(C) *Ex vivo* efferocytosis assay showing percentages of CMFDA^{+} efferocytotic Mo-Macs, quantified by flow cytometry.

(D–I) Characterization of Mo-Macs in the peritoneal lavage fluid of thioglycolate-injected *Cfh*$^{+/+}$ vs. *Cfh*$^{-/-}$ mice. (D) Volcano plot of genes with expression change exceeding a factor of 1.5 ($q < 0.1$) from a genome-wide transcriptome profiling by RNA sequencing. (E and F) *Enrichr* analysis. The eight most overrepresented (E) biological pathways as well as (F) biological processes of all differentially expressed genes between wild-type and CFH-deficient Mo-Macs are shown. Color coding (E) represents the number of genes featured in each pathway. (G) Heatmap of LAP-associated genes upregulated in CFH-deficient macrophages. (H) Fold change in mean fluorescence intensity (MFI) of the surface levels of CD16/32, TIM4, VSIG4, CD11b, and MHCII on CFH-deficient Mo-Macs compared with controls, measured by flow cytometry. (I) Western blot analysis of intracellular LC3-I and LC3-II levels in lysates of Mo-Macs isolated from the peritoneal cavity of thioglycolate-injected *Cfh*$^{+/+}$ vs. *Cfh*$^{-/-}$ mice. A representative blot is shown.

(J) Real-time qRT-PCR analysis of *Itgam*, *Timd4*, and *Vsig4* transcript levels of *ex vivo* peritoneal Mo-Macs of thioglycolate-injected mice supplemented with increasing concentrations of purified mouse C3.

(K) Western blot analysis of intracellular LC3-I and LC3-II levels in lysates of Mo-Macs incubated with or without purified C3 (1 μg).

(L) pHrodo positivity and MFI of CFH-deficient Mo-Macs following bafilomycin A1 (BafA1; 200 nM) treatment and pHrodo+ apoptotic cell loading, measured by flow cytometry.

(M) Schematic representation of BafA1 treatment of *Cfh*$^{-/-}$ mice.

(N and O) Absolute numbers of Mo-Macs with corresponding flow cytometry plots (N) and (O) total counts of 7-AAD^{+} Mo-Macs in the peritoneal cavity of *Cfh*$^{-/-}$ mice, injected with or without BafA1 after thioglycolate injection, quantified by flow cytometry. Pool of two independent experiments. Each symbol represents individual mice. Mean ± SEM, two-tailed Student's t tests (*$p < 0.05$, **$p < 0.01$, ****$p < 0.0001$).

leukocytes affects the resolution of inflammation. We first investigated the expression profile of *Cfh*, along with other canonical complement repressors among various immune cell subsets of murine splenocytes. We found a unique expression pattern for *Cfh* with a restriction to monocytes, while other regulators were either undetectable (*C4bp, Cfhr1, Cfhr2, Clu, Vtn, Cpn1,*

Please cite this article in press as: Kiss et al., Cell-autonomous regulation of complement C3 by factor H limits macrophage efferocytosis and exacerbates atherosclerosis, Immunity (2023), https://doi.org/10.1016/j.immuni.2023.06.026

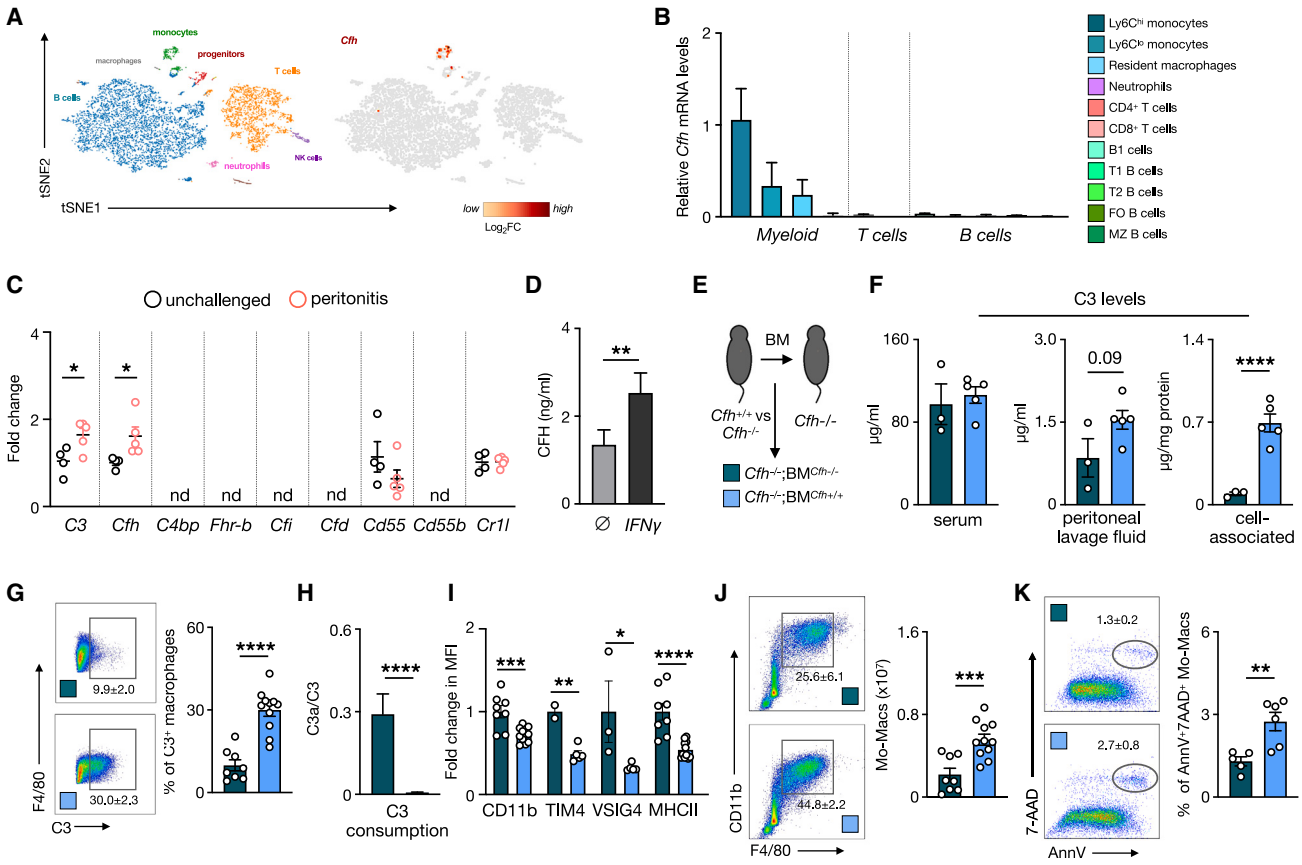

Figure 4. Monocyte/macrophage-derived complement factor H is sufficient to delay the resolution of inflammation

(A) Single-cell RNA-seq data from wild-type spleen, represented by t-distributed stochastic neighbor embedding (t-SNE). Left side demonstrates the clustering and annotation of splenic immune cell subsets. Gene expression profile of *Cfh* is shown.

(B) Relative gene expression of *Cfh* in fluorescence-activated cell sorting (FACS)-sorted splenic immune cell subsets of unchallenged mice measured by real-time qRT-PCR. Data are shown relative to *Cfh* expression in Ly6C^{hi} monocytes.

(C) Real-time qRT-PCR analysis of *C3* and multiple complement-regulatory proteins (*Cfh, C4bp, Fhr-b, Cfi, Cfd, CD55, CD55b, Cr1l*) in circulating Ly6C^{hi} monocytes sorted from the blood of thioglycolate-injected vs. control mice.

(D) Total secreted CFH levels in the supernatant of Mo-Macs treated with 100 ng/mL IFNγ.

(E–L) Lethally irradiated wild-type mice were reconstituted with bone marrow from *Cfh*$^{+/+}$ vs. *Cfh*$^{-/-}$ mice and were subjected to thioglycolate-induced sterile peritonitis 10 weeks after transplantation (n = 5 vs. n = 6, n = 3 vs. n = 6 of two independent experiments). (E) Schematic representation of chimeric models of CFH deficiency. (F) C3 concentration in the serum, peritoneal lavage fluid, as well as cell-associated C3 levels normalized to cellular protein content in lysates of adherent Mo-Macs of bone-marrow-chimeric mice measured by ELISA. (G) Bar graphs and representative flow cytometry plots show intracellular C3 levels of Mo-Macs measured by flow cytometry. (H) C3a/C3 ratio, a measure of complement activation, as judged by total intracellular C3a and C3 levels in lysates of adherent Mo-Macs quantified by ELISA. (I) Fold change in mean fluorescence intensity (MFI) of the surface levels of CD11b, TIM4, VSIG4, and MHCII on Mo-Macs of bone-marrow-chimeric mice, measured by flow cytometry. (J and K) Mo-Macs absolute numbers (J) and frequency (K) of late apoptotic (AnnV$^+$ 7-AAD$^+$) Mo-Macs in the peritoneal lavage fluid of bone-marrow-chimeric mice 72 h after thioglycolate injection, quantified by flow cytometry. Representative plots are shown. Each symbol represents individual mice. Mean ± SEM, two-tailed Student's t tests (*p < 0.05, **p < 0.01, ***p < 0.001, ****p < 0.0001).

Cd59, Cd55b) or ubiquitously expressed (*Cr1l*, *Cd55*) (Figures 4A and S4A). We confirmed our findings by real-time qRT-PCR analysis of sorted splenic leukocyte subsets, which further revealed that inflammatory Ly6C^{hi} monocytes predominantly account for *Cfh* expression (Figure 4B), suggesting an inflammatory regulation of CFH production by monocytes. Indeed, we could demonstrate that expression of *Cfh* is induced in circulating Ly6C^{hi} monocytes of thioglycolate-injected mice (Figure 4C), and isolated Mo-Macs were capable of secreting CFH in an IFNγ-inducible manner (Figure 4D).

Given the observation that CFH is the sole complement regulator with a compartmentalized expression pattern, we investigated the significance of monocyte-derived CFH during inflammation. We transplanted *Cfh*$^{-/-}$ mice with *Cfh*$^{-/-}$ or *Cfh*$^{+/+}$ bone marrow and subjected them to sterile peritonitis (Figure 4E). Although reconstitution of CFH production in the hematopoietic compartment of CFH-deficient mice did not affect C3 levels in the serum or in the peritoneal lavage fluid, it did normalize intracellular C3 levels in Mo-Macs (Figures 4F and 4G), which was accompanied by a robust decrease in cell-associated C3a/C3 ratio (Figure 4H). Furthermore, peritoneal Mo-Macs of CFH-competent bone-marrow-chimeric mice displayed reduced transcript levels (Figure S4B) and decreased surface expression (Figure 4I) of LAP receptors. Intriguingly, hematopoietic CFH was

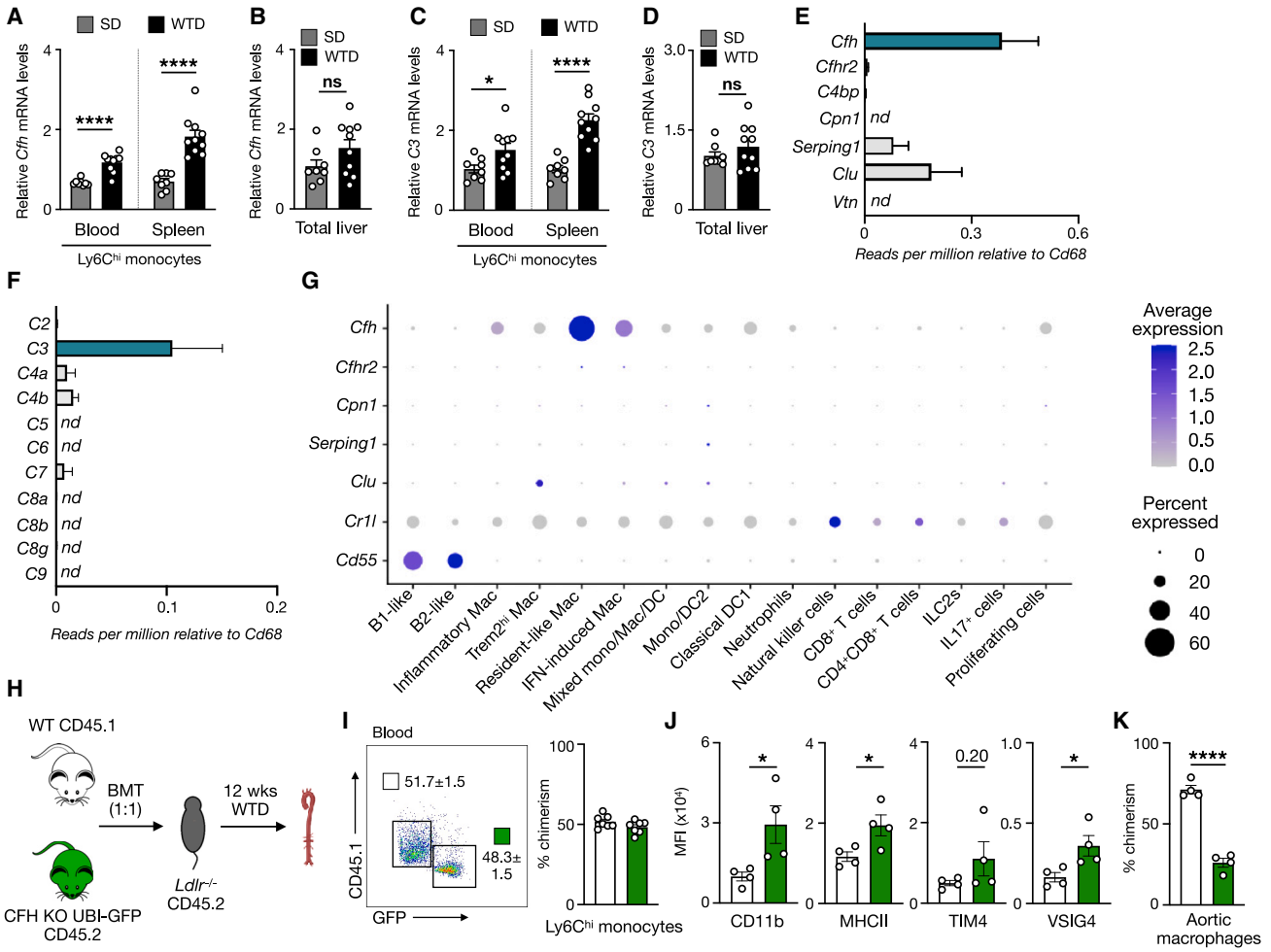

Figure 5. Complement factor H dominates local complement expression in aortic macrophages

(A–D) *Ldlr*$^{-/-}$ mice were fed a standard diet (SD) or western-type diet (WTD) for 12 weeks (n = 8 vs. n = 10). Real-time qRT-PCR analysis of *Cfh* and *C3* transcript levels in (A) and (C) circulating and splenic Ly6C^{hi} monocytes and in (B) and (D) total liver samples. Data are expressed relative to gene expression in SD-fed mice.

(E and F) Relative expression of (E) fluid-phase complement-regulatory proteins (*Cfh, Cfhr2, C4bp, Cpn1, Serping1, Clu*, and *Vtn*) as well as (F) complement cascade components in CD45^{+}CD11b^{+}CD64^{+} macrophages sorted from plaques of WTD-fed *Ldlr*$^{-/-}$ mice. Data are expressed as transcripts per million (TPM) relative to *Cd68* gene.

(G) Expression of complement repressors in aortic leukocyte subsets from a meta-analysis of nine single-cell RNA sequencing studies. Average expression level (log_2 scale) indicated by saturation of blue (dark blue is highest, with minimum scaling to 0). Dot size represents relative percentage of cells that expressed the corresponding genes within each cluster.

(H) Schematic representation of mixed 1:1 bone marrow transplantation experiment from control (WT, CD45.1) and CFH-deficient (CFH KO UBI-GFP, CD45.2) into Ldlr-deficient (*Ldlr*$^{-/-}$ CD45.2) mice, following a 12-week WTD feeding.

(I) Percent of chimerism among blood Ly6C^{hi} monocytes at harvest with a representative dot plot, quantified by flow cytometry.

(J and K) (J) Mean fluorescence intensity (MFI) of surface levels of CD11b, MHCII, TIM4, and VSIG4 and (K) percent of chimerism among aortic macrophages, measured by flow cytometry. Each symbol represents individual mice. Mean ± SEM, two-tailed Student's t tests (*p < 0.05, ****p < 0.0001).

sufficient to delay resolution, as judged by increased numbers of Mo-Macs (Figure 4J) as well as higher frequency of late apoptotic macrophages (Figure 4K) in the peritoneal lavage fluid of *Cfh*$^{+/+}$ bone-marrow-chimeric mice. Thus, our data demonstrate the significance of hematopoietic CFH production in regulating C3 consumption by macrophages and support a functional role for local complement regulation during inflammation.

Alternative pathway components dominate local complement production in atherosclerotic lesions

Ly6C^{hi} monocytes are hallmark cells of atherosclerosis being induced by hypercholesterolemia and accumulating in atherosclerotic lesions, where they differentiate to inflammatory macrophages.[58] Therefore, the negative effect of monocyte-derived CFH on efferocytosis could explain the observed protective role of CFH deficiency in atherosclerosis. Importantly, we could demonstrate increased *Cfh* expression in both blood as well as splenic Ly6C^{hi} monocytes of *Ldlr*$^{-/-}$ mice fed a WTD compared with standard-diet-fed (SD) mice (Figure 5A). Of note, *Cfh* expression in total liver tissue was not induced by WTD (Figure 5B) and directly correlated with the extent of myeloid cell infiltration indicated by *Itgam* expression (Figure S5A), suggesting that hypercholesterolemia triggers *Cfh* expression primarily in monocytes. We also found that *Cfh* is the most abundant

soluble complement regulator in CD45$^+$CD11b$^+$CD64$^+$ aortic macrophages isolated from atherosclerotic lesions of WTD-fed *Ldlr*$^{-/-}$ mice (Figure 5E). Concomitantly, transcript levels of *C3* were also upregulated in blood and splenic Ly6C^{hi} monocytes (Figure 5C), while unchanged in the liver of *Ldlr*$^{-/-}$ mice upon hypercholesterolemia (Figure 5D), and were also present in sorted lesional macrophages of WTD-fed *Ldlr*$^{-/-}$ mice (Figure 5F).

Next, we characterized the complement signature of plaque-infiltrating leukocytes from atherosclerotic mouse aortas in a comprehensive meta-analysis of single-cell RNA-seq (scRNA-seq) studies.[59] Again, we confirmed that among complement regulators, *Cfh* was expressed at the highest levels by aortic immune cells, exceeding the expression of membrane-bound complement regulators (*Cd55*, *Cr1l*), while other soluble repressors were barely detectable (*Clu*, *Serping1*, *Cpn*, *Cfhr2*) or not detectable at all (*C4bp*, *Vtn*) (Figure 5G). Furthermore, *Cfh* showed a unique expression pattern restricted to myeloid cells (predominantly monocytes and macrophages) and was particularly enriched in the subset of resident-like macrophages (Figure 5G). These cells potentially derive from infiltrating monocytes, which adapt a bona fide resident aortic macrophage phenotype of prominent phagocytotic signature.[23] Of note, expression of upstream alternative complement activators, such as properdin (*Cfp*) or factor B (*Cfb*), was also augmented by Ly6C^{hi} monocytes in response to a WTD (Figure S5B) and showed differential upregulation in resident-like aortic macrophages (Figure S5C), which suggests substantial on-site production of alternative pathway components in atherosclerotic lesions. In parallel, neither *C5* nor *C9* were expressed in sorted aortic macrophages (Figure 5F), and both *C5* and C9 mRNA were absent in all cell clusters of our meta-analysis (Figure S5D). These data suggest that plaque-infiltrating cells have the capacity to contribute to local complement activity, however, only at the level of C3. Thus, macrophage-derived CFH may promote disease progression by repressing C3 activation at the local milieu of atherosclerotic plaques.

To investigate whether CFH-deficient macrophages have an intrinsic advantage in clearing dead cells, we performed a mixed bone marrow transplantation study. We transplanted bone marrow at a 1:1 ratio from WT (CD45.1) and CFH-deficient ubiquitin (UBI)-GFP (CD45.2) mice into irradiated *Ldlr*$^{-/-}$ (CD45.2) mice (Figure 5H). 6 weeks after transplantation, we fed these mice a WTD for 12 weeks and measured the chimerism of Ly6C^{hi} monocytes deriving from WT (CD45.1$^+$) and CFH-deficient UBI-GFP (GFP$^+$CD45.2$^+$) animals. Despite observing balanced chimerism in peripheral blood (Figure 5I), aortic macrophages of *Cfh*$^{-/-}$ origin displayed heightened surface levels of LAP-associated receptors (Figure 5J). Similar results were obtained from infiltrating monocyte-derived macrophages of the spleen (Figure S5E). Intriguingly, chimerism of aortic macrophages showed a robust bias toward CD45.1$^+$ WT cells (Figure 5K), which did not occur in aortic CD11b$^+$F4/80$^-$ and CD45$^+$CD11b$^-$ cells (Figure S5F), and was not due to increased cell death, as we found reduced 7-AAD staining of CFH-deficient macrophages compared with controls (Figure S5G). These data led us to conclude that CFH-deficient macrophages have an intrinsic advantage to exert pro-resolving functions and may also serve as better subjects for anti-inflammatory cell clearance. In support of this notion, we found several "eat-me" signals as well as "find-me" and bridging molecules to be upregulated in CFH-deficient macrophages (Figure S5H).

Hematopoietic CFH deficiency promotes lesional efferocytosis and reduces atherosclerosis

Having demonstrated a robust expression and a crucial influence of CFH on macrophages in atherosclerotic lesions, we tested whether hematopoietic CFH affects disease progression. To overcome the limitation of hepatic CFH deficiency that instigates age-related, spontaneous nephropathies,[33] with confounding effects on lesion formation, we generated *Ldlr*$^{-/-}$ mice reconstituted with bone marrow of *Cfh*$^{+/+}$ or *Cfh*$^{-/-}$ mice and subjected them to a WTD for 12 weeks (Figure 6A). Body weights, plasma cholesterol, and triglyceride levels were unaffected between the groups (Figures S6A–S6C). Furthermore, hematopoietic CFH deficiency did not influence total CFH levels (Figure 6B) or systemic complement activation (Figures 6C and 6D); however, it resulted in a robust reduction of intact C3 content in lesions (Figure 6E) that was not due to differential C3 production, as we found comparable *C3* mRNA levels in sorted aortic macrophages (Figure S6D). Of note, C3 staining was the most prevalent in the shoulder regions of necrotic cores, which is consistent with recent findings on human plaques.[60] Importantly, *Cfh*$^{-/-}$ bone-marrow-chimeric mice developed reduced atherosclerosis in the entire aorta (Figure S6E) and in cross sections of the aortic root (Figures 6F and 6G). Furthermore, hematopoietic CFH deficiency led to a more than 80% reduction in necrotic core formation (Figure 6H). A substantial decrease in lesional TUNEL$^+$ macrophages (Figure 6J), combined with a striking reduction in the ratio of "free" to "macrophage-associated" apoptotic cells (Figure 6K), indicated enhanced lesional efferocytosis upon the loss of hematopoietic CFH, while the overall plaque macrophage content was comparable between the groups (Figure 6I). In addition, aortic macrophages from *Cfh*$^{-/-}$ bone-marrow-chimeric mice displayed heightened expression of the anti-inflammatory cytokines *Tgfb* and *Il10* (Figure S6F) and higher lesional ATG5 expression in macrophage-rich regions (Figure 6L), in line with the role of this key autophagy protein in autophagosome formation[61] and macrophage efferocytosis.[62] Of note, *Cfh*$^{-/-}$ bone-marrow-chimeric *Ldlr*$^{-/-}$ mice were also protected from hepatic inflammation, as demonstrated by decreased macrophage content (Figure S6E) and reduced *Cxcl1*, *Cxcl2*, and *Tnfa* expression in the liver (Figure S6F). Taken together, despite the abundant presence of liver-derived CFH in plasma, hematopoietic CFH deficiency markedly attenuates atherosclerosis by promoting lesional efferocytosis.

C3- and CFH-producing inflammatory aortic macrophages populate human coronary artery plaques

Having established a critical role for the local production of alternative complement in murine atherosclerosis, we turned our attention to human plaques. We started by validating CFH and C3 production by human Mo-Macs. We detected substantial secretion of CFH by human THP-1 monocytes upon IFNγ stimulation (Figure 7A) and further demonstrated high intracellular content of CFH and C3 in THP-1 Mo-Macs (Figures 7B and 7C). Next, we performed pathway analysis on key driver genes derived from an integrative genomics approach on CAD[63] and identified complement

Please cite this article in press as: Kiss et al., Cell-autonomous regulation of complement C3 by factor H limits macrophage efferocytosis and exacerbates atherosclerosis, Immunity (2023), https://doi.org/10.1016/j.immuni.2023.06.026

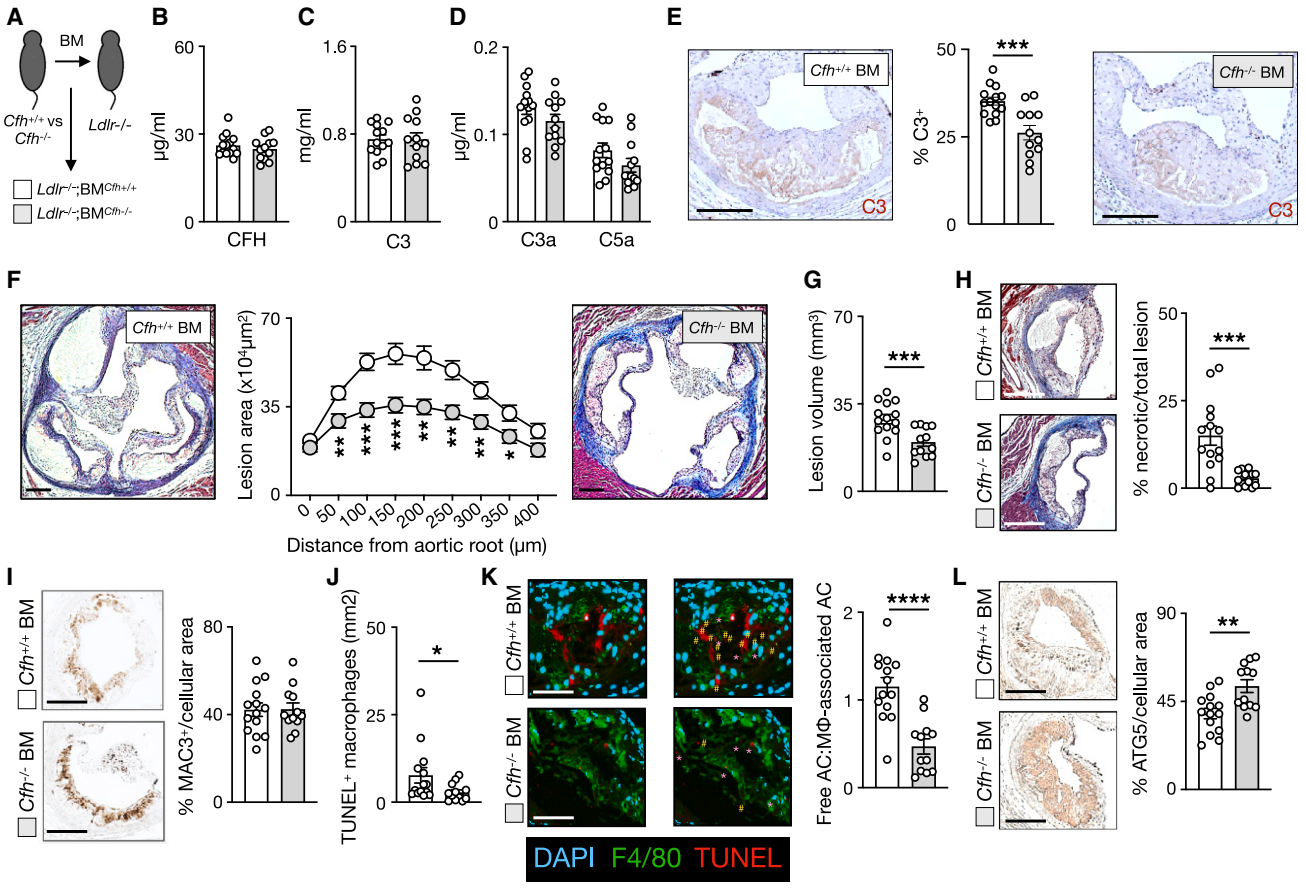

Figure 6. Hematopoietic deletion of complement factor H attenuates atherosclerosis by promoting lesional efferocytosis

(A) Schematic representation of chimeric models of hematopoietic CFH deficiency.

(A–L) Lethally irradiated *Ldlr*$^{-/-}$ mice were reconstituted with bone marrow from *Cfh*$^{+/+}$ vs. *Cfh*$^{-/-}$ mice and were fed an atherogenic diet for 12 weeks, starting 5 weeks after transplantation (n = 14 vs. n = 12).

(B–D) Total plasma (B) CFH, (C) C3, as well as (D) C3a and C5a levels, quantified by ELISA.

(E) Quantification of lesional intact C3 content. Representative images of C3-stained sections are shown. Original magnification, 50×; scale bars, 200 μm.

(F) Quantification of aortic root plaque size. Representative images of Masson's trichrome-stained sections are shown. Original magnification, 50×; scale bars, 200 μm.

(G) Measurement of lesion volume. The dot plots represent the average μm^2 of nine sections throughout the entire aortic origin, bar graphs show total lesion volume (mm^3).

(H) Assessment of necrotic core formation in cross sections at the aortic origin. Percentages of necrotic area of total lesion area are shown. Representative images are shown.

(I) Measurement of MAC-3$^+$ lesional macrophage content per total cellular area by immunohistochemistry.

(J) Quantification of dying F4/80$^+$ macrophages per cellular area (mm^2) by TUNEL staining using fluorescence microscopy.

(K) Evaluation of lesional efferocytosis. Efferocytotic capacity was determined as the ratio of free vs. macrophage-associated apoptotic cells using fluorescence microscopy. Representative images of sections stained with 4′,6-diamidino-2-phenylindole (DAPI), TUNEL, and F4/80 are shown. Yellow hashes (#) show free, while pink asterisks (*) indicate macrophage-associated apoptotic cells. Scale bars, 100 μm.

(L) Quantification of ATG5$^+$ lesional area per total cellular area by immunohistochemistry. Each symbol represents individual mice. Representative images are shown. Mean ± SEM, two-tailed Student's t tests (*p < 0.05, **p < 0.01, ***p < 0.001, ****p < 0.0001).

as one of the top CAD-relevant biological pathways (Figure 7D). To extend our observations to the cellular constituents of human atherosclerotic lesions, we performed comparative pathway analysis on aortic cell subsets from human carotid atherosclerotic plaques using the dataset published by Depuydt et al.[64] We found that genes necessary for complement activation were enriched in various macrophage populations, with notable—but lower—presence in smooth muscle cells (SMCs) too (Figure S7A). These findings were consistent with pathway analysis data obtained from our meta-analysis of murine scRNA-seq studies (Figure S7B).

To further streamline our investigation to macrophage-derived complement, we re-clustered aortic myeloid cell populations of coronary artery plaques from explanted hearts of transplant recipients.[65] Strikingly, a macrophage subset that displays C3 as one of the top differentially expressed genes (Figure 7E), hence referred to as C3^{high} inflammatory macrophages,[66] is present in plaques, occurs to be of monocyte origin based on high differential expression of *CSF1R* and *CSF3R* (Table S1), and is enriched in genes associated with IFN (especially IFNγ) and IL

Please cite this article in press as: Kiss et al., Cell-autonomous regulation of complement C3 by factor H limits macrophage efferocytosis and exacerbates atherosclerosis, Immunity (2023), https://doi.org/10.1016/j.immuni.2023.06.026

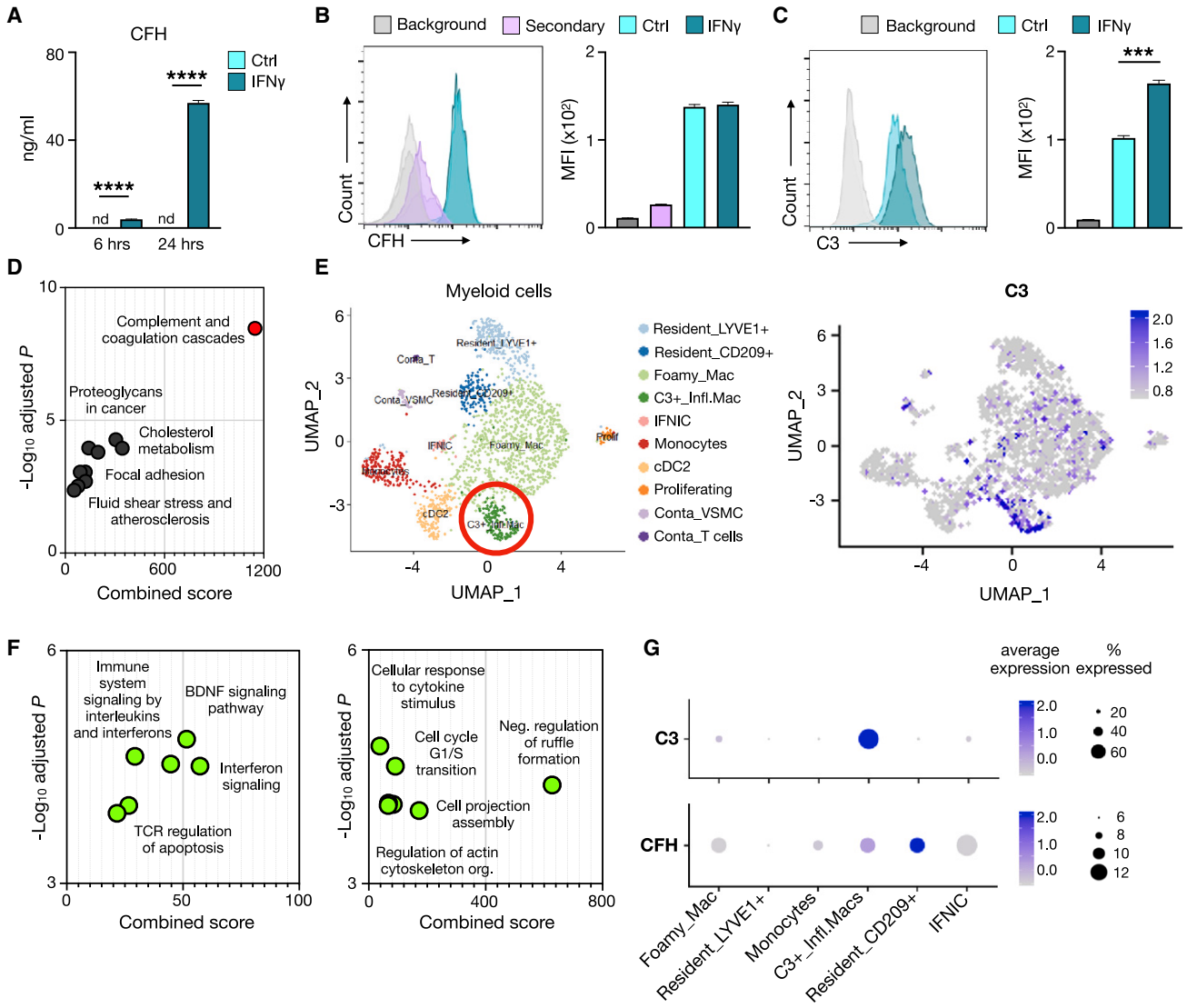

Figure 7. Complement C3- and CFH-producing inflammatory aortic macrophages populate human coronary arteries

(A) CFH secretion by untreated vs. interferon-gamma (IFNγ)-stimulated THP-1 monocytes, evaluated by ELISA.

(B and C) Representative flow cytometry histograms and bar graphs show intracellular (B) CFH and (C) C3 levels of untreated vs. IFNγ-stimulated THP-1 MoMacs evaluated by flow cytometry. Data are representative of three independent experiments.

(D) *Enrichr* analysis of coronary artery disease (CAD) candidate genes from the CAD1000G gene list, retrieved from Zhao et al.[63] The ten most overrepresented biological pathways are shown.

(E) Uniform manifold approximation and projection (UMAP) visualization of aortic myeloid cell populations from human coronary artery plaques re-clustered from the raw data published by Wirka et al.[65] Red circle highlights a distinct population of C3^{high} inflammatory macrophages. Right: *C3* gene expression profile is shown in human aortic myeloid cell populations, average expression level (log_2 scale) indicated by saturation of blue (dark blue is highest, with minimum scaling to 0). IFNICs, interferon-response macrophages; DC, dendritic cell; VSMCs, vascular smooth muscle cells.

(F) *Enrichr* analysis of the top differentially expressed genes enriched in C3^{high} inflammatory macrophages. The most overrepresented biological pathways and molecular processes are shown.

(G) Expression of *C3* and *CFH* in single cells from human aortic myeloid cell subsets. Average expression level (log_2 scale) indicated by saturation of blue (see above). Dot size represents relative percentage of cells within the respective cluster that expressed the corresponding genes. Mean ± SEM, two-tailed Student's t tests (***$p < 0.001$, ****$p < 0.0001$).

(*IL10RA, IL13RA1, IL18*) signaling (Figure 7F). We identified multiple biological pathways overrepresented in this cluster (regulation of ruffle formation, cell projection assembly, and the regulation of cytoskeleton organization) that may indicate a role for C3^{high} macrophages in apoptotic cell engulfment (Figure 7F).

Supporting our murine findings, *C5* expression was undetectable in C3^{high} macrophages and was minute among the distinct myeloid cell types (Figure S7C). Importantly, however, we found that C3^{high} macrophages display a considerable co-expression of *CFH* (Figure 7G). Furthermore, we distinguished CD209^{+} resident-like macrophages as the primary local source of CFH with

Please cite this article in press as: Kiss et al., Cell-autonomous regulation of complement C3 by factor H limits macrophage efferocytosis and exacerbates atherosclerosis, Immunity (2023), https://doi.org/10.1016/j.immuni.2023.06.026

low *C3* expression (Figure 7G). Thus, differential expression of *C3* and its main regulator may result in subset-specific functional differences with respect to complement activation. These data unravel the presence of a distinct C3/CFH-expressing inflammatory macrophage subset in human atherosclerotic plaques and identifies an additional layer of potential local complement regulation. Of note, *VSIG4* expression was also abundant among $C3^{high}$ macrophages (Figure S7D), and its downregulation in aortic macrophages was associated with a symptomatic lesion phenotype (Figure S7E). Taken together, our findings reveal the existence and functional relevance of complement-producing macrophages in both murine and human atherosclerotic plaques.

DISCUSSION

Our findings describe an immune-regulatory mechanism wherein cell-autonomous complement controls cytoprotective functions in monocyte-derived macrophages during inflammation. This is in line with the notion that early C3 activation evolved to be a part of an intracellular sensor system that armors individual cells against cellular stress and injury.[67,68] Leukocyte adhesion molecule-1 (LFA-1)-dependent C3 licensing is a cardinal feature of human immune cells upon diapedesis.[69] Thus, our observations that specifically $Ly6C^{hi}$ monocytes carry their own set of alternative complement proteins to the site of inflammation aligns with a general role for intracellular C3 in tissue immune cell biology.

Although the protective role of classical complement via C1q is well-described in atherosclerosis,[70–72] the effect of alternative complement on lesion formation is less evident. Global C3 deficiency promotes plaque formation and results in greater lesional macrophage content.[27,73] These observations are consistent with our current report that enhanced local C3 activation promotes lesional efferocytosis and protects from atherosclerosis; however, the former studies did not address the contribution of systemic vs. locally produced C3. Notably, $Sca\text{-}1^{+}$ SMCs are considered a relevant source of C3 in atherosclerotic plaques, where they home near the necrotic core.[60] This suggests that non-leukocytes can also contribute to local C3 production and, if taken up, SMC-derived C3 may represent a paracrine layer of regulation in complement-mediated efferocytosis.

Here, we identify that CFH, the canonical repressor of alternative complement activation in serum, is highly upregulated in inflammatory monocytes and macrophages, where it suppresses C3 cleavage. The exact mechanism of action requires further investigation; however, CFH may accelerate the decay of an intracellular C3 convertase[74] or inhibit a cell-specific protease with C3-cleaving ability.[75] Importantly, we provide evidence for the non-redundant role of macrophage-derived CFH in regulating C3-dependent efferocytosis during atherosclerosis, as we show that selective deficiency of CFH in the hematopoietic compartment leads to a robust decrease in lesion size and necrotic area. Moreover, the impact of macrophage-derived CFH on atherosclerosis appears to be dominant over the effect of liver-derived CFH, as mice with global CFH deficiency still displayed a decrease in necrotic core formation, despite having similar lesion size compared with controls. The lack of difference in lesion size between $Cfh^{+/+}Ldlr^{-/-}$ and $Cfh^{-/-}Ldlr^{-/-}$ mice is likely attributed to the pro-atherogenic effect of global CFH deficiency through excessive systemic complement activation. Thus, dissecting the layers of CFH activity in a compartmentalized manner allowed us to identify opposing effects of systemic vis-à-vis local complement activation in atherosclerosis. The local availability of macrophage-derived CFH may depend on the extent of accumulating apoptotic cells that are bound by CFH.[32,76] In turn, this may limit the amount of secreted CFH for re-uptake by macrophages and thereby indirectly modulate intracellular complement activity.[77] Thus, our data suggest a model in which self-derived CFH actively controls the pro-resolving machinery of infiltrating macrophages.

Mirroring our murine data, we identify a distinct inflammatory monocyte-derived macrophage subset in human atherosclerotic plaques with substantial *C3* and *CFH* expression. Although further investigation is warranted to decipher their functional relevance, $C3^{high}$ macrophages do display a preferential enrichment for genes associated with cytoskeletal remodeling that is a prerequisite for efficient apoptotic cell internalization. Furthermore, in accordance with our murine findings illustrating the inability of $Ly6C^{hi}$ Mo-Macs to produce C5 and to activate complement downstream of C3, human $C3^{high}$ plaque macrophages were also devoid of *C5* expression (although low levels of *C5* could be detected in other myeloid subsets). Taken together, these observations—further bolstered by the detrimental role of macrophage-specific C5aR1 signaling in atherosclerosis[78]—strengthen our rationale that C3 and C5 activation might be uncoupled on the cellular level.[68] Supporting this notion, in a recent study devoted to promoting regression of atherosclerosis via macrophage remodeling,[79] cyclodextrin treatment of human plaques led to increased *C3* but decreased *CFH* expression, concomitant with *C5* downregulation. Thus, divergent expression of *C5* and *C3* accompanied by reduced *CFH* expression reflects a pro-resolving gene signature in human plaques—in line with our murine studies demonstrating increased cell-associated C3 consumption but decreased C5 activation upon resolution. In aggregate, we propose that the specific repertoire of complement components expressed by macrophages determines their overall functional consequences on atherosclerotic lesion formation.

Besides atherosclerosis, the accumulation of apoptotic macrophages is a major characteristic of many other chronic inflammatory diseases. Thus, it is tempting to assume that our findings on cell-autonomous complement regulation are also applicable to Mo-Macs in other diseases characterized by low-grade, non-resolving inflammation, such as obesity. In perspective, tissue- or even cell-specific modulation of local complement activation, i.e., via targeting macrophage-derived CFH, could be potentially harnessed to promote pro-resolving molecular mechanisms in chronic inflammatory diseases.

In summary, we identify a mechanism by which uncontrolled cell-autonomous C3 activation resulting from CFH deficiency induces cytoprotective autophagy in macrophages, promotes lesional efferocytosis, and mitigates atherosclerosis development. The need for alternative strategies in treating atherosclerotic vascular diseases—such as inducing resolution—is apparent, as broad anti-inflammatory drug therapies can potentially suppress host defense and lead to fatal infections.[80] Our findings indicate that targeting cell-associated complement regulation

may provide novel opportunities in next-generation therapeutics against chronic inflammatory diseases without dampening host defense mechanisms.

Limitations of the study

This study reveals the existence and functional relevance of local complement regulation by CFH in atherosclerotic plaques. Our findings propose that the specific repertoire of complement components in macrophages licenses their overall inflammatory responses and subsequent pro-resolving phenotype. In this scenario, a cell-specific intracellular C3 convertase that is overactivated in the absence of CFH may aid LAP-mediated apoptotic cell clearance by enhanced intracellular coating of the engulfed material. However, the characterization of this convertase activity was not the focus of our current manuscript and, thus, our data do not allow for exact dissection of intracellular vs. autocrine regulatory effects. Therefore, we refer to it as a "cell-autonomous" CFH effect, while placing it in juxtaposition with systemic complement modulation.

We further demonstrate that enhanced cell-autonomous C3 consumption upon CFH deficiency does not culminate in downstream C5 activation in Mo-Macs. Although we show that Mo-Macs do not produce C5, macrophage C5aR1 signaling impacts atherosclerosis, possibly mediated by C5 of other cellular sources or via intrinsic C5 in a different macrophage subset. These observations bolster the notion that C3 and C5 activation might be uncoupled on the cellular level; however, additional work is needed to prove this.

Lastly, while our data unravel the presence of a distinct C3/CFH-expressing inflammatory macrophage subset in human atherosclerotic plaques, further investigation is warranted to establish the functional relevance of complement-producing macrophages in human atherosclerosis and other chronic inflammatory diseases.

STAR★METHODS

Detailed methods are provided in the online version of this paper and include the following:

- KEY RESOURCES TABLE
- RESOURCE AVAILABILITY
  - Lead contact
  - Materials availability
  - Data and code availability
- EXPERIMENTAL MODEL AND SUBJECT DETAILS
  - Mice
- METHOD DETAILS
  - Diets
  - Evaluation of atherosclerosis
  - Immunohistochemistry in aortic root lesions
  - Quantification of lesional apoptosis and *in situ* efferocytosis assay
  - Liver Histology
  - Primary cell isolation, flourescence-activated cell sorting and flow cytometry
  - Sorting of aortic macrophages and RNA sequencing
  - Meta-analysis of single cell-RNA sequencing data from atherosclerotic mouse aorta
  - Plasma cholesterol and triglyceride quantification
  - Quantification of complement component levels
  - Quantification of secreted interleukin-1 beta and peritoneal CXCL1 levels
  - Antibody measurements
  - Cell lines
  - Generation and stimulation of THP-1-derived macrophages
  - Generation of CMFDA-labeled apoptotic RAW 264.7 macrophages
  - *Ex vivo* efferocytosis assays
  - C3 supplementation studies
  - LC3 conversion assay
  - Generation and stimulation of bone-marrow-derived macrophages
  - Gene expression analyses
  - Single-cell RNA sequencing
  - Bulk RNA-sequencing
  - Human single-cell RNA sequencing analysis
  - Statistical analysis

SUPPLEMENTAL INFORMATION

Supplemental information can be found online at https://doi.org/10.1016/j.immuni.2023.06.026.

ACKNOWLEDGMENTS

We thank Thomas Winkler-Penz and the Biomedical Sequencing Facility as well as the Anna Spiegel Animal Facility, especially Astrid Fabry for excellent technical support. We are grateful to Christina Schüller and Robert Kralovics for providing us with CD45.1 mice. We thank Arif Yurdagul Jr. and Ira Tabas for providing us with the *in situ* efferocytosis assay protocol. This work was supported by the doctoral program Cell Communication in Health and Disease (CCHD) (DK W1205-B09, to M.G.K. and F.P.), by SFB Lipotox F30 (F 3015-B19), both funded by the Austrian Science Fund (FWF), by the Leducq Foundation (TNE-20CVD03) to C.J.B., and by the Deutsche Forschungsgemeinschaft (DFG, German Research Foundation; project number 324392634-TR221 to A.Z., 458539578 and 471705758 to C.C., and 453989101-SFB1525 and 432915089 to A.Z. and C.C.).

AUTHOR CONTRIBUTIONS

Conceptualization, M.G.K., N.P.-M., and C.J.B.; data acquisition, M.G.K., N.P.-M., F.P., D.T., T.H., M.T., M.-S.N., L.G., M.O.-K., and A.H.; data analysis, M.G.K., N.P.-M., F.P., D.T., and T.H.; sequencing data interpretation and analysis, H.Q.D., K.L., M.S., N.F., A.Z., and C.C.; generation of *Cfh*$^{-/-}$ mice, M.C.P.; supervision, S.K., F.G., C.B., F.K.S., K.L., A.Z., C.C., C.K., Z.M., and C.J.B.; manuscript writing, M.G.K. and C.J.B.; manuscript editing, M.G.K., N.P.-M., F.P., D.T., T.H., H.Q.D., M.-S.N., L.G., M.O.-K., M.S., N.F., A.H., S.K., F.G., M.C.P., C.B., F.K.S., K.L., A.Z., C.C., C.K., Z.M., and C.J.B.

DECLARATION OF INTERESTS

The authors declare no competing interests.

INCLUSION AND DIVERSITY

We support inclusive, diverse, and equitable conduct of research.

Received: March 22, 2021
Revised: October 21, 2022
Accepted: June 30, 2023
Published: July 26, 2023

REFERENCES

1. Walport, M.J. (2001). Advances in immunology between INNATE AND ADAPTIVE. Engl. J. *344*, 1140–1144. https://doi.org/10.1056/NEJM200104123441506.
2. Walport, M.J. (2001). Complement. First of two parts. N. Engl. J. Med. *344*, 1058–1066. https://doi.org/10.1056/NEJM200104053441406.
3. Holers, V.M. (2014). Complement and its receptors: new insights into human disease. Annu. Rev. Immunol. *32*, 433–459. https://doi.org/10.1146/annurev-immunol-032713-120154.
4. Elvington, M., Liszewski, M.K., Bertram, P., Kulkarni, H.S., and Atkinson, J.P. (2017). A C3 (H2O) recycling pathway is a component of the intracellular complement system. J. Clin. Invest. *127*, 970–981. https://doi.org/10.1172/JCI89412.
5. Zipfel, P.F., and Skerka, C. (2009). Complement regulators and inhibitory proteins. Nat. Rev. Immunol. *9*, 729–740. https://doi.org/10.1038/nri2620.
6. Morgan, B.P., and Gasque, P. (1997). Extrahepatic complement biosynthesis: where, when and why? Clin. Exp. Immunol. *107*, 1–7. https://doi.org/10.1046/j.1365-2249.1997.d01-890.x.
7. Naughton, M.A., Botto, M., Carter, M.J., Alexander, G.J., Goldman, J.M., and Walport, M.J. (1996). Extrahepatic secreted complement C3 contributes to circulating C3 levels in humans. J. Immunol. *156*, 3051–3056.
8. Elvington, M., Liszewski, M.K., and Atkinson, J.P. (2016). Evolution of the complement system: from defense of the single cell to guardian of the intravascular space. Immunol. Rev. *274*, 9–15. https://doi.org/10.1111/imr.12474.
9. Hess, C., and Kemper, C. (2016). Complement-mediated regulation of metabolism and basic cellular processes. Immunity *45*, 240–254. https://doi.org/10.1016/j.immuni.2016.08.003.
10. Frišćić, J., Böttcher, M., Reinwald, C., Bruns, H., Wirth, B., Popp, S.J., Walker, K.I., Ackermann, J.A., Chen, X., Turner, J., et al. (2021). The complement system drives local inflammatory tissue priming by metabolic reprogramming of synovial fibroblasts. Immunity *54*, 1002–1021.e10. https://doi.org/10.1016/j.immuni.2021.03.003.
11. Lalli, P.N., Strainic, M.G., Yang, M., Lin, F., Medof, M.E., and Heeger, P.S. (2008). Locally produced C5a binds to T cell expressed C5aR to enhance effector T-cell expansion by limiting antigen-induced apoptosis. Blood *112*, 1759–1766. https://doi.org/10.1182/blood-2008-04-151068.
12. Strainic, M.G., Liu, J., Huang, D., An, F., Lalli, P.N., Muqim, N., Shapiro, V.S., Dubyak, G.R.R., Heeger, P.S., and Medof, M.E. (2008). Locally produced complement fragments C5a and C3a provide both costimulatory and survival signals to naive CD4+ T cells. Immunity *28*, 425–435. https://doi.org/10.1016/j.immuni.2008.02.001.
13. Le Friec, G., Sheppard, D., Whiteman, P., Karsten, C.M., Shamoun, S.A.T., Laing, A., Bugeon, L., Dallman, M.J., Melchionna, T., Chillakuri, C., et al. (2012). The CD46-Jagged1 interaction is critical for human T H 1 immunity. Nat. Immunol. *13*, 1213–1221. https://doi.org/10.1038/ni.2454.
14. Sorbara, M.T., Foerster, E.G., Tsalikis, J., Abdel-Nour, M., Mangiapane, J., Sirluck-Schroeder, I., Tattoli, I., van Dalen, R., Isenman, D.E., Rohde, J.R., et al. (2018). Complement C3 drives autophagy-dependent restriction of cyto-invasive bacteria. Cell Host Microbe *23*, 644–652.e5. https://doi.org/10.1016/j.chom.2018.04.008.
15. Tam, J.C.H., Bidgood, S.R., McEwan, W.A., and James, L.C. (2014). Intracellular sensing of complement C3 activates cell autonomous immunity. Science *345*, 1256070. https://doi.org/10.1126/science.1256070.
16. Baudino, L., Sardini, A., Ruseva, M.M., Fossati-Jimack, L., Cook, H.T., Scott, D., Simpson, E., and Botto, M. (2014). C3 opsonization regulates endocytic handling of apoptotic cells resulting in enhanced T-cell responses to cargo-derived antigens. Proc. Natl. Acad. Sci. USA *111*, 1503–1508. https://doi.org/10.1073/pnas.1316877111.
17. Liszewski, M.K., Kolev, M., Le Friec, G., Leung, M., Bertram, P.G., Fara, A.F., Subias, M., Pickering, M.C., Drouet, C., Meri, S., et al. (2013). Intracellular complement activation sustains T cell homeostasis and mediates effector differentiation. Immunity *39*, 1143–1157. https://doi.org/10.1016/j.immuni.2013.10.018.
18. Kolev, M., Dimeloe, S., Le Friec, G., Navarini, A., Arbore, G., Povoleri, G.A., Fischer, M., Belle, R., Loeliger, J., Develioglu, L., et al. (2015). Complement regulates nutrient influx and metabolic reprogramming during Th1 cell responses. Immunity *42*, 1033–1047. https://doi.org/10.1016/j.immuni.2015.05.024.
19. Arbore, G., West, E.E., Spolski, R., Robertson, A.A.B., Klos, A., Rheinheimer, C., Dutow, P., Woodruff, T.M., Yu, Z.X., O'Neill, L.A., et al. (2016). T helper 1 immunity requires complement-driven NLRP3 inflammasome activity in CD4+ T cells. Science *352*, aad1210. https://doi.org/10.1126/science.aad1210.
20. Weber, C., and Noels, H. (2011). Atherosclerosis: current pathogenesis and therapeutic options. Nat. Med. *17*, 1410–1422. https://doi.org/10.1038/nm.2538.
21. Moore, K.J., and Tabas, I. (2011). Macrophages in the pathogenesis of atherosclerosis. Cell *145*, 341–355. https://doi.org/10.1016/j.cell.2011.04.005.
22. Kiss, M.G., and Binder, C.J. (2022). The multifaceted impact of complement on atherosclerosis. Atherosclerosis *351*, 29–40. https://doi.org/10.1016/j.atherosclerosis.2022.03.014.
23. Cochain, C., Vafadarnejad, E., Arampatzi, P., Pelisek, J., Winkels, H., Ley, K., Wolf, D., Saliba, A.E., and Zernecke, A. (2018). Single-cell RNA-seq reveals the transcriptional landscape and heterogeneity of aortic macrophages in murine atherosclerosis. Circ. Res. *122*, 1661–1674. https://doi.org/10.1161/CIRCRESAHA.117.312509.
24. Winkels, H., Ehinger, E., Vassallo, M., Buscher, K., Dinh, H.Q., Kobiyama, K., Hamers, A.A.J., Cochain, C., Vafadarnejad, E., Saliba, A.E., et al. (2018). Atlas of the immune cell repertoire in mouse atherosclerosis defined by single-cell RNA-sequencing and mass cytometry. Circ. Res. *122*, 1675–1688. https://doi.org/10.1161/CIRCRESAHA.117.312513.
25. McArdle, S., Buscher, K., Ghosheh, Y., Pramod, A.B., Miller, J., Winkels, H., Wolf, D., and Ley, K. (2019). Migratory and dancing macrophage subsets in atherosclerotic lesions. Circ. Res. *125*, 1038–1051. https://doi.org/10.1161/CIRCRESAHA.119.315175.
26. Oksjoki, R., Kovanen, P.T., Mäyränpää, M.I., Laine, P., Blom, A.M., Meri, S., and Pentikäinen, M.O. (2007). Complement regulation in human atherosclerotic coronary lesions. Immunohistochemical evidence that C4b-binding protein negatively regulates the classical complement pathway, and that C5b-9 is formed via the alternative complement pathway. Atherosclerosis *192*, 40–48. https://doi.org/10.1016/j.atherosclerosis.2006.06.013.
27. Buono, C., Come, C.E., Witztum, J.L., Maguire, G.F., Connelly, P.W., Carroll, M., and Lichtman, A.H. (2002). Influence of C3 deficiency on atherosclerosis. Circulation *105*, 3025–3031. https://doi.org/10.1161/01.CIR.0000019584.04929.83.
28. Speidl, W.S., Kastl, S.P., Huber, K., and Wojta, J. (2011). Complement in atherosclerosis: friend or foe? J. Thromb. Haemost. *9*, 428–440. https://doi.org/10.1111/j.1538-7836.2010.04172.x.
29. Pickering, M.C., and Cook, H.T. (2008). Translational Mini-Review Series on Complement factor H: renal diseases associated with complement factor H: novel insights from humans and animals. Clin. Exp. Immunol. *151*, 210–230. https://doi.org/10.1111/j.1365-2249.2007.03574.x.
30. Ferreira, V.P., Pangburn, M.K., and Cortés, C. (2010). Complement control protein factor H: the good, the bad, and the inadequate. Mol. Immunol. *47*, 2187–2197. https://doi.org/10.1016/j.molimm.2010.05.007.
31. Zipfel, P.F. (2001). Complement factor H: physiology and pathophysiology. Semin. Thromb. Hemost. *27*, 191–199. https://doi.org/10.1055/s-2001-15248.
32. Weismann, D., Hartvigsen, K., Lauer, N., Bennett, K.L., Scholl, H.P.N., Charbel Issa, P.C., Cano, M., Brandstätter, H., Tsimikas, S., Skerka, C., et al. (2011). Complement factor H binds malondialdehyde epitopes and protects from oxidative stress. Nature *478*, 76–81. https://doi.org/10.1038/nature10449.

33. Pickering, M.C., Cook, H.T., Warren, J., Bygrave, A.E., Moss, J., Walport, M.J., and Botto, M. (2002). Uncontrolled C3 activation causes membranoproliferative glomerulonephritis in mice deficient in complement factor H. Nat. Genet. *31*, 424–428. https://doi.org/10.1038/ng912.

34. De Córdoba, S.R., and De Jorge, E.G. (2008). Translational mini-review series on complement factor H: genetics and disease associations of human complement factor H. Clin. Exp. Immunol. *151*, 1–13. https://doi.org/10.1111/j.1365-2249.2007.03552.x.

35. Oksjoki, R., Jarva, H., Kovanen, P.T., Laine, P., Meri, S., and Pentikäinen, M.O. (2003). Association between complement factor H and proteoglycans in early human coronary atherosclerotic lesions: implications for local regulation of complement activation. Arterioscler. Thromb. Vasc. Biol. *23*, 630–636. https://doi.org/10.1161/01.ATV.0000057808.91263.A4.

36. Kiss, M.G., Ozsvár-Kozma, M., Porsch, F., Göderle, L., Papac-Miličević, N., Bartolini-Gritti, B., Tsiantoulas, D., Pickering, M.C., and Binder, C.J. (2019). Complement factor H modulates splenic B cell development and limits autoantibody production. Front. Immunol. *10*, 1607. https://doi.org/10.3389/fimmu.2019.01607.

37. Leung, V.W.Y., Yun, S., Botto, M., Mason, J.C., Malik, T.H., Song, W., Paixao-Cavalcante, D., Pickering, M.C., Boyle, J.J., and Haskard, D.O. (2009). Decay-accelerating factor suppresses complement C3 activation and retards atherosclerosis in low-density lipoprotein receptor-deficient mice. Am. J. Pathol. *175*, 1757–1767. https://doi.org/10.2353/ajpath.2009.090183.

38. Skaggs, B.J., Hahn, B.H., and McMahon, M. (2012). Accelerated atherosclerosis in patients with SLE - Mechanisms and management. Nat. Rev. Rheumatol. *8*, 214–223. https://doi.org/10.1038/nrrheum.2012.14.

39. Yurdagul, A., Doran, A.C., Cai, B., Fredman, G., and Tabas, I.A. (2018). Mechanisms and consequences of defective efferocytosis in atherosclerosis. Front. Cardiovasc. Med. *4*, 1–10. https://doi.org/10.3389/fcvm.2017.00086.

40. Calippe, B., Augustin, S., Beguier, F., Charles-Messance, H., Poupel, L., Conart, J.B., Hu, S.J., Lavalette, S., Fauvet, A., Rayes, J., et al. (2017). Complement factor H inhibits CD47-mediated resolution of inflammation. Immunity *46*, 261–272. https://doi.org/10.1016/j.immuni.2017.01.006.

41. Kojima, Y., Volkmer, J.P., McKenna, K., Civelek, M., Lusis, A.J., Miller, C.L., Direnzo, D., Nanda, V., Ye, J., Connolly, A.J., et al. (2016). CD47-blocking antibodies restore phagocytosis and prevent atherosclerosis. Nature *536*, 86–90. https://doi.org/10.1038/nature18935.

42. Ghosn, E.E., Cassado, A.A., Govoni, G.R., Fukuhara, T., Yang, Y., Monack, D.M., Bortoluci, K.R., Almeida, S.R., Herzenberg, L.A., and Herzenberg, L.A. (2010). Two physically, functionally, and developmentally distinct peritoneal macrophage subsets. Proc. Natl. Acad. Sci. USA *107*, 2568–2573. https://doi.org/10.1073/pnas.0915000107.

43. Bannenberg, G.L., Chiang, N., Ariel, A., Arita, M., Tjonahen, E., Gotlinger, K.H., Hong, S., and Serhan, C.N. (2005). Molecular circuits of resolution: formation and actions of resolvins and protectins. J. Immunol. *174*, 4345–4355. https://doi.org/10.4049/jimmunol.174.7.4345.

44. Ricklin, D., Reis, E.S., and Lambris, J.D. (2016). Complement in disease: a defence system turning offensive. Nat. Rev. Nephrol. *12*, 383–401. https://doi.org/10.1038/nrneph.2016.70.

45. Chen, E.Y., Tan, C.M., Kou, Y., Duan, Q., Wang, Z., Meirelles, G.V., Clark, N.R., and Ma'ayan, A. (2013). Enrichr: interactive and collaborative HTML5 gene list enrichment analysis tool. BMC Bioinformatics *14*, 128. https://doi.org/10.1186/1471-2105-14-128.

46. Kuleshov, M.V., Jones, M.R., Rouillard, A.D., Fernandez, N.F., Duan, Q., Wang, Z., Koplev, S., Jenkins, S.L., Jagodnik, K.M., Lachmann, A., et al. (2016). Enrichr: a comprehensive gene set enrichment analysis web server 2016 update. Nucleic Acids Res. *44*, W90–W97. https://doi.org/10.1093/nar/gkw377.

47. Jaitin, D.A., Adlung, L., Thaiss, C.A., Weiner, A., Li, B., Descamps, H., Lundgren, P., Bleriot, C., Liu, Z., Deczkowska, A., et al. (2019). Lipid-associated macrophages control metabolic homeostasis in a Trem2-dependent manner. Cell *178*, 686–698.e14. https://doi.org/10.1016/j.cell.2019.05.054.

48. Remmerie, A., Martens, L., Thoné, T., Castoldi, A., Seurinck, R., Pavie, B., Roels, J., Vanneste, B., De Prijck, S., Vanhockerhout, M., et al. (2020). Osteopontin expression identifies a subset of recruited macrophages distinct from Kupffer cells in the fatty liver. Immunity *53*, 641–657.e14. https://doi.org/10.1016/j.immuni.2020.08.004.

49. Ramachandran, P., Dobie, R., Wilson-Kanamori, J.R., Dora, E.F., Henderson, B.E.P., Luu, N.T., Portman, J.R., Matchett, K.P., Brice, M., Marwick, J.A., et al. (2019). Resolving the Fibrotic Niche of Human Liver Cirrhosis at Single-Cell Level (Springer). https://doi.org/10.1038/s41586-019-1631-3.

50. Hendrikx, T., Porsch, F., Kiss, M.G., Rajcic, D., Papac-Miličević, N., Hoebinger, C., Goederle, L., Hladik, A., Shaw, L.E., Horstmann, H., et al. (2022). Soluble TREM2 levels reflect the recruitment and expansion of TREM2+ macrophages that localize to fibrotic areas and limit NASH. J. Hepatol. *77*, 1373–1385. https://doi.org/10.1016/j.jhep.2022.06.004.

51. Gluschko, A., Herb, M., Wiegmann, K., Krut, O., Neiss, W.F., Utermöhlen, O., Krönke, M., and Schramm, M. (2018). The β2 integrin Mac-1 induces protective LC3-associated phagocytosis of Listeria monocytogenes. Cell Host Microbe *23*, 324–337.e5. https://doi.org/10.1016/j.chom.2018.01.018.

52. Kim, K.H., Choi, B.K., Kim, Y.H., Han, C., Oh, H.S., Lee, D.G., and Kwon, B.S. (2016). Extracellular stimulation of VSIG4/complement receptor Ig suppresses intracellular bacterial infection by inducing autophagy. Autophagy *12*, 1647–1659. https://doi.org/10.1080/15548627.2016.1196314.

53. Martinez, J., Almendinger, J., Oberst, A., Ness, R., Dillon, C.P., Fitzgerald, P., Hengartner, M.O., and Green, D.R. (2011). Microtubule-associated protein 1 light chain 3 alpha (LC3)-associated phagocytosis is required for the efficient clearance of dead cells. Proc. Natl. Acad. Sci. USA *108*, 17396–17401. https://doi.org/10.1073/pnas.1113421108.

54. King, B.C., Kulak, K., Krus, U., Rosberg, R., Golec, E., Wozniak, K., Gomez, M.F., Zhang, E., O'Connell, D.J., Renström, E., et al. (2019). Complement Component C3 is highly expressed in human pancreatic islets and prevents β cell death via ATG16L1 interaction and autophagy regulation. Cell Metab. *29*, 202–210.e6. https://doi.org/10.1016/j.cmet.2018.09.009.

55. Jacquin, E., Leclerc-Mercier, S., Judon, C., Blanchard, E., Fraitag, S., and Florey, O. (2017). Pharmacological modulators of autophagy activate a parallel noncanonical pathway driving unconventional LC3 lipidation. Autophagy *13*, 854–867. https://doi.org/10.1080/15548627.2017.1287653.

56. Wang, F., Zhang, C., Dai, L., Zhang, Y., Wang, Y., Hao, Y., Ji, S., Xu, Z., Han, N., Chen, H., et al. (2020). Bafilomycin A1 Accelerates Chronic Refractory Wound Healing in db/db Mice. BioMed Res. Int. *2020*, 6265701. https://doi.org/10.1155/2020/6265701.

57. Yuan, N., Song, L., Zhang, S., Lin, W., Cao, Y., Xu, F., Fang, Y., Wang, Z., Zhang, H., Li, X., et al. (2015). Bafilomycin A1 targets both autophagy and apoptosis pathways in pediatric B-cell acute lymphoblastic leukemia. Haematologica *100*, 345–356. https://doi.org/10.3324/haematol.2014.113324.

58. Swirski, F.K., and Nahrendorf, M. (2013). Leukocyte behavior in. Atherosclerosis *161*, 161–166. https://doi.org/10.1126/science.1230719.

59. Zernecke, A., Winkels, H., Cochain, C., Williams, J.W., Wolf, D., Soehnlein, O., Robbins, C.S., Monaco, C., Park, I., McNamara, C.A., et al. (2020). Meta-analysis of leukocyte diversity in atherosclerotic mouse aortas. Circ. Res. *127*, 402–426. https://doi.org/10.1161/CIRCRESAHA.120.316903.

60. Wang, Y., Nanda, V., Direnzo, D., Ye, J., Xiao, S., Kojima, Y., Howe, K.L., Jarr, K.U., Flores, A.M., Tsantilas, P., et al. (2020). Clonally expanding smooth muscle cells promote atherosclerosis by escaping efferocytosis and activating the complement cascade. Proc. Natl. Acad. Sci. USA *117*, 15818–15826. https://doi.org/10.1073/pnas.2006348117.

61. Dikic, I., and Elazar, Z. (2018). Mechanism and medical implications of mammalian autophagy. Nat. Rev. Mol. Cell Biol. *19*, 349–364. https://doi.org/10.1038/s41580-018-0003-4.

62. Liao, X., Sluimer, J.C., Wang, Y., Subramanian, M., Brown, K., Pattison, J.S., Robbins, J., Martinez, J., and Tabas, I. (2012). Macrophage autophagy plays a protective role in advanced atherosclerosis. Cell Metab. *15*, 545–553. https://doi.org/10.1016/j.cmet.2012.01.022.

63. Zhao, Y., Chen, J., Freudenberg, J.M., Meng, Q., Rajpal, D.K., and Yang, X. (2016). Network-based identification and prioritization of key regulators of coronary artery disease loci. Arterioscler. Thromb. Vasc. Biol. *36*, 928–941. https://doi.org/10.1161/ATVBAHA.115.306725.

64. Depuydt, M.A.C., Prange, K.H.M., Slenders, L., Örd, T., Elbersen, D., Boltjes, A., De Jager, S.C.A., Asselbergs, F.W., De Borst, G.J., Aavik, E., et al. (2020). Microanatomy of the human atherosclerotic plaque by single-cell transcriptomics. Circ. Res. *127*, 1437–1455. https://doi.org/10.1161/CIRCRESAHA.120.316770.

65. Wirka, R.C., Wagh, D., Paik, D.T., Pjanic, M., Nguyen, T., Miller, C.L., Kundu, R., Nagao, M., Coller, J., Koyano, T.K., et al. (2019). Atheroprotective roles of smooth muscle cell phenotypic modulation and the TCF21 disease gene as revealed by single-cell analysis. Nat. Med. *25*, 1280–1289. https://doi.org/10.1038/s41591-019-0512-5.

66. Zernecke, A., Erhard, F., Weinberger, T., Schulz, C., Ley, K., Saliba, A.E., and Cochain, C. (2022). Integrated single-cell analysis based classification of vascular mononuclear phagocytes in mouse and human atherosclerosis. Cardiovasc. Res. https://doi.org/10.1093/cvr/cvac161.

67. Kolev, M., and Kemper, C. (2017). Keeping it all going-complement meets metabolism. Front. Immunol. *8*, 1. https://doi.org/10.3389/fimmu.2017.00001.

68. West, E.E., and Kemper, C. (2019). Complement and T cell metabolism: food for thought. Immunometabolism *1*, e190006. https://doi.org/10.20900/immunometab20190006.

69. Kolev, M., West, E.E., Kunz, N., Chauss, D., Moseman, E.A., Rahman, J., Freiwald, T., Balmer, M.L., Lötscher, J., Dimeloe, S., et al. (2020). Diapedesis-induced integrin signaling via LFA-1 facilitates tissue immunity by inducing intrinsic complement C3 expression in immune cells. Immunity *52*, 513–527.e8. https://doi.org/10.1016/j.immuni.2020.02.006.

70. Bhatia, V.K., Yun, S., Leung, V., Grimsditch, D.C., Benson, G.M., Botto, M.B., Boyle, J.J., and Haskard, D.O. (2007). Complement C1q reduces early atherosclerosis in low-density lipoprotein receptor-deficient mice. Am. J. Pathol. *170*, 416–426. https://doi.org/10.2353/ajpath.2007.060406.

71. Lewis, M.J., Malik, T.H., Ehrenstein, M.R., Boyle, J.J., Botto, M., and Haskard, D.O. (2009). Immunoglobulin M is required for protection against atherosclerosis in low-density lipoprotein receptor-deficient mice. Circulation *120*, 417–426. https://doi.org/10.1161/CIRCULATIONAHA.109.868158.

72. Yin, C., Ackermann, S., Ma, Z., Mohanta, S.K., Zhang, C., Li, Y., Nietzsche, S., Westermann, M., Peng, L., Hu, D., et al. (2019). ApoE attenuates unresolvable inflammation by complex formation with activated C1q. Nat. Med. *25*, 496–506. https://doi.org/10.1038/s41591-018-0336-8.

73. Persson, L., Borén, J., Robertson, A.K.L., Wallenius, V., Hansson, G.K., and Pekna, M. (2004). Lack of complement factor C3, but not factor B, increases hyperlipidemia and atherosclerosis in apolipoprotein E-/- low-density lipoprotein receptor-/- mice. Arterioscler. Thromb. Vasc. Biol. *24*, 1062–1067. https://doi.org/10.1161/01.ATV.0000127302.24266.40.

74. Yan, B., Freiwald, T., Chauss, D., Wang, L., West, E., Bibby, J., Olson, M., Kordasti, S., Portilla, D., Laurence, A., et al. (2020). SARS-CoV2 drives JAK1/2-dependent local and systemic complement hyper-activation. Res. Sq. 1–22. https://doi.org/10.21203/rs.3.rs-33390/v1.

75. Kolev, M., Friec, G. Le, and Kemper, C. (2014). Complement-tapping into new sites and effector systems. Nat. Rev. Immunol. *14*, 811–820. https://doi.org/10.1038/nri3761.

76. Leffler, J., Herbert, A.P., Norström, E., Schmidt, C.Q., Barlow, P.N., Blom, A.M., and Martin, M. (2010). Annexin-II, DNA, and histones serve as factor H ligands on the surface of apoptotic cells. J. Biol. Chem. *285*, 3766–3776. https://doi.org/10.1074/jbc.M109.045427.

77. Martin, M., Leffler, J., Smolag, K.I., Mytych, J., Björk, A., Chaves, L.D., Alexander, J.J., Quigg, R.J., and Blom, A.M. (2016). Factor H uptake regulates intracellular C3 activation during apoptosis and decreases the inflammatory potential of nucleosomes. Cell Death Differ. *23*, 903–911. https://doi.org/10.1038/cdd.2015.164.

78. Niyonzima, N., Rahman, J., Kunz, N., West, E.E., Freiwald, T., Desai, J.V., Merle, N.S., Gidon, A., Sporsheim, B., Lionakis, M.S., et al. (2021). Mitochondrial C5aR1 activity in macrophages controls IL-1β production underlying sterile inflammation. Sci. Immunol. *6*, eabf2489. https://doi.org/10.1126/sciimmunol.abf2489.

79. Zimmer, S., Grebe, A., Bakke, S.S., Bode, N., Halvorsen, B., Ulas, T., Skjelland, M., De Nardo, D., Labzin, L.I., Kerksiek, A., et al. (2016). Cyclodextrin promotes atherosclerosis regression via macrophage reprogramming. Sci. Transl. Med. *8*, 333ra50. https://doi.org/10.1126/scitranslmed.aad6100.

80. Ridker, P.M., Everett, B.M., Thuren, T., MacFadyen, J.G., Chang, W.H., Ballantyne, C., Fonseca, F., Nicolau, J., Koenig, W., Anker, S.D., et al. (2017). Antiinflammatory therapy with canakinumab for atherosclerotic disease. N. Engl. J. Med. *377*, 1119–1131. https://doi.org/10.1056/NEJMoa1707914.

81. Korsunsky, I., Millard, N., Fan, J., Slowikowski, K., Zhang, F., Wei, K., Baglaenko, Y., Brenner, M., Loh, P.-R., and Raychaudhuri, S. (2019). Fast, sensitive and accurate integration of single-cell data with Harmony. Nat. Methods *16*, 1289–1296. https://doi.org/10.1038/s41592-019-0619-0.

82. Binder, C.J., Hörkkö, S., Dewan, A., Chang, M.-K., Kieu, E.P., Goodyear, C.S., Shaw, P.X., Palinski, W., Witztum, J.L., and Silverman, G.J. (2003). Pneumococcal vaccination decreases atherosclerotic lesion formation: molecular mimicry between Streptococcus pneumoniae and oxidized LDL. Nat. Med. *9*, 736–743. https://doi.org/10.1038/nm876.

83. Wang, Y., Subramanian, M., Yurdagul, A., Barbosa-Lorenzi, V.C., Cai, B., de Juan-Sanz, J., Ryan, T.A., Nomura, M., Maxfield, F.R., and Tabas, I. (2017). Mitochondrial fission promotes the continued clearance of apoptotic cells by macrophages. Cell *171*, 331–345.e22. https://doi.org/10.1016/j.cell.2017.08.041.

84. Busch, C.J.-L., Hendrikx, T., Weismann, D., Jäckel, S., Walenbergh, S.M.A., Rendeiro, A.F., Weißer, J., Puhm, F., Hladik, A., Göderle, L., et al. (2017). Malondialdehyde epitopes are sterile mediators of hepatic inflammation in hypercholesterolemic mice. Hepatology *65*, 1181–1195. https://doi.org/10.1002/hep.28970.

85. Alic, L., Papac-Milicevic, N., Czamara, D., Rudnick, R.B., Ozsvar-Kozma, M., Hartmann, A., Gurbisz, M., Hoermann, G., Haslinger-Hutter, S., Zipfel, P.F., et al. (2020). A genome-wide association study identifies key modulators of complement factor H binding to malondialdehyde-epitopes. Proc. Natl. Acad. Sci. USA *117*, 9942–9951. https://doi.org/10.1073/pnas.1913970117.

Please cite this article in press as: Kiss et al., Cell-autonomous regulation of complement C3 by factor H limits macrophage efferocytosis and exacerbates atherosclerosis, Immunity (2023), https://doi.org/10.1016/j.immuni.2023.06.026

STAR★METHODS

KEY RESOURCES TABLE

REAGENT or RESOURCE	SOURCE	IDENTIFIER
Antibodies		
Anti-mouse MAC3 (clone M3/84)	BD Biosciences	Ref#: 550292; RRID: AB_393587
Anti-mouse ATG5	Novus Biologicals	Ref#: NBP2-54702
Biotinylated goat-anti-rat IgG (H+L)	VectorLabs	Ref#: BA-9401-.5
HRP-conjugated goat anti-mouse C3	MP BioMedicals	Ref#: 0855557
Donkey anti-rabbit IgG (H+L) AlexaFluor 647	Thermo Fisher Scientific	Ref#: A-31573; RRID: AB_2536183
Anti-mouse MAC1/CD11b (Clone M1/70)	R&D Systems	Ref#: MLDP5; RRID: AB_2129382
Anti-mouse CD16/32 (clone 90)	Thermo Fisher Scientific	Ref#: 14-0161-85; RRID: AB_467134
Anti-mouse CD11b APC (clone M1/70)	Thermo Fisher Scientific	Ref#: 17-0112-82; RRID: AB_469343
Anti-mouse Ly6C FITC (clone HK1.4)	BioLegend	Ref#: 128006; RRID: AB_1186135
Anti-mouse Ly6G PE (clone 1A8)	BioLegend	Ref#: 127608; RRID: AB_1186099
Anti-mouse F4/80 PerCP-Cy5.5 (clone BM8)	BioLegend	Ref#: 123128; RRID: AB_893484
Anti-mouse CD45R (B220) PerCP-Cy5.5 (clone RA3-6B2)	Thermo Fisher Scientific	Ref#: 45-0452-82; RRID: AB_1107006
Anti-mouse CD43 PE (clone S7)	BD Biosciences	Ref#: 553271; RRID: AB_394748
Anti-mouse CD23 FITC (clone B3B4)	BD Biosciences	Ref#: 11-0232-82; RRID: AB_1467923
Biotinylated anti-mouse CD21/35 (clone 7E9)	BioLegend	Ref#: 123406; RRID: AB_940401
Anti-mouse CD3e PE (clone 145-2C11)	Thermo Fisher Scientific	Ref#: 12-0031-82; RRID: AB_465496
Anti-mouse CD8a APC (clone 53-6.7)	Thermo Fisher Scientific	Ref#: 17-0081-82; RRID: AB_1283728
Anti-mouse C5aR1 PE-Cy7 (clone 20/70)	BioLegend	Ref#: 135809; RRID: AB_10900077
Anti-mouse C5aR2 AlexaFluor 700 (clone 468705)	R&D Systems	Ref#: IC4729N
Anti-mouse C3aR (clone 14D4)	Hycult Biotech	Ref#: HM1123
Anti-mouse C3/C3b/iC3b/C3c (clone 3/26)	Hycult Biotech	Ref#: HM1078; RRID: AB_533251
Anti-mouse C3a (clone mAb 3/11)	Hycult Biotech	Ref#: HM1072; RRID: AB_10130227
Anti-mouse CD16/32 APC (clone 93)	Thermo Fisher Scientific	Ref#: 17-0161-82; RRID: AB_469356
Anti-mouse TIM4 PE (clone 54, RM14-54)	Thermo Fisher Scientific	Ref#: 12-5866-80; RRID: AB_1257164
Anti-mouse VSIG4 PE-Cy7 (clone NLA14)	Thermo Fisher Scientific	Ref#: 25-5752-80; RRID: AB_2637430
Anti-mouse MHCII AlexaFluor 700 (clone M5/114.15.2)	Thermo Fisher Scientific	Ref#: 56-5231-82; RRID: AB_494010

(*Continued on next page*)

Please cite this article in press as: Kiss et al., Cell-autonomous regulation of complement C3 by factor H limits macrophage efferocytosis and exacerbates atherosclerosis, Immunity (2023), https://doi.org/10.1016/j.immuni.2023.06.026

Continued

REAGENT or RESOURCE	SOURCE	IDENTIFIER
FITC-labelled hematopoietic lineage cocktail	Thermo Fisher Scientific	Ref#: 22-7770-72; RRID: AB_2644066
Anti-mouse C-kit (CD117) APC-eFluor780 (clone 2B8)	Thermo Fisher Scientific	Ref#: 47-1171-80; RRID: AB_1272213
Anti-mouse Sca1 (Ly6A/E) PE-Cy7 (clone J43)	Thermo Fisher Scientific	Ref#: 25-5981-81; RRID: AB_469668
Anti-mouse CD34 eFluor 450 (clone RAM34)	Thermo Fisher Scientific	Ref#: 48-0341-80; RRID: AB_2043838
Anti-mouse CD135 (Flt3) PerCP-eFlour 710 (clone A2F10)	Thermo Fisher Scientific	Ref#: 46-1351-80; RRID: AB_10733392
Anti-mouse IL7R (CD127) PE (clone A7R34)	Thermo Fisher Scientific	Ref#: 12-1271-82; RRID: AB_465844
Anti-human CFH (clone OX-24)	Cedarlane Laboratories	Ref#: AM20110PU-N; RRID: AB_10547520
Anti-mouse IgG1 kappa APC (clone P3.6.2.8.1)	Thermo Fisher Scientific	Ref#: 17-4714-82; RRID: AB_763649
Monoclonal anti-mouse CFH	R&D Systems	Ref#: MAB4999; RRID: AB_10890774
Polyclonal anti-mouse CFH	R&D Systems	Ref#: AF4999; RRID: AB_10972783
Anti-human C3 FITC	MP BioMedicals	Ref#: 0855500
Anti-mouse LC3	GeneTex	Ref#: GTX127375; RRID: AB_11176277
Chemicals, peptides, and recombinant proteins		
Thioglycollate	Thermo Fisher Scientific	Ref#: CM0173B
Zymosan	Sigma Aldrich	Ref#: Z4250
Bafilomycin A1	Eubio	Ref#: BV1-0252-C100
4',6-Diamidino-2-Phenylindole (DAPI)	Sigma Aldrich	Ref#: D1306
Cell Tracker Green CMFDA	Thermo Fisher Scientific	Ref#: C7025
Citrate buffer ph6.0, 10x	Sigma Aldrich	Ref#: C9999
Recombinant mouse CFH	R&D Systems	Ref#: 4999-FH
pHrodo Red, succinimidyl ester	Invitrogen	Ref#: P36600
Purified mouse complement C3	Complement Technology Inc	Ref#: M113
Critical commercial assays		
In Situ Cell Death Detection Kit TMR-Red	Roche Diagnostics	Ref#: 12156792910
Alexa Fluor 488 Antibody Labeling Kit	Thermo Fisher Scientific	Ref#: A20181
Foxp3/ Transcription Factor Staining Buffer set	Thermo Fisher Scientific	Ref#: 00-5523-00
Annexin V and 7-AAD viability solution kit	BioLegend	Ref#: 640934
Mouse C3 ELISA kit	Abcam	Ref#: ab263884
Mouse C5 ELISA kit	Abcam	Ref#: ab264609
Mouse C3a ELISA kit	MyBioSource	Ref#: MBS2701721
Pierce BCA Protein Assay Kit	Thermo Fisher Scientific	Ref#: 23225
IL-1 beta Mouse Uncoated ELISA Kit	Thermo Fisher Scientific	Ref#: 88-7013-88
High Capacity cDNA Reverse Transcription Kit	Thermo Fisher Scientific	Ref#: 4368814
Kapa SYBR Fast Bio-Rad iCycler with ROX dye	Roche Diagnostics	Ref#: KK4602
RNeasy mini kit	Qiagen	Ref#:74004
TruSeq Stranded mRNA LT sample preparation kit	Illumina	https://www.illumina.com

(*Continued on next page*)

Continued

REAGENT or RESOURCE	SOURCE	IDENTIFIER
Takara's SMART-Seq v4 Ultra Low Input RNA Kit	Takara	Ref#:634894
Deposited data		
scRNA-seq and bulk RNA-seq datasets	This paper	N/A
Experimental models: Cell lines		
THP-1 human monocytic cell line	ATCC	TIB-202
RAW 264.7 murine macrophage cell line	ATCC	TIB-71
Experimental models: Organisms/strains		
Mouse: C57BL/6J	Jackson Laboratory	Strain code: 000664
Mouse: C57BL/6J *Cfh-/-*	In-house	Pickering et al.[33]
Mouse: B6.12957-Ldlrtm1Her/J	Jackson Laboratory	Strain code: 002207
Mouse: B6.12954-C3tm1Crr/J	Jackson Laboratory	Strain code: 029661
Mouse: C57BL/6J *Cfh-/-C3-/-*	In-house	N/A
Mouse: C57BL/6J *Cfh-/-Ldlr-/-*	In-house	N/A
Mouse: C57BL/6J *C3-/-Ldlr-/-*	In-house	N/A
Mouse: C57BL/6J *Cfh-/-C3-/-Ldlr-/-*	In-house	N/A
Mouse: C57BL/6Tg(UBC-GFP)30Scha/J	Jackson Laboratory	Strain code: 004353
Mouse:C57BL/6J *Cfh-/-*UBC-GFP	In-house	N/A
Mouse: B6.SJL-Ptprca Pepcb/BoyJ	Jackson Laboratory	Strain code: 002014
Oligonucleotides		
Primers Table S2		N/A
Software and algorithms		
FlowJo (version 10)	BD Biosciences	https://www.flowjo.com
GraphPad Prism (version 8.0)	Dotmatics	https://www.graphpad.com
CellRanger (v2.1.0.)	10x Genomics	https://10xgenomics.com/
Seurat (v3)	10x Genomics	https://satijalab.org/seurat
Harmony	Broad Institute	Korsunsky et al.[81]
AxioVision	Carl Zeiss AG	https://www.zeiss.com
Adobe Photoshop CS5	Adobe Inc.	https://www.adobe.com
Star 2.5.0a	Gensoft Pasteur	https://gensoft.pasteur.fr
Image Lab 4.1	Bio-Rad Laboratories	https://www.bio-rad.com
Loupe Cell Browser 3.1.1	10x Genomics	https://www.10xgenomics.com
ACT-1 v2.63	Nikon	https://www.nikon.com
RTA software	Illumina	https://www.illumina.com
TopHat2 v2.1.1	CCB at Johns Hopkins	https://ccb.jhu.edu
Tuxedo Suite	Illumina	https://www.illumina.com
Bowtie2	Langmead and Salzberg[8]	http://bowtie-bio.sourceforge.net/bowtie2/index.shtml
ACT-1 v2.63	Nikon	https://www.nikon.com
Image J	NIH	https://imagej.nih.gov
R (version 4.0)	The R Foundation	https://www.r-project.org
Other		
Rodent chow	LASvendi	https://www.lasvendi.com
Western-type diet	Ssniff Spezialdiäten	https://www.ssniff.com

RESOURCE AVAILABILITY

Lead contact

Further information and requests for resources should be directed to and will be fulfilled by the lead contact, Christoph J. Binder (christoph.binder@meduniwien.ac.at).

Materials availability

This study did not generate new, unique reagents.

Data and code availability

- Single-cell RNA-seq and bulk RNA-seq data have been deposited at GEO and the accession number can be provided upon request.
- This paper does not report original code.
- Any additional information required to reanalyze the data reported in this paper is available from the lead contact upon request.

EXPERIMENTAL MODEL AND SUBJECT DETAILS

Mice

All experimental studies were approved by the Animal Ethics Committee of the Medical University of Vienna, Austria and were performed according to the guidelines for Good Scientific Practice of the Medical University of Vienna, Austria. All mice were on a C57BL/6J background. $Cfh^{-/-}$ mice were generated by Matthew C. Pickering.[33] $C3^{-/-}$ and $Ldlr^{-/-}$ mice as well as Ubiquitin (UBI or UBC)-GFP transgenic mice were purchased originally from The Jackson Laboratories (Bar Harbor, ME, USA). $Cfh^{-/-}$, $C3^{-/-}$ and $Ldlr^{-/-}$ mice were further crossed to generate $Cfh^{-/-}$ $C3^{-/-}$, $Cfh^{-/-}$ $Ldlr^{-/-}$, $C3^{-/-}$ $Ldlr^{-/-}$ and $Cfh^{-/-}$ $C3^{-/-}$ $Ldlr^{-/-}$ mice. $Cfh^{-/-}$ UBI-GFP mice were also generated in-house. CD45.1 mice were a generous gift from Robert Kralovics (Department of Laboratory Medicine, Medical University of Vienna, Vienna, Austria).

Bone marrow transplantation studies were performed. as follows: 8-week-old $Ldlr^{-/-}$ mice or 10-week-old $Cfh^{-/-}$ mice were lethally irradiated (2x 6Gy) and were subsequently injected intravenously via the retro-orbital plexus with $3x10^6$ $Cfh^{+/+}$ or $Cfh^{-/-}$ bone marrow from 6-week-old donors. The recipient mice were given a 5-week recovery period before intervention studies. Successful bone marrow reconstitution was verified by extracting and amplyfing genomic DNA from the bone marrow of the recipient mice.

The mixed bone marrow chimera experiment was performed, as follows: 8-week-old $Ldlr^{-/-}$ mice were lethally irradiated (2x6Gy) and were subsequently injected intravenously via the retro-orbital plexus with $5x10^6$ bone marrow cells, which consisted of a 1:1 mixture of $Cfh^{+/+}$ (CD45.1) and $Cfh^{-/-}$ UBI-GFP (CD45.2) cells from 6-week-old donors. The recipient mice were given a 6-week recovery period before the intervention study.

For inducing sterile peritonitis, mice were intraperitoneally injected with a single dose of 50μl/g/body weight sterile thioglycolate (Thermo Fisher Scientific, Difco Laboratories, Waltham, MA, USA) or zymosan (Sigma Aldrich, St. Louis, MO, USA) in sterile PBS, and were sacrificed 24 hours, 72 hours or 168 hours post injection. In experiments involving bafilomycin A1 (BafA1; Eubio, Vienna, Austria) treatment, thioglycolate-injected mice received two doses of BafA1 (1mg/kg) or 0.9% NaCl, 6 and 30 hours post sterile peritonitis induction. This dosage was equivalent to approaches used in previous reports.[56,57]

All mice were bred in our in-house breeding facility. All experiments were performed with age- and sex-matched adult littermates (i.e. 8 weeks of age or older).

METHOD DETAILS

Diets

Unless indicated otherwise, all mice received non-atherogenic rodent chow (LASvendi, Soest, Germany). For dietary intervention studies, experimental mice were fed a Western type diet containing 21% milk fat and 0.2% cholesterol (E15721-347, Ssniff Spezialdiäten GmbH, Soest, Germany) for 10-12 weeks.

Evaluation of atherosclerosis

The extent of atherosclerosis was assessed as previously described.[82] Briefly, lesion formation in the entire aorta was evaluated in *en face* preparations by staining the luminal surface with Sudan IV (Sigma Aldrich). Atherosclerosis in the aortic origin was quantified in modified elastin-trichrome stained, 5 μm-thick serial sections through a 400 μm segment of the aortic root starting upon the appearance of all 3 valve leaflets. For each mouse, 9 sections separated by 50 μm were examined and total lesion volume was determined. Necrotic core formation was quantified as the percent of acellular area compared to total lesional area. Each section was photographed using the AxioVision software (Carl Zeiss AG, Jena, Germany) and lesion size was assessed in a blinded fashion by computer-assisted image analysis using Adobe Photoshop CS5 (Adobe Inc., San Jose, CA, USA) and ImageJ software (National Institute of Health).

Immunohistochemistry in aortic root lesions

For the quantification of lesional macrophage content or ATG5 expression, sections of aortic root lesions were stained with an anti–mouse MAC-3 antibody (clone M3/84, BD Pharmingen, San Diego, CA, USA) or with a polyclonal anti-mouse ATG5 antibody (Novus Biologicals, Centennial, CO, USA), respectively. Sections were then stained with a biotinylated goat anti-rat IgG (VectorLabs, Burlingame, CA, USA) and were developed with streptavidin-peroxidase polymer (Sigma Aldrich). For the measurement of intact lesional C3 content, sections of aortic root lesions were stained with and HRP-conjugated goat anti-mouse complement C3 antibody (MP BioMedicals, Santa Ana, CA, USA). Quantification was performed with computer-assisted image analysis using Adobe Photoshop CS5 (Adobe Inc.) and ImageJ software.

Quantification of lesional apoptosis and *in situ* efferocytosis assay

Sections of aortic root lesions were de-paraffinized with xylene (Carl Roth, Karlsruhe, Germany) and were rehydrated in decreasing concentrations of ethanol (Carl Roth). The specimens were then boiled in 1x citrate buffer (Sigma Aldrich; pH 6.0) for antigen retrieval. After cooling, the sections were incubated with TUNEL using the In Situ Cell Death Detection Kit TMR-Red (Roche Diagnostics, Rotkreuz, Switzerland) according to the manufacturer's instructions at 37°C for 60 min in a dark, humidified atmosphere and then washed 3 times with 1X DPBS (Sigma Aldrich). Sections were then blocked with 10% donkey serum (Sigma Aldrich) in 1X DPBS supplemented with 1% bovine serum albumin (BSA; PAN-Biotech GmbH, Aldenbach, Germany) for 60 min and were incubated overnight at 4°C with a rabbit anti-mouse F4/80 antibody (clone: D2S9R, Cell Signaling Technology, Cambridge, UK; 1:200). Following 3 washing steps with 1X DPBS, sections were incubated with a polyclonal donkey anti-rabbit IgG (H+L) antibody conjugated to Alexa Fluor 647 (Jackson ImmunoResearch, West Grove, PA, USA; 1:500) for 2 hours and after intensive washing with 1X DPBS, were counterstained with 4',6-diamidino-2-phenylindole (DAPI, Sigma Aldrich; 1:2000) for 5 min. Slides were mounted in Fluoromount (Thermo Fisher Scientific). Representative fields (six to eight fields of each valve leaflet in a 200 μm depth) were photographed with Axio Imager A1 (Carl Zeiss AG). For the quantification of apoptotic macrophages, only $TUNEL^+F4/80^+$ cells that co-localized with DAPI-stained nuclei were counted as being positive. *In situ* efferocytosis was quantified as described by Wang et al.[83] Shortly, the ratio of $TUNEL^+$ nuclei that were associated with $F4/80^+$ macrophages ('macrophage-associated' apoptotic cells), indicative of efferocytosis, or not associated with $F4/80^+$ macrophages ('free' apoptotic cells) was determined.

Liver Histology

The left lobe of each liver was isolated and four equal pieces were snap frozen in liquid nitrogen for further analyses. To assess the level of macrophage infiltration, 7 μm-thick frozen liver sections were stained with an anti-Mac1 antibody (clone M1/70; R&D Systems, Minneapolis, MN, USA; 1:500) as described previously.[84] Cell nuclei were counterstained with hematoxylin (VWR, Klinipath, Radnor, PA, USA). Pictures were taken with a Nikon digital camera DMX1200 (Nikon, Tokyo, Japan) and ACT-1 v2.63 software. To determine the extent of liver inflammation, the number of $Mac1^+$ cells was counted in a blinded fashion using six images (200X) per each liver.

Primary cell isolation, flourescence-activated cell sorting and flow cytometry

Spleens were mechanically dissociated through a 100 μm cell strainer (BD Biosciences, Franklin Lakes, NJ, USA) and red blood cells were lysed in red blood cell lysis buffer (Morphisto, Frankfurt am Main, Germany). Peripheral blood was collected via the vena cava (in a MiniCollect EDTA blood collection TUBE; Greiner Bio-One, Kremsmünster, Austria) and red blood cells were lysed in red blood cell lysis buffer. Peritoneal exudate cells were harvested by peritoneal lavage using ice-cold HBSS (Thermo Fisher Scientific) supplemented with 2% fetal calf serum (FCS; Thermo Fisher Scientific, Gibco). Total viable cells were counted manually using a hemocytometer or by CASY cell counter & analyzer (OLS-OMNI Life Science GmbH, Bremen, Germany). For flourescence-activated cell sorting, the whole cell suspension was incubated with 2.5 μg/ml of a blocking anti-CD16/32 antibody (Clone 90, Thermo Fisher Scientific, eBioscience) diluted in 1X DPBS (Sigma Aldrich) supplemented with 1% FCS for 20 min at 4°C. After two washing steps, cells were stained with the following monoclonal antibodies: anti-CD11b APC (clone M1/70, Thermo Fisher Scientific, eBioscience), anti-Ly6C FITC (clone HK1.4, BioLegend, San Diego, CA, USA), anti-Ly6G PE (clone 1A8, BioLegend), anti-F4/80 PerCP-Cy5.5 (clone BM8, BioLegend), anti-CD45R (B220) PerCP-Cy5.5 (clone RA3-6B2, Thermo Fisher Scientific, eBioscience), anti-CD43 PE (clone S7, BD Biosciences), anti-CD23 FITC (clone B3B4, BD Biosciences), biotinylated anti-CD21/35 (clone 7E9, BioLegend), anti-CD3e PE (clone 145-2C11, Thermo Fisher Scientific, eBioscience), anti-CD4 FITC (clone GK1.5, Thermo Fisher Scientific, eBioscience), anti-CD8a APC (clone 53-6.7; Thermo Fisher Scientific, eBioscience) and streptavidin APC (Thermo Fisher Scientific, eBioscience). Data were acquired on a SH800S Cell Sorter (Sony Biotechnology, San Jose, CA, USA) and were analyzed using FlowJo software 10 (Tree Star, Ashland, OR, USA).

For flow cytometry, $1x10^6$ cells were added in a 96-well V-bottom plate (Thermo Fisher Scientific) and incubated with 2.5 μg/ml of a blocking anti-CD16/32 antibody (Clone 90, Thermo Fisher Scientific, eBioscience) diluted in 1X DPBS supplemented with 1% FCS for 20 min at 4°C. After two washing steps, cells were stained with the following monoclonal antibodies: anti-CD11b APC (clone M1/70, Thermo Fisher Scientific, eBioscience), anti-Ly6C FITC (clone HK1.4, BioLegend), anti-Ly6G PE (clone 1A8, BioLegend), anti-F4/80 PerCP-Cy5.5 (clone BM8, BioLegend), anti-C5aR1 (CD88) PE-Cy7 (clone 20/70, BioLegend), anti-C5aR2 (C5L2) Alexa Fluor 700 (clone 468705, R&D Systems, Minneapolis, MN, USA), anti-C3aR Alexa Fluor 488 (14D4, Hycult Biotech, Wayne, PA, USA), anti-C3/C3b/iC3b,/C3c Alexa Fluor 488 (clone 3/26, Hycult), anti-C3a Alexa Fluor 488 (clone mAb 3/11, Hycult), anti-CD16/32 APC (clone 93, Thermo Fisher Scientific, eBioscience), anti-TIM4 PE (clone 54 (RM14-54), Thermo Fisher Scientific, eBioscience) anti-MHCII

Alexa Fluor 700 (clone M5/114.15.2, Thermo Fisher Scientific, eBioscience), anti-VSIG4 PE-Cy7 (clone NLA14, Thermo Fisher Scientific, eBioscience), FITC-labelled hematopoietic lineage cocktail (Thermo Fisher Scientific, eBioscience), anti-c-kit (CD117) APC-eFluor 780 (clone 2B8, Thermo Fisher Scientific, eBioscience), anti-Sca1 (Ly6A/E) PE-Cy7 (clone J43, Thermo Fisher Scientific, eBioscience), anti-CD34 eFluor 450 (clone RAM34, Thermo Fisher Scientific, eBioscience), anti-CD135 (Flt3) PerCP-eFluor 710 (clone A2F10, Thermo Fisher Scientific, eBioscience) and anti-IL7R (CD127) PE (clone A7R34, Thermo Fisher Scientific, eBioscience). All unconjugated antibodies were labelled using the Alexa Fluor 488 Antibody Labeling Kit (Thermo Fisher Scientific, Invitrogen).

To determine the amount of intracellular C3, C3a, C3aR, C5aR1 and C5aR2, cells were first incubated with the unconjugated form of the respective antibody and were fixed and permeabilized with Fixation and Permeabilization Solution (Thermo Fisher Scientific, eBioscience) for 20 minutes at 4 °C and then stained intracellularly in permeabilization buffer (Thermo Fisher Scientific, eBioscience) with the respective conjugated antibodies stated above. For intracellular human CFH staining, THP-1 macrophages were fixed and permeabilized as stated above and then stained intracellularly in permeabilization buffer (Thermo Fisher Scientific, eBioscience) with anti-CFH (clone OX-24, Cedarlane Laboratories, Burlington, ON, Canada) followed by a secondary antibody staining using anti-IgG1 kappa APC (clone P3.6.2.8.1, Thermo Fisher Scientific, eBioscience). All stainings were carried out in 1X DPBS supplemented with 1% FCS for 30 min at 4°C, followed by two washing steps. Finally, to identify early and late dead cells staining with Annexin V and 7-AAD viability solution was performed according to the manufacturer's protocol (Thermo Fisher Scientific, eBioscience). Data were acquired on a BD FACSCalibur (BD Biosciences) or BD LSRII Fortessa (BD Biosciences) and were analyzed using FlowJo software 10 (Tree Star).

Sorting of aortic macrophages and RNA sequencing

Ldlr$^{-/-}$ male mice (n=9) were subjected to 3 weeks of atherogenic diet. Aortic macrophages (n= 3 separate samples, each sample consisting of aortic macrophages pooled from 3 mice) were subjected to RNA-seq. Single cell suspensions of aortic cells were prepared and aortic macrophages were identified as CD45^{+}CD11b^{+}CD64^{+} gated on live singlets. RNA extraction and residual DNA removal upon DNase digestion was performed with the RNeasy mini kit (Qiagen) according to the manufacturer's instructions. Total RNA, after quality check with Agilent Bioanalyser 2100 system, was made into sequencing libraries using Takara's SMART-Seq v4 Ultra Low Input RNA Kit, following manufacturer's instruction, at the Genomics/Transcriptomics Core (IMS-MRL, Cambridge, UK). Briefly, total RNA was fragmented before reverse transcription. Second strand cDNA was PCR synthesized with the incorporation of SMART technology. cDNA originally from rRNA was removed selectively before Illumina-compatible barcoded libraries are generated via PCR amplification. Indexed libraries were normalized, pooled and were sequenced on the Illumina HiSeq 4000 platform, single-end reads (SE50) at the Genomics Core Facility, Cancer Research UK Cambridge Institute (Cambridge, UK). Sequence reads were mapped to the mouse genome (GRCm38) and gene-level count was performed using Star 2.5.0a using standard parameters.

Meta-analysis of single cell-RNA sequencing data from atherosclerotic mouse aorta

We used the results from a meta-analysis of integrating different scRNA-Seq datasets from mouse aortas in our recent review.[59] scRNA-Seq data from 9 data sets were analyzed using the latest bioinformatics integration method Harmony.[81] Harmony allows to integrate multiple experimental and biological batches across data from different laboratories in which cells were assigned and corrected for dataset specificity using fuzzy clustering. After quality control preprocessing, a total of 15,288 cells were projected and were visualized into a shared embedding space in which cells were assigned and corrected for dataset specificity using fuzzy clustering. Then, all cells were visualized using the nonlinear high dimensionality deduction method, Uniform Manifold Approximation and Projection. Louvain-based graph clustering was then used with the Seurat method together with downstream cell-type merging and annotation that yielded 17 clusters as we published in Zernecke et al.[59]

Plasma cholesterol and triglyceride quantification

Blood was collected from the vena cava (in a MiniCollect EDTA blood collection TUBE; Greiner Bio-One) at the time of sacrifice. Blood was centrifuged at 1000g for 30 minutes at room temperature. Plasma total cholesterol and triglyceride were measured in an ISO 15189 accredited medical laboratory under standardized conditions on Beckman Coulter AU5400 (Beckman Coulter, Brea, CA, USA) instruments, using the Beckman Coulter OSR6516 reagent.

Quantification of complement component levels

To measure plasma concentrations of complement components, peripheral blood was collected from the vena cava (in a MiniCollect EDTA blood collection TUBE; Greiner Bio-One) at the time of sacrifice. Blood was centrifuged at 1000g for 30 minutes at room temperature and plasma samples were snap frozen in liquid nitrogen for further use. To determine the intracellular levels of complement components in monocyte-derived macrophages (Mo-Macs), peritoneal exudate cells were harvested from thioglycolate-injected wildtype and Cfh$^{-/-}$ mice by peritoneal lavage using ice-cold HBSS (Thermo Fisher Scientific, Gibco) supplemented with 2% FCS. Total viable cells were counted by CASY cell counter & analyzer (OLS-OMNI Life Science GmbH) and cells were plated in equivalent numbers in RPMI-1640 medium (Thermo Fisher Scientific, Invitrogen) containing 10% FCS at 37°C for 60 minutes. Non-adherent cells were removed by washing three times with ice-cold 1X DPBS (Sigma Aldrich). The purity of adherent Mo-Macs was confirmed by flow cytometry, as described above. Adherent Mo-Macs were lysed in an IP protein lysis buffer containing 50 mM Tris (Sigma Aldrich, pH 7.5), 150 mM NaCl (Carl Roth), 5 mM EDTA (Sigma Aldrich), 5 mM EGTA (Sigma Aldrich) and 1% NP-40 (Merck, Calbiochem, Darmstadt, Germany). Lysates of adherent Mo-Macs were kept at -20°C or used immediately. The concentration of complement components was determined by specific ELISA kits including the Mouse C3 ELISA kit (Abcam, Cambridge, UK), the Mouse C3a ELISA Kit

(MyBioSource, San Diego, CA, USA) and the Mouse C5 ELISA kit (Abcam, Cambridge, UK), according to the manufacturer's recommendations. To quantify plasma CFH levels, a self-established sandwich ELISA was set up using a monoclonal and a polyclonal anti-mouse CFH antibody (both R&D systems). As a measure of C3 consumption, C3a/C3 ratio was calculated based on total C3a concentrations divided by the total C3 levels of each individual sample. For intracellular measurements, total protein content of the lysates was quantified using Pearce BCA Protein Assay Kit (Thermo Fisher Scientific) and was used to normalize complement component levels.

Quantification of secreted interleukin-1 beta and peritoneal CXCL1 levels

Mo-Macs were isolated and plates as stated above. Adherent Mo-Macs were cultured in RPMI-1640 medium (Thermo Fisher Scientific, Invitrogen) containing 10% fetal calf serum (FCS; Thermo Fisher Scientific, Gibco) at 37°C for 24 hours and the supernatant were collected and spun down at 400g for 5 minutes. The concentrations of interleukin-1 beta in cell supernatants were quantified by the IL-1 beta Mouse Uncoated ELISA Kit (Thermo Fisher Scientific, Life Technologies) according to the manufacturer's instructions. Samples were developed using TMB substrate solution (BD Biosciences) and the reaction was terminated with 1M H_2SO_4 (Honeywell, Morristown, NJ, USA). The absorbance was measured with a Synergy 2 plate reader (BioTek Instruments, Winooski, VT, USA) at 450 nm as the primary wavelength.

Peritoneal lavage fluid was analyzed for CXCL1 secretion by an enzyme-linked immunosorbent assay using corresponding capture and detection antibodies and recombinant protein standards (CXCL1: MAB453, BAF453, 453-KC-010; R&D Systems), followed by Streptavidin-HRP (DY998, R&D Systems) and TMB Substrate incubation (555214, Becton, Dickinson and Company). Absorbance was measured using a Synergy 2 Multi-Mode Reader (Biotek).

Antibody measurements

Anti-dsDNA IgG antibodies were quantified as previously described.[36] In short, 96-well Nunc MaxiSorp plates (Thermo Fisher Scientific) were irradiated with UV light and coated with calf thymus DNA (Thermo Fisher Scientific, Invitrogen; 5 μg/ml) in 1X DPBS (Sigma Aldrich). After overnight incubation at 4°C, plates were blocked in 1% bovine serum albumin (BSA; PAN-Biotech GmbH) in 1X DPBS. Plasma samples were added in 1:200 dilutions and the signal was detected with HRP-conjugated anti-mouse IgG (1:1000, GE Healthcare, Chicago, IL, USA). The absorbance was measured with a Synergy 2 plate reader (BioTek Instruments) at 450 nm as the primary wavelength.

Cell lines

Human THP-1 monocytic cells and murine RAW 264.7 macrophages (Abelson leukemia virus-transformed cell line derived from BALB/c mice) were purchased from ATCC (Manassas, VA, USA) and were maintained in presence of RPMI-1640 (Thermo Fisher Scientific, Invitrogen) supplemented with 10% heat-inactivated FCS and 1% Penicillin Streptomycin Glutamine (Thermo Fisher Scientific, Gibco). All cells were incubated in a humidity-controlled environment at 37°C, 5% CO_2 (Thermo Scientific Heraeus Cytoperm 2).

Generation and stimulation of THP-1-derived macrophages

To obtain THP-1-derived macrophages, THP-1 monocytes were stimulated for 24 hours with 100 nM phorbol-12-myristate-13-acetate (PMA; Sigma Aldrich). After 2 days, THP-1 macrophages were stimulated in culture medium containing 100 ng/ml recombinant human interferon-gamma (BioLegend). Secreted CFH levels were quantified as previously described.[85] Intracellular levels of CFH and C3 were measured by flow cytometry on a BD FACSCalibur (BD Biosciences) and were analyzed using FlowJo software 10 (Tree Star). A monoclonal mouse anti-CFH antibody (OX-24; Cedarlane, Burlington, Ontario, Canada) as well as a FITC-conjugated goat anti-human C3 antibody (MP Biomedicals) were used as detection antibodies.

Generation of CMFDA-labeled apoptotic RAW 264.7 macrophages

RAW 264.7 macrophages were plated on a cell culture dish (100x20 mm, CELLSTAR, Greiner Bio-One) and were incubated in RPMI-1640 medium (Thermo Fisher Scientific, Invitrogen) containing 5 μM CellTracker Green chloromethylfluorescein diacetate (CMFDA; Thermo Fisher Scientific, Invitrogen) in the absence of serum for 30 min at 37°C. After replacing the medium with 1X DPBS (Sigma Aldrich), apoptosis of RAW 264.7 macrophages was induced by UVC irradiation (100mJ/cm^2) using a UVP CX-2000 UV Crosslinker (Analytik Jena, Jena, Germany). Following the irradiation, cells were maintained in RPMI-1640 medium containing sterile bovine serum albumin (BSA; PAN-Biotech GmbH; 50μg/ml) in a humidity-controlled environment at 37°C, 5% CO2 for 16 hours.

Ex vivo efferocytosis assays

Peritoneal exudate cells were harvested as stated above. Non-adherent cells were removed by two times washing with fresh medium. Adherent monocyte-derived macrophages (Mo-Macs) were cultured in RPMI-1640 medium (Thermo Fisher Scientific, Invitrogen) in the presence of 1% of respective sera at 37°C overnight and were subsequently incubated with CMFDA-labeled apoptotic RAW macrophages in a 1:3 ratio for 1.5 hours. After discarding the supernatant, cells were washed three times in ice-cold 1x DPBS (Sigma Aldrich) and were detached using a cell scraper (Sigma Aldrich). Mo-Macs were then taken in collection tubes and the percentages of CMFDA$^+$ efferocytotic cells were quantified on a BD FACSCalibur (BD Biosciences) and were analyzed using FlowJo software 10 (Tree Star). In an alternative approach, adherent CFH-deficient Mo-Macs were cultured in RPMI-1640 medium (Thermo Fisher Scientific, Invitrogen) in the presence of 1% of respective sera at 37°C overnight. Prior to apoptotic cell feeding, Mo-Macs were pre-incubated with 200 nM BafA1 (1:500 dilution, 0.1mg/ml) for 2 hours. Concomitantly, UVC irradiated apoptotic macrophages were

Please cite this article in press as: Kiss et al., Cell-autonomous regulation of complement C3 by factor H limits macrophage efferocytosis and exacerbates atherosclerosis, Immunity (2023), https://doi.org/10.1016/j.immuni.2023.06.026

stained with pHrodo (Invitrogen) diluted in 1:1000 for 30 minutes on 37°C and subsequently washed in 1x DPBS. Afterwards, pHrodo-labeled apoptotic macrophages were added to the culture in a 1:3 ratio for 1.5 hours. Mo-Macs were then taken in collection tubes and the percentages as well as mean fluorescence intensity of pHrodo$^+$ efferocytotic cells were quantified as stated above.

C3 supplementation studies

Peritoneal exudate cells were harvested as stated above. Non-adherent cells were removed by two times washing with fresh medium. Adherent monocyte-derived macrophages (Mo-Macs) were cultured in RPMI-1640 medium (Thermo Fisher Scientific, Invitrogen) and supplemented with increasing concentration of purified mouse complement C3 (Complement Technology Inc., Tyler, TX, USA). Consumption of added C3 was confirmed with quantifying cell-associated C3a levels using the Mouse C3a ELISA Kit (MyBioSource, San Diego, CA, USA).

LC3 conversion assay

Protein loading was normalized in each lysate of adherent monocyte-derived macrophages using a Pearce BCA Protein Assay Kit (Thermo Fisher Scientific, Gibco). After resuspending the lysates in 1x Laemmli buffer (Bio-Rad Laboratories, Hercules, CA, USA) and heating the samples up to 96°C, proteins were separated on a polyacrylamide gel (Bio-Rad Laboratories), transferred to PVDF membranes (Bio-Rad Laboratories), blocked with 5% non-fat dry milk (Bio-Rad Laboratories) in 1x TBS (Sigma Aldrich, St. Louis, MO, USA) containing 1% bovine serum albumin (BSA; PAN-Biotech GmbH, Aldenbach, Germany) and incubated with a goat anti-mouse LC3 antibody (GeneTex, Irvine, CA, USA; 1:1000). As secondary antibody, rabbit anti-goat IgG-HRP (Bio-Rad Laboratories) was used and the subsequent chemiluminescent quantification was performed on ChemiDoc imager (Bio-Rad Laboratories). The signal was measured with Image Lab 4.1 analysis software (Bio-Rad Laboratories).

Generation and stimulation of bone-marrow-derived macrophages

To obtain bone-marrow derived macrophages (BMDM), bone marrow cell suspensions were isolated by flushing femurs and tibiae of C57BL/6J mice through a 26-gauge needle (BD Biosciences) with 1% fetal calf serum (FCS; Thermo Fisher Scientific, Gibco) in 1x DPBS (Sigma Aldrich) and red blood cells were lysed as stated above. BMDMs were then cultured in the presence of RPMI-1640 (Thermo Fisher Scientific, Invitrogen), 10% heat-inactivated FCS, penicillin (100 U/ml), streptomycin (100 μg/ml) and antimycotics (all Sigma Aldrich), supplemented with 10% L929-conditioned medium. After 7-8 days, BMDMs were stimulated in culture medium containing 100 ng/ml recombinant mouse interferon-gamma (R&D Systems).

Gene expression analyses

Total RNA was isolated from tissue, cell culture or sorted cell subsets using the RNeasy Mini Kit (VWR, PeqLab) and total RNA was reversely transcribed using the High Capacity cDNA Reverse Transcription kit (Thermo Fisher Scientific, Applied Biosystems). Quantitative real-time PCR was performed using Kapa SYBR Fast Bio-Rad iCycler with ROX dye (Roche Diagnostics, Kapa Biosystems) in a CFX96 Real-time System (Bio-Rad Laboratories). All data were normalized to the housekeeping gene Cyclin B1 (CycB1) and/or 36B4. Values are expressed as the relative expression compared to untreated samples or the control group/cell type.

Primer sequences

mm CycB1-forward: 5'-CAGCAAGTTCCATCGTGTCATCA-3'
mm CycB1-reverse: 5'-GGAAGCGCTCACCATAGATGCTC-3'
mm 36B4-forward: 5'-AGGGCGACCTGGAAGTCC-3'
mm 36B4-reverse: 5'-CCCACAATGAAGCATTTTGGA-3'
mm Cfh-forward: 5'-ACCACATGTGCCAAATGCTA-3'
mm Cfh-reverse: 5'-TGTTGAGTCTCGGCACTTTG-3'
mm C4bp-forward: 5'-CCTGGCTATGGTAGGGGAAT-3'
mm C4bp-reverse: 5'-CCTCGGACCTCACAAGAACT-3'
mm Cr1l-forward: 5'-ACTCAACCTGGACGAGTGCT-3'
mm Cr1l-reverse: 5'-CTGGGGGTATCTCACAAGGA-3'
mm Cd55b-forward: 5'-TCAACATACCAACCGGCATA-3'
mm Cd55b-reverse: 5'-TTGGTGGGTCTGGACAAAAT-3'
mm Cd55-forward: 5'-TAATGCGAGGGGAAAGTGAC-3'
mm Cd55-reverse: 5'-TGAGGGGGTTCCTGTACTTG-3'
mm Cfi-forward: 5'-TGTGTGAATGGGAAGCACAT-3'
mm Cfi-reverse: 5'-CACAACGGCTCTCATCTTCA-3'
mm Cfd-forward: 5'-TGCACAGCTCCGTGTACTTC-3'
mm Cfd-reverse: 5'-CACCTGCACAGAGTCGTCAT-3'
mm Fhr-b-forward: 5'-GTACAGAGAATGGCTGGTC-3'
mm Fhr-b-reverse: 5'-AGTGATCCTCTTGCTTTCTG-3'
mm Cxcl1-forward: 5'-TGCACCCAAACCGAAGTCAT-3'
mm Cxcl1-reverse: 5'-TTGTCAGAAGCCAGCGTTCAC-3'
mm Cxcl2-forward: 5'-AGTGAACTGCGCTGTCAATGC-3'

mm Cxcl2-reverse: 5'-AGGCAAACTTTTTGACCGCC-3'
mm Tnfa-forward: 5'-CATCTTCTCAAAATTCGAGTGACAA-3'
mm Tnfa-reverse: 5'-TGGGAGTAGACAAGGTACAACCC-3'
mm C3-forward: 5'-AGAAAGGGATCTGTGTGGCA-3'
mm C3-reverse: 5'- GAAGTAGCGATTCTTGGCGG-3'
mm C5-forward: 5'- TCTGAGAGTGCTTGGACAGG-3'
mm C5-reverse: 5'- TGGTGGGGCATATGTCAACT-3'
mm Cfp-forward: 5'- AAGCCATGTGCTGGAAAACT-3'
mm Cfp-reverse: 5'- TCTCACCCTGACCTTCAACC-3'
mm Cfb-forward: 5'- CCCAGGAGAACAGCAGAAGA-3'
mm Cfb-reverse: 5'- ACTCGCCACCTTCTCAATCA-3'
mm Marco-forward: 5'- CCAAGGAAAACCTACTGATC-3'
mm Marco-reverse: 5'- TTCTGCCTACAAGACCTGGG-3'
mm Timd4-forward: 5'- ATCCACTTCACAGCTGACGA-3'
mm Timd4-reverse: 5'- GTCTGGCCTCTTGTGTCTCT-3'
mm *Tgfb1*-forward: 5'- TGATACGCCTGAGTGGCTGTCT-3'
mm *Tgfb1*-reverse: 5'- CACAAGAGCAGTGAGCGCTGAA-3'
mm *Il10*-forward: 5'- GCCAGAGCCACATGCTCCTA-3'
mm *Il10*-reverse: 5'- GTCCAGCTGGTCCTTTGTTTG-3'

Single-cell RNA sequencing

Droplet-based single-cell RNA sequencing was performed using the Chromium Single Cell 3' v3 Chemistry (10X Genomics, Pleasanton, CA, USA) according to manufacturer's recommendations. Raw reads were demultiplexed using cellranger (version 2.1.0) mkfastq. Demultiplexed reads were aligned to the mouse genome provided by 10x Genomics (mm10 genome version 1.2.0) using cellranger count. Data were analyzed and visualized using Loupe Cell Browser 3.1.1.

Bulk RNA-sequencing

NGS Library Preparation

Total RNA concentration was quantified by using the Qubit 2.0 Fluorometric Quantitation System (Life Technologies, Carlsbad, CA, USA). The RNA integrity number (RIN) was determined by applying the Experion Automated Electrophoresis System (Bio-Rad, Hercules, CA, USA). RNA-seq libraries were prepared by using the TruSeq Stranded mRNA LT sample preparation kit (Illumina, San Diego, CA, USA) and the Sciclone and Zephyr liquid handling workstations (PerkinElmer, Waltham, MA, USA) for pre-PCR and post-PCR procedures, respectively. Library concentrations were measured with the Qubit 2.0 Fluorometric Quantitation System (Life Technologies, Carlsbad, CA, USA) and the size distribution was evaluated by using the Experion Automated Electrophoresis System (Bio-Rad, Hercules, CA, USA). For the sequencing step, samples were diluted and pooled into Next-Generation Sequencing (NGS) libraries in equimolar amounts.

Sequencing and Raw Data Processing

Expression profiling libraries were sequenced by HiSeq 3000/4000 instruments (Illumina, San Diego, CA, USA) using the 50-base-pair single-end configuration. The base calls were provided by the RTA software (Illumina, San Diego, CA, USA) and were subsequently converted into multiplexed, unaligned BAM format followed by demultiplexing into sample-specific, unaligned BAM files. For the raw data processing of the instruments, Picard-tool based custom programs were used.

Transcriptome Analysis

[Tuxedo Suite]. Transcriptome analysis was carried out with the Tuxedo suite. For each individual sample, NGS reads tested by vendor quality filtering were aligned to the UCSC Genome Browser [mm10] flavor of the Genome Reference Consortium [GRCm38] assembly with TopHat2 (v2.1.1), a splice junction mapper using the Bowtie2 (v2.2.9) short read aligner. Therefore, "basic" Ensembl transcript annotation (version e87; December 2016) served as reference transcriptome. Based on spliced read alignments and the reference transcriptome joint with raw transcript quantification, Cufflinks (v2.2.1) allowed for transcriptome assembly. Ahead of differential expression calling with Cuffdiff (included in Cufflinks v2.2.1), transcriptome sets of each individual sample of each group was combined via the Cuffmerge algorithm. Lastly, the cummeRbund and biomaRt Bioconductor packages were used in custom R scripts for performing quality assessment and further refinement of the results from the analysis.

[STAR Aligner and DESeq2]. NGS reads were mapped onto the Genome Reference Consortium [GRCm38] assembly together with the "Spliced Transcripts Alignment to a Reference" (STAR) aligner using the "basic" Ensembl transcript annotation (version e87; December 2016) serving as the reference transcriptome. As the [mm10] assembly flavor of the UCSC Genome Browser was favored for alignment as well as for downstream data processing with Bioconductor packages, Ensembl transcript annotation needed to be adjusted to UCSC Genome Browser sequence region names ahead of the alignment. Reads overlapping transcript features were determined by using the summarizeOverlaps() function of the Bioconductor GenomicAlignments package also taking into consideration that the Illumina TruSeq stranded mRNA protocol results in sequencing of the second strand, therefore all reads required inverting before counting. The Bioconductor DESeq2 package was then applied to model the data set and identify differentially expressed genes.

Human single-cell RNA sequencing analysis

We reanalyzed scRNA-seq data of cells from atherosclerotic coronary arteries of 4 donors as published in Wirka et al. Nat Med 2019. The author-provided count matrix (Gene Expression Omnibus GSE131778) was loaded and analyzed in Seurat v3 (Stuart, 2019). Batch correction across patients was performed using Harmony.[81] We first performed Louvain clustering, dimensional reduction (UMAP), and differential gene expression analysis on total coronary artery cells to identify major vascular cell lineages. Cells corresponding to mononuclear phagocytes (monocytes, macrophages, dendritic cells) were extracted and separately reanalyzed with Louvain clustering and UMAP dimensional reduction. Differential gene expression analysis across clusters was performed using the built-in 'FindAllMarkers' Seurat function. Data visualizations were generated using the built-in Seurat functions 'DotPlot' and 'FeaturePlot'.

Statistical analysis

Statistical analyses were performed using Graph Pad Prism 8 for Windows (Graph Pad Software, La Jolia, CA, USA). Normal distribution of data was assessed, and experimental groups were compared using two tailed Student's unpaired or paired t test or Mann-Whitney U test or one-way ANOVA followed by Tukey's multiple comparison test, as appropriate. Data points that were more than 2x standard deviation of the mean were excluded as statistical outliers. Data are presented as mean ± SEM and considered significant at $p \leq 0.05$ (*$p \leq 0.05$, **$p \leq 0.01$, ***$p \leq 0.001$ and ****$p \leq 0.0001$, respectively).

Immunity, Volume *56*

Supplemental information

Cell-autonomous regulation of complement C3 by factor H limits macrophage efferocytosis and exacerbates atherosclerosis

Máté G. Kiss, Nikolina Papac-Miličević, Florentina Porsch, Dimitrios Tsiantoulas, Tim Hendrikx, Minoru Takaoka, Huy Q. Dinh, Marie-Sophie Narzt, Laura Göderle, Mária Ozsvár-Kozma, Michael Schuster, Nikolaus Fortelny, Anastasiya Hladik, Sylvia Knapp, Florian Gruber, Matthew C. Pickering, Christoph Bock, Filip K. Swirski, Klaus Ley, Alma Zernecke, Clément Cochain, Claudia Kemper, Ziad Mallat, and Christoph J. Binder

Figure S1 (*Related to Figure 1*). The effect of global CFH and/or C3 deficiency on autoantibody levels, bone marrow hematopoiesis, blood monocyte levels as well as lesional macrophage and collagen content

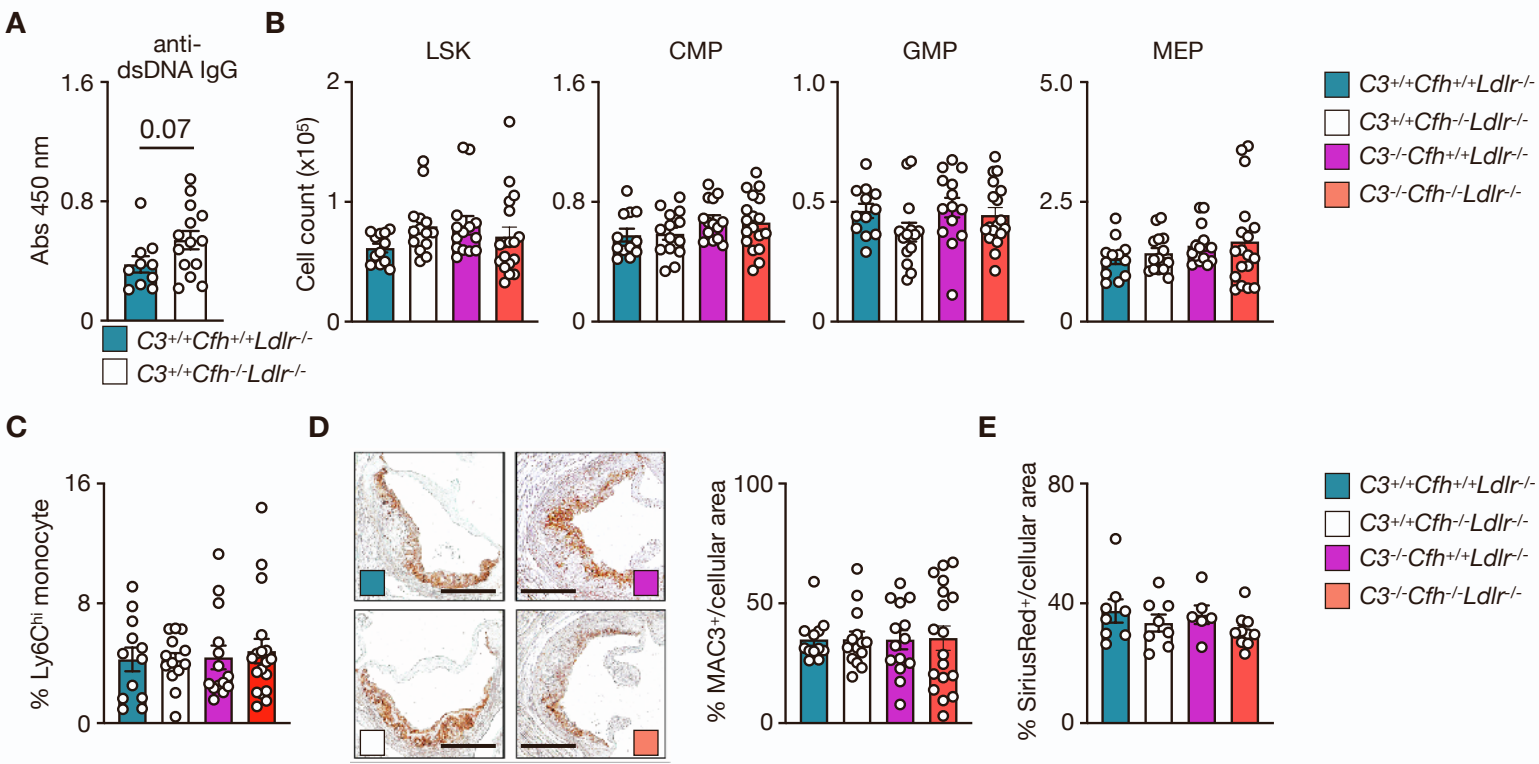

Figure S2 (*Related to Figure 2*). Accumulation of intracellular C3 in Ly6C^{hi} monocytes and monocyte-derived macrophages without downstream C5 activation

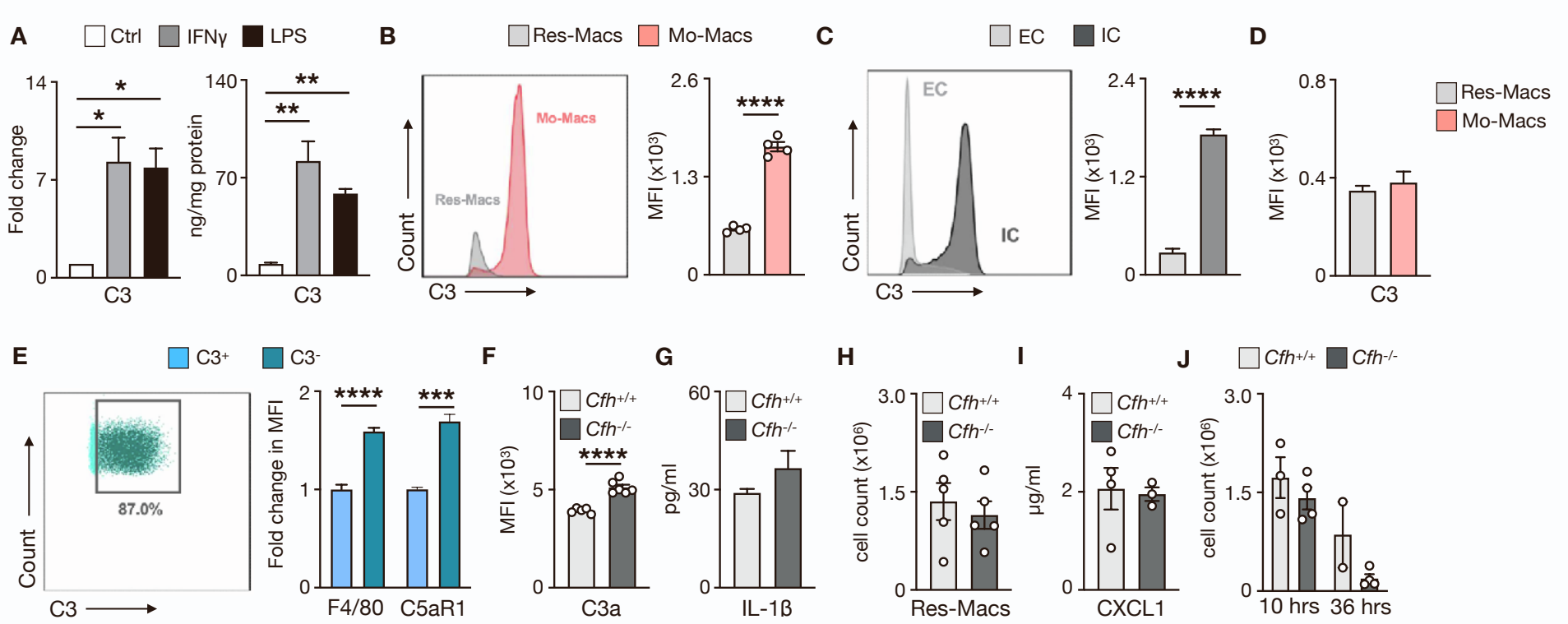

Figure S3 (*Related to Figure 3*). Purity, principal component analysis plot as well as transcriptomic and functional profile of adherent monocyte-derived macrophages isolated from the peritoneal cavity of *Cfh*$^{+/+}$ vs *Cfh*$^{-/-}$ mice

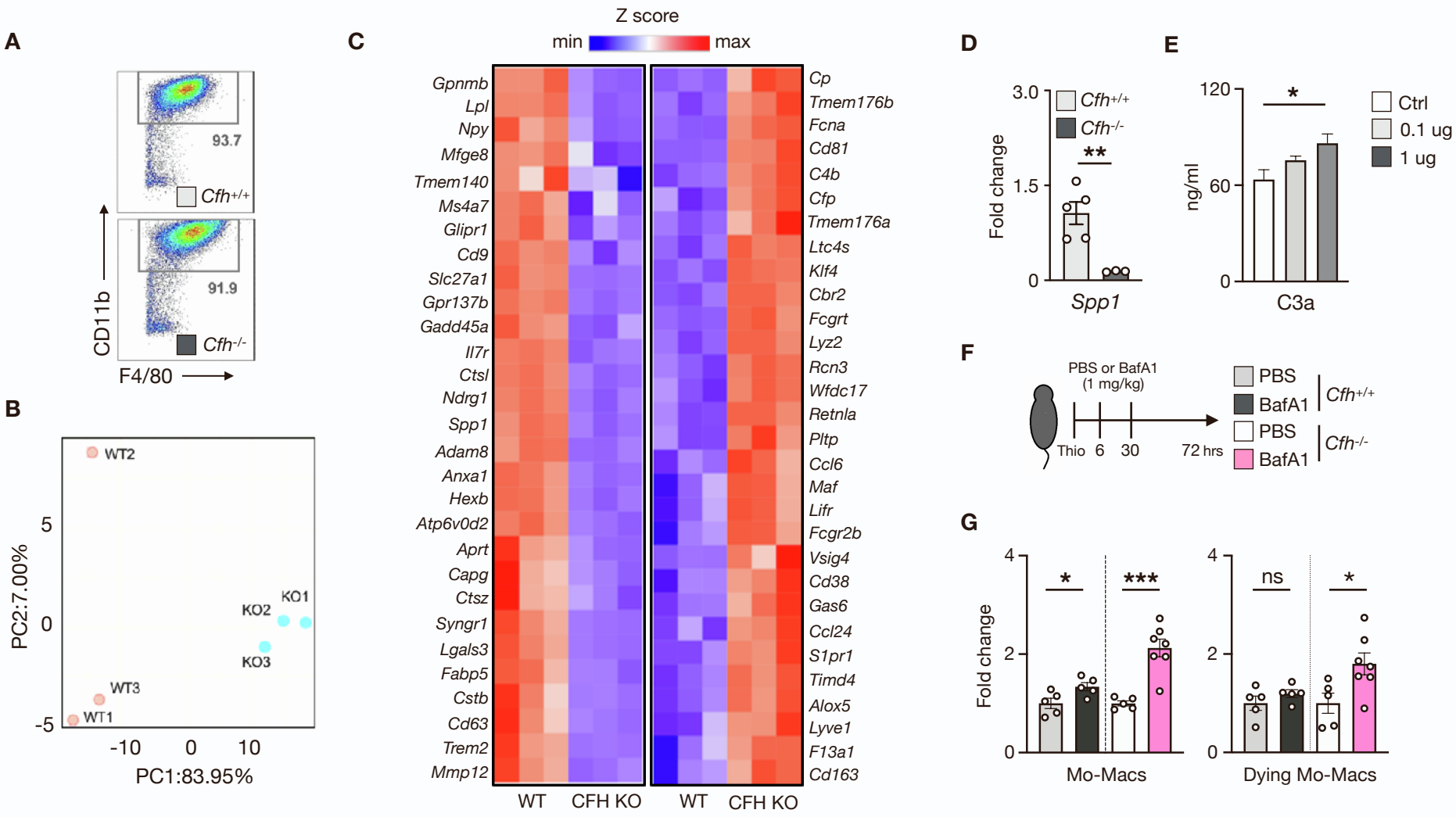

Figure S4 (*Related to Figure 4*). Expression pattern of complement activators as well as regulators among immune cells and the effect of monocyte-derived CFH deficiency on monocyte-derived macrophage phenotype during inflammation

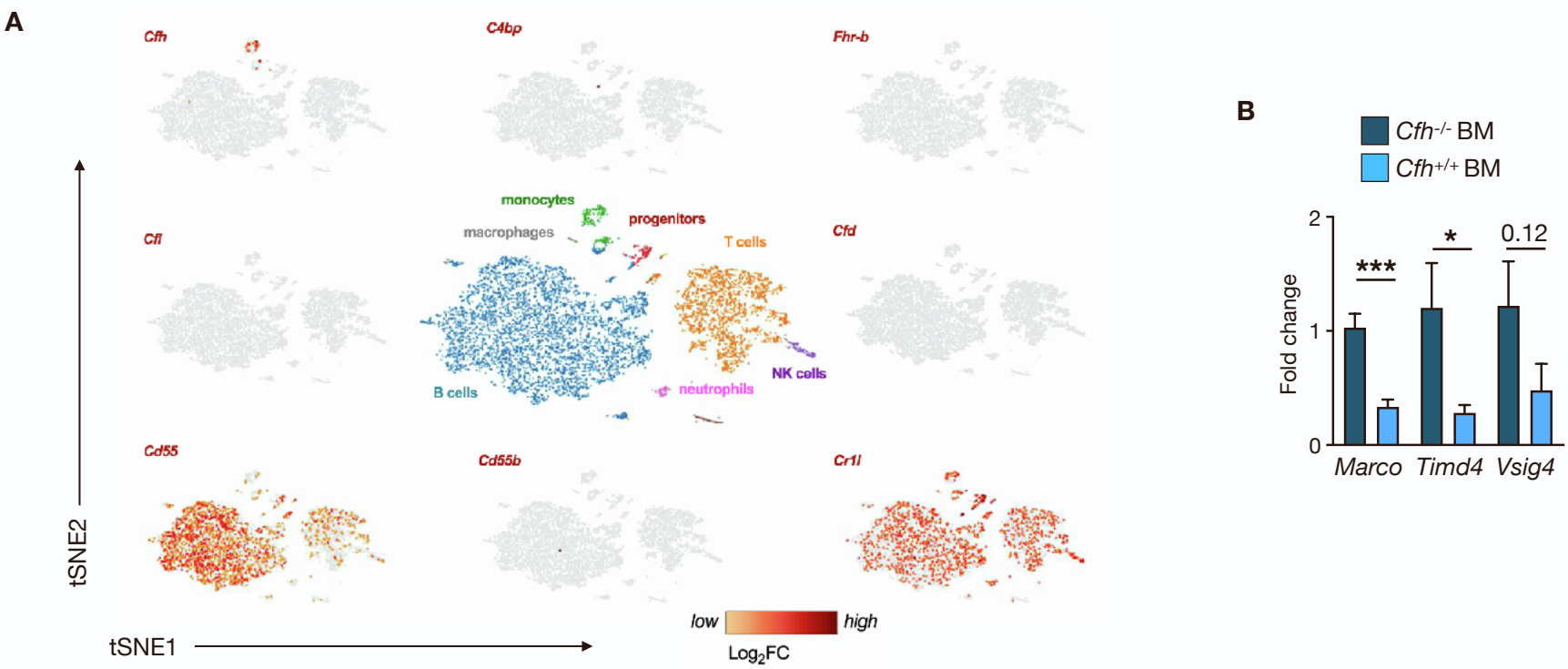

Figure S5 (*Related to Figure 5*). Ly6C^{hi} monocytes upregulate alternative complement genes upon Western diet feeding

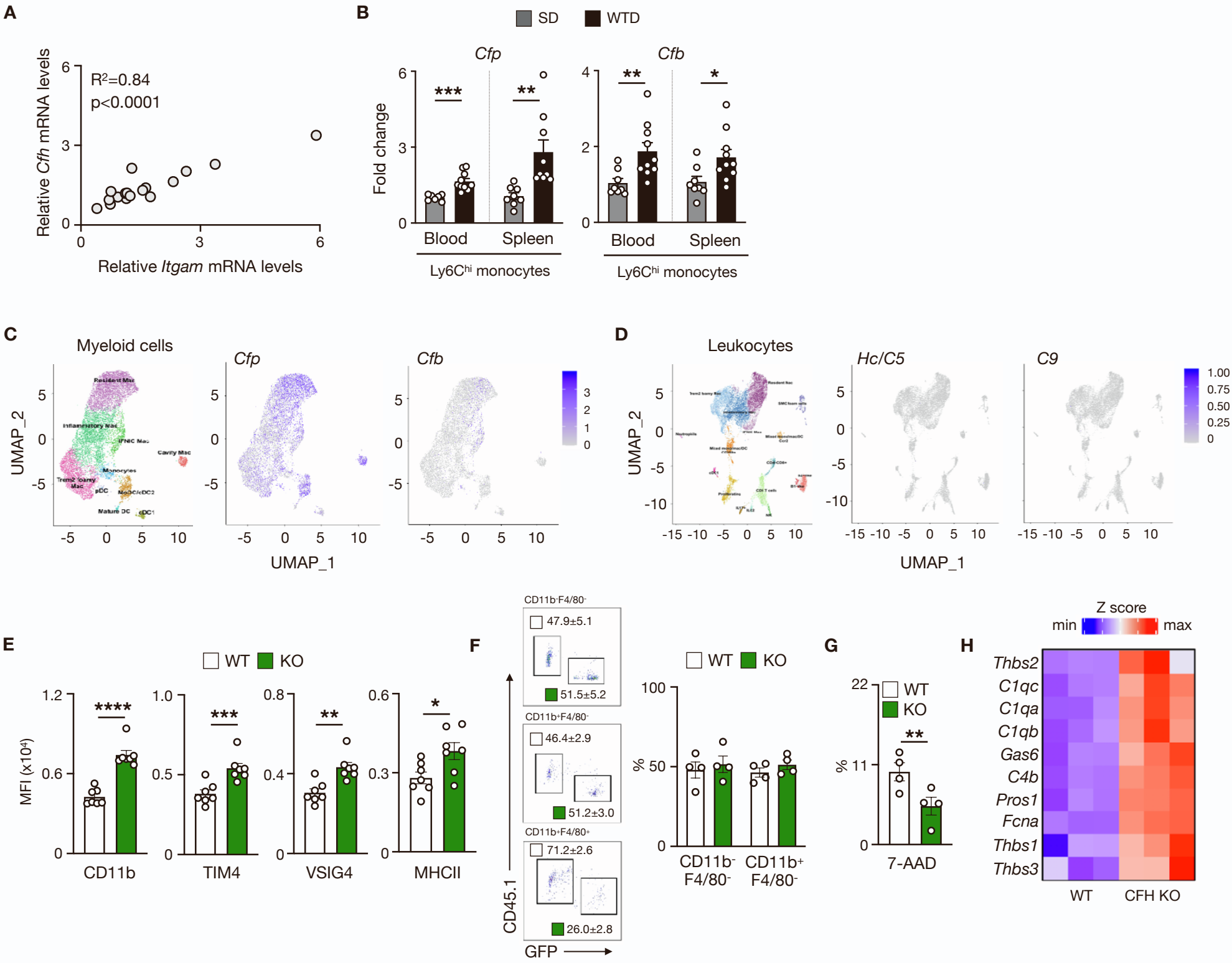

Figure S6 (Related to Figure 6). Hematopoietic deletion of complement factor H does not affect weight gain or lipid metabolism but mitigates atherosclerosis and hepatic inflammation

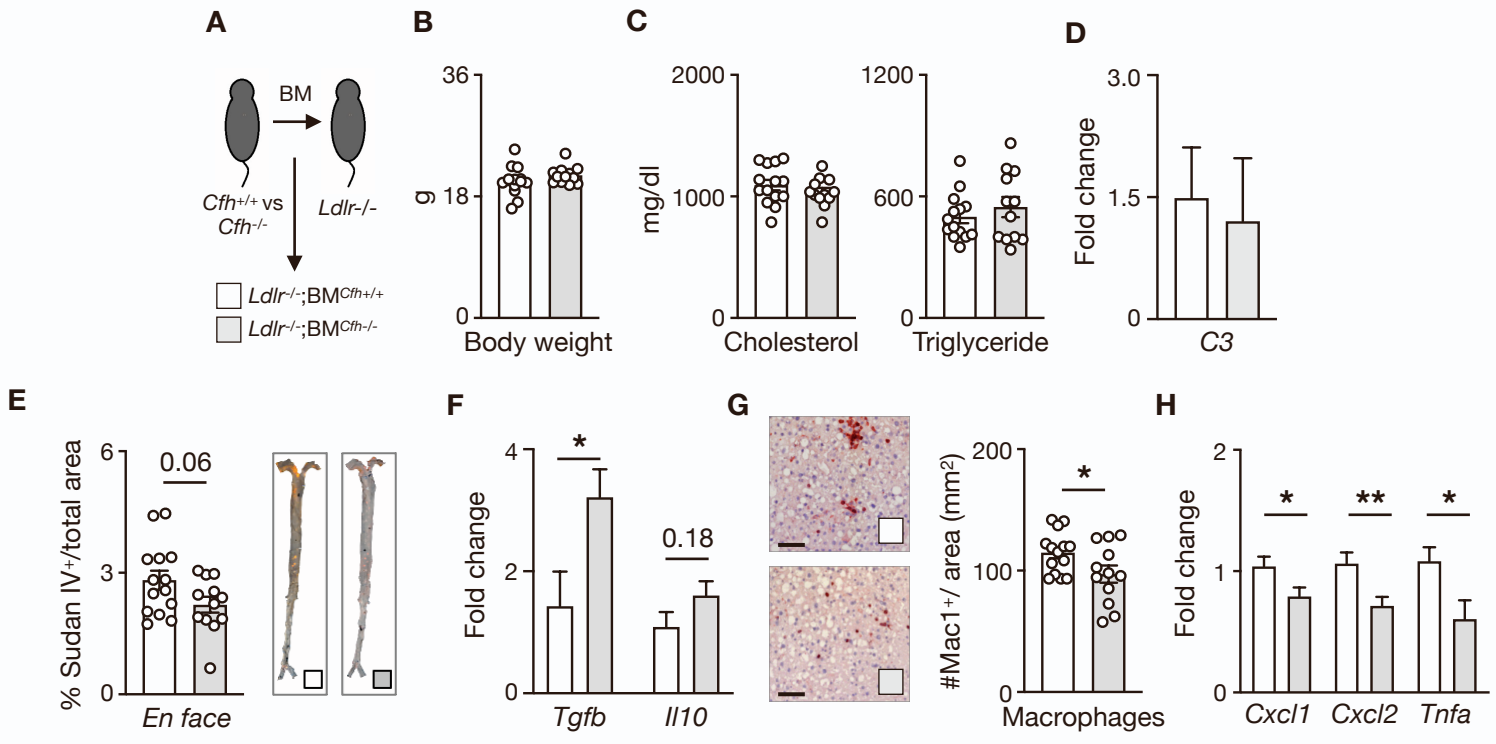

Figure S7 (Related to Figure 7). Complement C3- and CFH-producing inflammatory aortic macrophages from human coronary arteries express *VSIG4*, but not *C5*

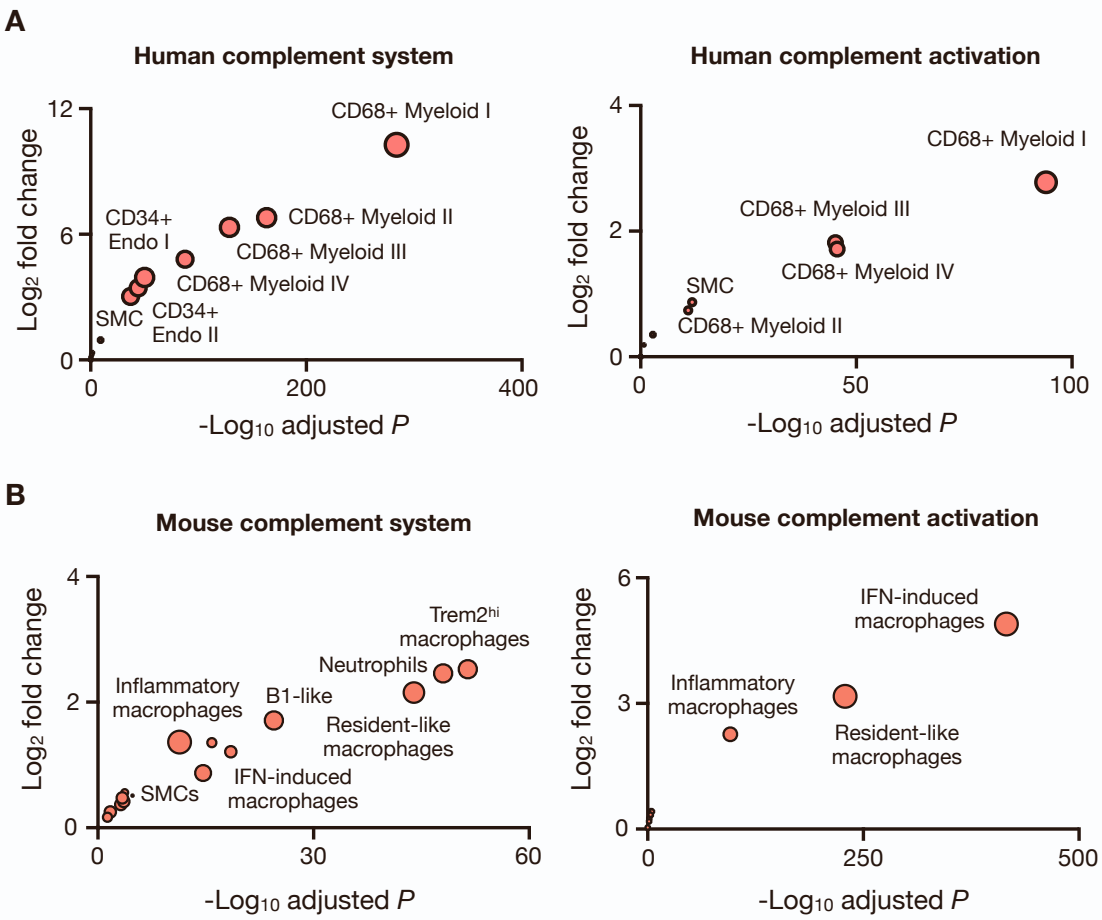

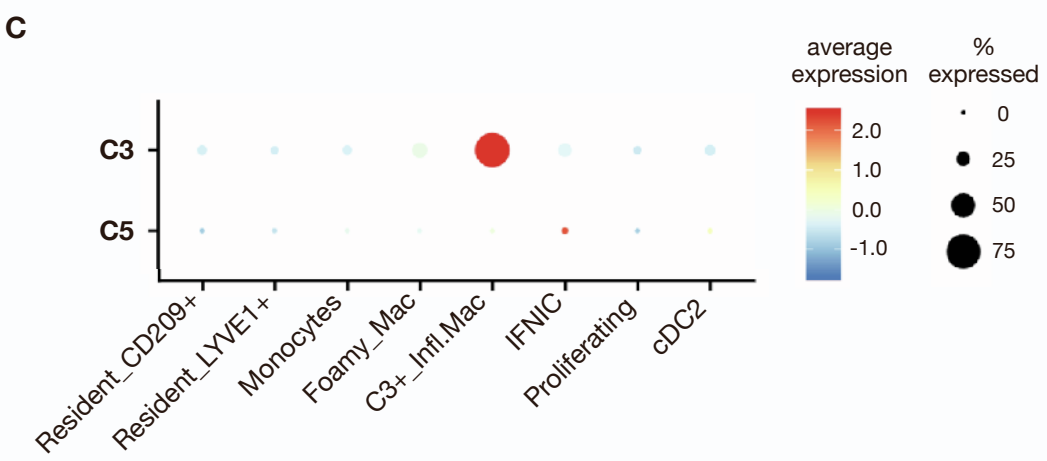

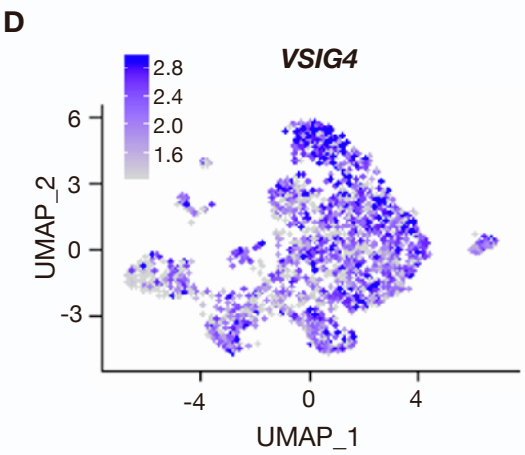

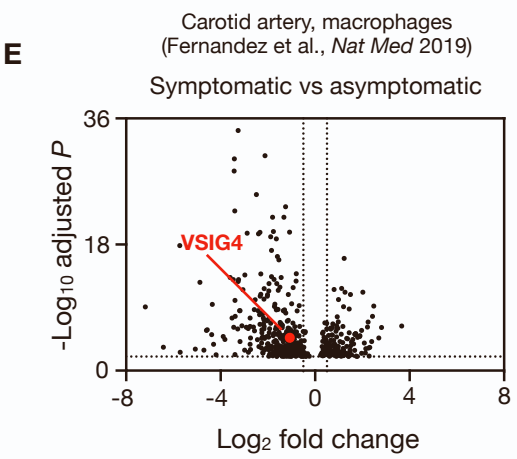

Figure legends to supplementary figures:

Figure S1 (*Related to Figure 1*). The effect of global CFH and/or C3 deficiency on autoantibody levels, bone marrow hematopoiesis, blood monocyte levels as well as iesional macrophage and collagen content (A-E) *C3*$^{+/+}$*Cfh*$^{+/+}$*Ldlr*$^{-/-}$, *C3*$^{+/+}$*Cfh*$^{-/-}$ *Ldlr*$^{-/-}$, *C3*$^{-/-}$*Cfh*$^{+/+}$*Ldlr*$^{-/-}$ and *C3*$^{-/-}$*Cfh*$^{-/-}$*Ldlr*$^{-/-}$ mice were fed an atherogenic diet for 10 weeks (n=12, 14, 14 and 18, respectively; pool of two independent experiments. **(A)** Plasma IgG titers specific for double stranded-DNA measured by ELISA of *C3*$^{+/+}$*Cfh*$^{+/+}$*Ldlr*$^{-/-}$ and *C3*$^{+/+}$*Cfh*$^{-/-}$ *Ldlr*$^{-/-}$ mice. **(B)** Enumeration of bone marrow hematopoiesis (LSK: Lin^{-}Sca-1^{+}c-Kit^{+} hematopoietic stem cells, CMP: common myeloid progenitors, GMP: granulocyte-monocyte progenitors, MEP: megakaryocyte-erythroid progenitors) and **(C)** Ly6C^{hi} monocytes in the blood by flow cytometry. Quantification of **(D)** MAC-3^{+} lesional macrophage and **(E)** Sirius-Red^{+} collagen content per total cellular area by immunohistochemistry. Statistical significance was evaluated by one-way ANOVA followed by Tukey's multiple comparison test. Error bars indicate SEM.

Figure S2 (*Related to Figure 2*). Accumulation of intracellular C3 in Ly6C^{hi} monocytes and monocyte-derived macrophages without downstream C5 activation (A) qRT-PCR analysis of *C3* transcript levels and ELISA measurement of intracellular C3 levels of bone marrow-derived macrophages of wild-type mice cultured with or without interferon-gamma (IFNγ) or LPS for 24 hours. **(B)** C3 levels of resident macrophages (Res-Macs) vs monocyte-derived macrophages (Mo-Macs) in the peritoneal lavage fluid of control vs thioglycolate-injected mice (24 hours) quantified by intracellular flow cytometry. **(C)** Extracellular and intracellular C3 mean fluorescence intensity (MFI) of Mo-Macs from the peritoneal cavity of thioglycolate-injected mice (24 hours) measured by flow cytometry. Representative flow cytometry histograms are shown. Bars represent the mean±SEM of 4 mice. **(D)** Surface levels of C3 on monocyte-derived macrophages vs resident macrophages in the peritoneal lavage fluid of thioglycolate-injected vs control C57BL/6J mice assessed by flow cytometry. Bars represent the mean±SEM of 4 vs 4 mice. **(E)** Representative flow cytometry plot shows the percentage of intracellular C3^{+} Ly6C^{hi} monocytes in the peritoneal lavage fluid of thioglycolate-injected mice (24 hours) assessed by flow cytometry. Mean fluorescence intensity (MFI) of macrophage markers (F4/80, C5aR1) on the surface of C3^{-} and C3^{+} Ly6C^{hi} monocytes in the peritoneal lavage fluid of thioglycolate-injected mice quantified by flow cytometry.**(F)** C3a MFI measured by intracellular flow cytometry and **(G)** IL-1β levels in the supernatant of Mo-Macs isolated from peritoneal cavity of thioglycolate-injected *Cfh*$^{+/+}$ vs *Cfh*$^{-/-}$ mice measured by ELISA. **(H)** Total F4/80^{+} macrophage numbers in the the peritoneal cavity of unchallenged *Cfh*$^{+/+}$ vs *Cfh*$^{-/-}$ mice. **(I)** CXCL1 levels in the peritoneal lavage fluid of *Cfh*$^{+/+}$ vs *Cfh*$^{-/-}$ mice 2, hours after thioglycolate injection, quantified by ELISA. **(J)** Absolute numbers of neutrophils (Cd11b^{int}Ly6C^{hi}Ly6G^{+}) in the peritoneal lavage fluid of *Cfh*$^{+/+}$ vs *Cfh*$^{-/-}$ mice 10 and 36 hours after zymosan injection, quantified by flow cytometry. Statistical significance was evaluated by two-tailed Student's *t*-tests (* $P < 0.05$, ** $P < 0.01$, *** $P <$ 0.001, **** $P < 0.0001$). Error bars indicate SEM.

Figure S3 (*Related to Figure 3*). Purity, principal component analysis plot as well as transcriptomic and functional profile of adherent monocyte-derived macrophages isolated from the peritoneal cavity of *Cfh*$^{+/+}$ vs *Cfh*$^{-/-}$ mice (**A**) Representative flow cytometry plots show the percentage of CD11b^{+}F4/80^{+} cells among adherent cells after plating total peritoneal cells isolated from thioglycolate-injected *Cfh*$^{+/+}$ and *Cfh*$^{-/-}$ mice measured by flow cytometry. (**B**) Principal component analysis (PCA) plot of RNA sequencing experiment of *Cfh*$^{+/+}$ vs *Cfh*$^{-/-}$ mice. **(C)** Heat map of genes associated with a Trem2^{hi} vs resident-like macrophage expression profile between CFH deficient vs control macrophages. **(D)** qRT-PCR analysis of *Spp1* transcript levels of Mo-Macs sorted from the peritoneal cavity of thioglycolate-injected *Cfh*$^{+/+}$ vs *Cfh*$^{-/-}$ mice. **(E)** Cell-associated C3a levels of *ex vivo* Mo-Macs isolated from the peritoneal cavity of thioglycolate-injected C57BL/6J mice following supplementation with increasing concentrations of purified mouse C3. **(F)** Schematic representation of BafA1 treatment of *Cfh*$^{+/+}$ and *Cfh*$^{-/-}$ mice. **(G)** Relative change in the numbers of Mo-Macs (Cd11b^{int}F4/80^{int}Ly6C^{dim}) as well as 7-AAD^{+} dying Mo-Macs in the peritoneal cavity of *Cfh*$^{+/+}$ and *Cfh*$^{-/-}$ mice injected with or without BafA1 after thioglycolate injection, quantified by flow cytometry. Pool of two independent experiments. Each symbol represents individual mice. Statistical significance was evaluated by two-tailed Student's *t*-tests (* $P < 0.05$, ** $P < 0.01$, **** $P < 0.0001$). Error bars indicate SEM.

Figure S4 (*Related to Figure 4*). Expression pattern of complement activators as well as regulators among immune cells and the effect of monocyte-derived CFH deficiency on monocyte-derived macrophage phenotype during inflammation (A) Single cell RNA-seq data from the spleen of a C57BL/6J mouse, represented by t-SNE. Middle panel demonstrates splenic immune cell clustering and annotation, surrounding feature plots show expression of complement genes (*Cfh, C4bp, Fhr-b, Cfi, Cfd, Cd55, Cd55b, Cr1l*) are shown around the middle panel. **(B)** Lethally irradiated wild-type mice were reconstituted with bone marrow from *Cfh*$^{+/+}$ vs *Cfh*$^{-/-}$ mice and were subjected to thioglycolate-induced sterile peritonitis, 10 weeks after transplantation (n=5 vs n=6 and n=3 vs n=6 of two independent experiment). qRT-PCR analysis of *Marco*, *Timd4* and *Vsig4* transcript levels of Mo-Macs isolated from bone marrow chimeric mice 72 hours after thioglycolate injection. Data are expressed relative to gene expression in *Cfh*$^{-/-}$ bone marrow-transplanted *Cfh*$^{-/-}$ mice. Statistical significance was evaluated by two-tailed Student's *t*-tests (*$P < 0.05$, ***$P < 0.001$). Error bars indicate SEM.

Figure S5 (*Related to Figure 5*). Ly6C^{hi} monocytes upregulate alternative complement genes upon Western diet feeding (A) qRT-PCR analysis showing that transcript levels of *Cfh* correlate with *Itgam* (encoding CD11b) expression in the liver of *Ldlr*$^{-/-}$ mice fed a standard (SD) or Western-type diet (WTD) for 12 weeks (n=8 vs n=10). **(B)** *Ldlr*$^{-/-}$ mice were fed SD or WTD for 12 weeks (n=8 vs n=10). qRT-PCR analysis of *Cfp* and *Cfb* transcript levels in circulating and splenic Ly6C^{hi} monocytes. Data are expressed relative to gene expression in SD-fed mice.**(C)** *Cfp* and *Cfb* expression of aortic myeloid cell subsets from a meta-analysis of 9 single cell RNA sequencing studies of atherosclerotic mouse aorta. Average expression level (log2 scale) indicated by saturation of blue (dark blue is highest expression with minimum scaling to 0). **(D)** *Hc* (*C5)* and *C9* expression of aortic leukocyte subsets from a meta-analysis of 9 single cell RNA sequencing studies of atherosclerotic mouse aorta (Zernecke et al., 2020). Average expression level (log2 scale) indicated by saturation of blue (dark blue is highest expression with minimum scaling to 0). (**E-G**) Mixed 1:1 bone marrow transplantation experiment from control (WT, CD45.1) and CFH deficient (CFH KO UBI-GFP, CD45.2) into LDLR-deficient (*Ldlr*$^{-/-}$ CD45.2) mice, following a 12 wks WTD feeding. **(E)** Mean fluorescence intensity (MFI) of surface levels of CD11b, TIM4, VSIG4 and MHCII among splenic monocyte-derived macrophages (Mo-Macs), measured by flow cytometry. **(F)** Percent of chimerism among aortic CD11b^{-}F4/80^{-} and CD11b^{+}F4/80^{-} cells at the end of the study with the representative dot plots, quantified by flow cytometry. **(G)** Enumeration of 7-aminoactinomycin D (7-AAD)-positive aortic macrophages by flow cytometry. **(H)** Heat map of genes associated with "eat me", "find me" and bridging molecules between CFH-deficient vs control macrophages. Each symbol represents individual mice. Statistical significance was evaluated by two-tailed Student's *t*-tests (*$P < 0.05$, **$P < 0.01$, ***$P < 0.001$, **** $P < 0.0001$). Error bars indicate SEM.

Figure S6 (Related to Figure 6). Hematopoietic deletion of complement factor H does not affect weight gain or lipid metabolism but mitigates atherosclerosis and hepatic inflammation (A-H) Lethally irradiated *Ldlr*$^{-/-}$ mice were reconstituted with bone marrow from *Cfh*$^{+/+}$ vs *Cfh*$^{-/-}$ mice and were fed a Western-type diet (WTD) for 12 weeks, starting 5 weeks after transplantation (n=14 vs n=12). **(A)** Schematic representation of the study. **(B)** Final body weight. **(C)** Plasma cholesterol and triglyceride levels measured by an automated enzymatic method. Symbols represent individual mice. **(D)** qRT-PCR analysis of transcript levels of *C3* in sorted aortic macrophages. **(E)** Quantitative analysis of atherosclerosis in the aorta. Data are expressed as percentage of Sudan IV-stained area of the entire aorta. Representative images are shown. (**F**) qRT-PCR analyses of transcript levels of *Tgfb* and *Il10* in sorted aortic macrophages. **(G)** Quantification of infiltrating macrophages in liver sections. Data are expressed as number of positive cells per mm^2. Representative images of Mac-1-stained liver sections are shown. Original magnification, 200X; scale bars, 100 μm. **(H)** qRT-PCR analyses of transcript levels of inflammatory genes (*Cxcl1, Cxcl2* and *TNFα*) in total liver tissue. Data are expressed relative to the expression of individual genes in control *Cfh*$^{+/+}$ bone marrow-chimeric mice. Bars represent the mean±SEM of 14 vs 12 mice. Statistical significance was evaluated by two-tailed Student's *t*-tests (*$P < 0.05$, **$P < 0.01$). Error bars indicate SEM.

Figure S7 (Related to Figure 7). Complement C3- and CFH-producing inflammatory aortic macrophages from human coronary arteries express *VSIG4*, but not *C5* (A-B) Comparative analysis of **(A)** mouse and **(B)** human *"complement system"* and *"complement activation"* biological pathways among various aortic leukocyte subsets from Zernecke et al. 2020 and Depuydt et al. 2020, respectively, using *Enrichr*. **(C)** Expression of *C3* and *C5* in single cells from human aortic myeloid cell subsets. Average expression level (log2 scale) indicated by saturation of red (dark red is highest expression with dark blue being the minimum scaling to 0). Dot size represents relative percentage of cells that expressed the corresponding genes in cluster. **(D)** Gene expression profile of *VSIG4* is shown human aortic myeloid cell populations. **(E)** Volcano plot of genes with a significant differential expression in aortic macrophages from carotid artery plaques of symptomatic versus asymptomatic patients. Red arrow indicates *VSIG4* being significantly downregulated in symptomatic patients.